Supporting Information

Air Stable Photo-Redox Active Elusive Cr(III)-Tri-dithiolene-radical Complexes as a New Class of Pseudo-Supercapacitor with High Capacitance: Enhancement of Energy Storage with Heavier Chalcogenide

Sujit Das,[a]† Mayur Thosare,[b]† Saurav Ghosh,[a] T Kedara Shivasharma,[b] Subuhan Ahamed,[a] Harsha S. Karnamkkott,[a] Björn Schwarz,[c]* Babasaheb R. Sankapal,[b]* Liviu, Ungur,[d] and Kartik Chandra Mondal[a]*

[a] M.Sc. S. Das, M.Sc. S. Ahamed, M.Sc. A. Nath, M.Sc. H. S. Karnamkkott, M.Sc. S. Ghosh and Dr. K. C. Mondal*, Department of Chemistry, Indian Institute of Technology Madras. Chennai, 600036, India. E-mail: csdkartik@iitm.ac.in

[b] M.Sc. Thosare and Prof. Dr. B. R. Sankapal*, Department of Physics, Visvesvaraya National Institute of Technology, Nagpur 440010, Maharashtra, India. Email: brsankapal@phy.vnit.ac.in

[c] Dr. B. Schwarz, Institute for Applied Materials (IAM), KIT, Hermann-von-Helmholtz-Platz 1, 76344 Eggenstein-Leopoldshafen, Germany.

[d] Prof. Dr. L. Ungur, Department of Chemistry, National University of Singapore, Office: MD1-05-03A, Singapore 119077, Singapore

†These authors contributed equally to this manuscript

Content:

1. General Synthesis and characterization:

All the organic solvents (THF, *n*-hexane, *n*-pentane, toluene, diethyl ether, C_6D_6) were soaked with 3 Å molecular sieves to remove water, followed by distillation with Na metal and NaK alloy three times under the flow of high-purity argon gas. All experimental procedures were performed inside a glovebox under an argon atmosphere, with moisture and oxygen levels kept below 10 ppm. The dithiolene radical anions [$(THF)_2$Li(SS-NHC=S)] and [$(THF)_2$Li(SS-NHC=Se)] were prepared by following the previously reported synthetic method.[S1] The X-ray single crystal was carefully mounted using Paratone oil, with an argon gas flow to maintain a stable environment. Data was collected using a Bruker D8 VENTURE system, ensuring high-quality diffraction data was captured for analysis at 100 K. Data was refined using the Apex-4 or Apex-6 package. CV was measured in alloyed distilled THF in a potentiometer (CH instrument). NMR spectra were recorded in C_6D_6 using a 500/400 MHz Bruker instrument at IIT Madras. XPS data were collected at IIT Madras and results were supported with the previous reports.[S2] EPR spectra were simulated using the EASY-SPIN package.[S3] X-band EPR measurements of complexes **1-2** were carried out at rt and 77 K at SAIF, IITM. Supercapacitor measurements were carried out at VNIT, Nagpur, utilizing ground powders of complexes **1-2** coating on stainless steel (as anode). Here, [Cr(III)(SS-NHC=S)$_3$] is named as complex **1** (E = S) and [Cr(III)(SS-NHC=Se)$_3$] as complex **2** (E = Se.

2. Synthesis: The reaction was carried out inside the glove box, and filtration and extraction were performed in the Schlenk line. The single crystals of Cr(III)-triradical complexes (**1-2**) were separated inside the glove box.

Synthesis of complex [Cr(III)(SS-NHC=S)$_3$] (complex **1**) [E = S]**:**

In a 100 mL Schlenk flask, 380 mg (0.6 mmol, 3 equiv.) of lithium salt of anionic dithiolene radical ligand [$(THF)_2$Li(SS-NHC=S)] was added, followed by the addition of 20 mL of freshly distilled NaK alloy THF. The mixture was stirred for 10 minutes until complete dissolution was achieved to obtain a dark purple solution. Subsequently, $CrCl_2$ (25 mg, 0.2 mmol, 1 equiv.) was introduced at rt, resulting in a noticeable colour change from dark purple to royal blue. The reaction mixture was stirred at room temperature for 2.5 h. After completion of the reaction, THF was evaporated, and the resultant residue was extracted with *n*-hexane. Long rods of dark green colored Cr(III)-triradical complex **1**, were grown from a concentrated

solution (volume of ~ 10 mL). The yield is 60% (calculated with respect to $CrCl_2$). We can obtain the same product by adjusting the ratio of the metal salt and the radical ligand. Specifically, using one or two equivalents (s) of the dithiolene radical in combination with one equivalent of anhydrous chromium-dichloride results in a lower yield (30% or 43%) compared to the above-mentioned method.

Complex **1** was also isolated when the dry mass was extracted with toluene, indicating that both solvents were effective in extracting the Cr-complex from the residue. This complex is soluble in *n*-hexane, THF, C_6D_6, and toluene. Pure single crystals were isolated after separation from the mother liquor and followed by a quick wash with cold n-hexane inside the glove box. They were dried under vacuum. These single crystals were ground to obtain the powders and utilised for all the characterisation and supercapacitor studies.

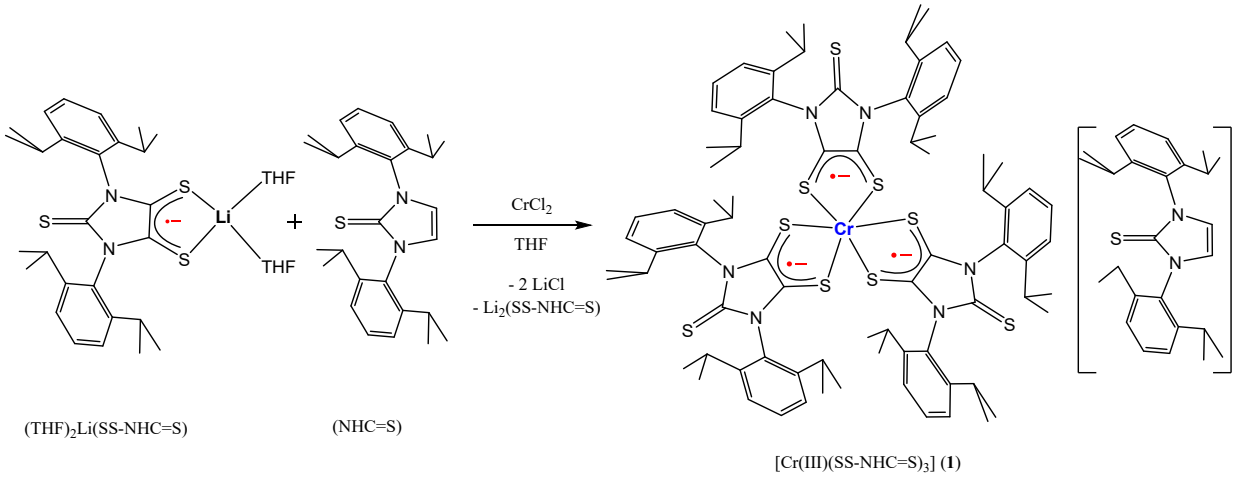

Scheme S1. Synthesis of Cr(III)-triradical complex **1**.

Alternative method: In a Schlenk flask, 253 mg (0.4 mmol, 1 equiv.) of an anionic dithiolene radical ligand was added, followed by 30 mL of dry THF. The mixture was stirred for 10 minutes until the ligand was fully dissolved. Next, anhydrous $CrCl_2$ (100 mg, 0.8 mmol, 2 equiv.) was introduced, causing a visible colour change from dark purple to royal blue. The reaction was allowed to stir at ambient temperature for 3 hours. Upon completion, the THF solvent was removed by evaporation, and the remaining residue was extracted with 30 mL of hexane, yielding the desired product. During the extraction and solvent volume reduction, block-shaped, dark bluish-green crystals formed in significant quantities. The yield is 15% (calculated with respect to $CrCl_2$).

Elemental analysis C, H, N (clcd.) (%) for $C_{108}H_{138}CrN_8S_{10}$: C 67.48 (67.53), H 7.30 (7.24), N 5.78 (5.83).

IR (KBr; cm^{-1}): 2955, 2917, 2867, 1471, 1362, 1304, 1258, 1191, 1095, 1057, 1020, 986, 940, 806, 710, 602, 430. KBr powders have been dehydrated at 250 ^oC under high vacuum before sample preparation. A KBr pellet was prepared inside the glove box at rt.

UV-VIS-NIR bands (THF): 350, 652, 522, and 900 nm.

Thermal stability: The powders of **1** decompose above 150 °C.

Synthesis of complex [Cr(III)(SS-NHC=Se)$_3$] (**2**; [E = Se]**:**

The synthetic method, which led to the isolation of complex **1** [E = S], was not successful for complex **2** [E = Se]. KOH was effective as an additive for the preparation of **2**.

The synthesis begins with the preparation of a striking dark blue solid, the lithium salt of the dithiolene radical anion [(THF)$_2$Li(SS-NHC=Se)], weighing 270 mg (0.4 mmol), which is dissolved in 10 mL dry tetrahydrofuran (THF) to form a vivid blue solution. In a separate flask, chromium(II)chloride ($CrCl_2$, 50 mg, 0.4 mmol) is dissolved in 8 mL THF under an inert atmosphere, and potassium hydroxide (KOH, 45 mg, 0.8 mmol) is added at -40 °C, inducing a light colour change from off-white to light blue. After stirring for 30 minutes, the radical anion solution is introduced, causing the solution to shift from dark blue to dark green, signalling the formation of the desired complex. The mixture is then stirred overnight, with the color deepening to a dark green, indicating completion. Following solvent removal under vacuum, a mixture of THF and *n*-hexane (1 mL + 12 mL, respectively) is used to extract the product, and after allowing the solution to stand undisturbed for several days, dark green crystals of the complex **2** were formed, achieving a yield of 35%. The yield of the reaction does not change on increasing the equivalents of dithiolene radical anion [(THF)$_2$Li(SS-NHC=Se)] ligand to double and triple that of $CrCl_2$. The reason is unknown.

Elemental analysis C, H, N (clcd.) (%) for $C_{81}H_{102}CrN_6S_6Se_3$: C 59.21 (59.29), H 6.32 (6.27), N 5.17 (5.12).

IR (KBr, cm^{-1}): 2967, 2917, 2867, 1630, 1467, 1354, 1312, 1280, 1178, 1090, 1061, 1015, 982, 806, 681, 605, 526 and 434 nm.

UV-Vis-NIR bands (THF): 950, 723, and 364 nm. Pure single crystals were isolated (after removal of mother liquor using a syringe; washed with cold n-hexane), which were ground to form powder required for all other characterisations (EPR, UV, and CV).

***KOH likely functions primarily as a strong base that modulates chromium speciation, precipitating $Cr(OH)_2$ from $CrCl_2$ (1.0 equiv) to effectively lower the concentration of Cr(II) ion: ligand ratio from ~1:1 to 1/3:1, favouring formation of tris-dithiolene-complex. Control experiments confirm its necessity. Analogous conditions, which lead to the formation of complex **1** (1 equiv $CrCl_2$, 3 equiv ligand, in the absence of KOH) did not lead to the formation of single crystals of complex **2** underscoring KOH's role in controlled hydrolysis and/or Cr(II)/Cr(III) redox equilibrium.

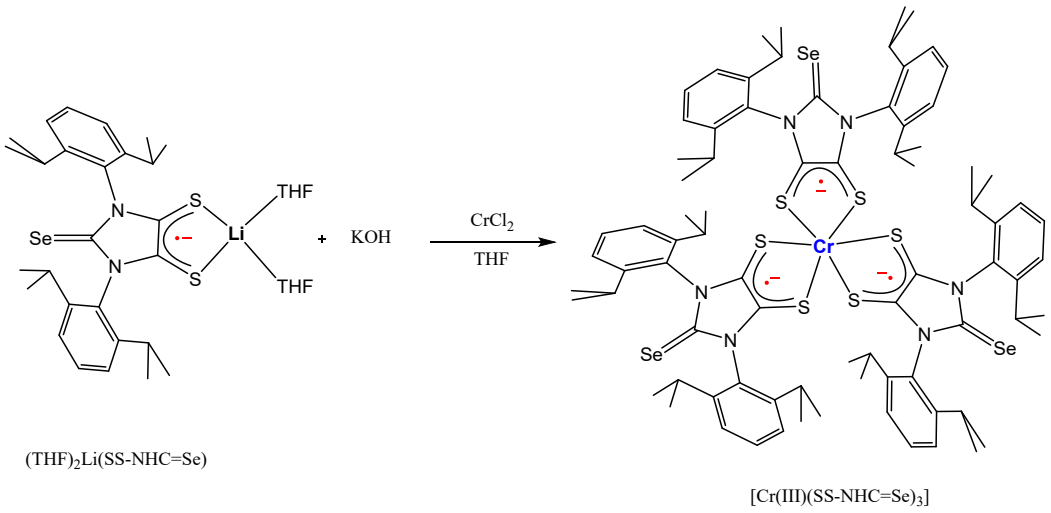

Scheme S2. Synthesis of Cr(III)-triradical complex **2**; E = Se.

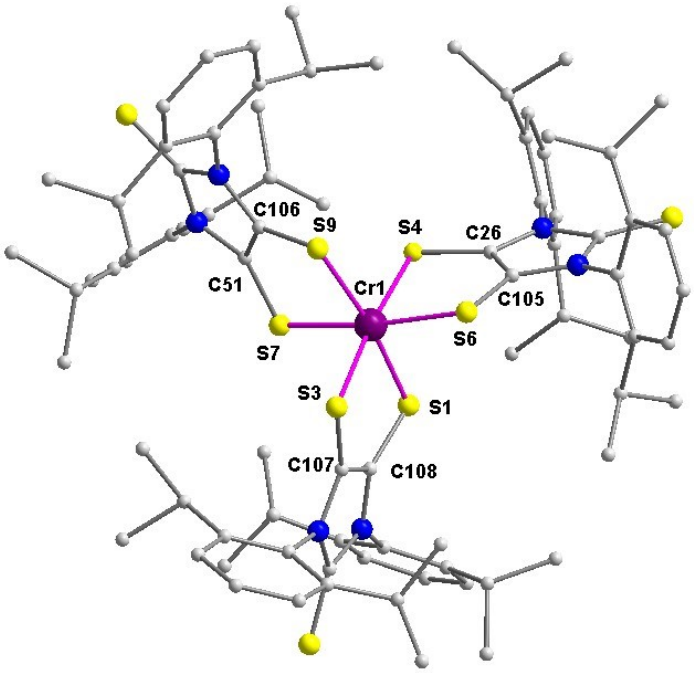

Figure S1. Molecular structure of complex **1** (E = S). The lattice NHC=S, and all the H atoms were omitted for clarity. Red, Se; blue, N; off-white C.

3. UV-VIS-NIR measurements.

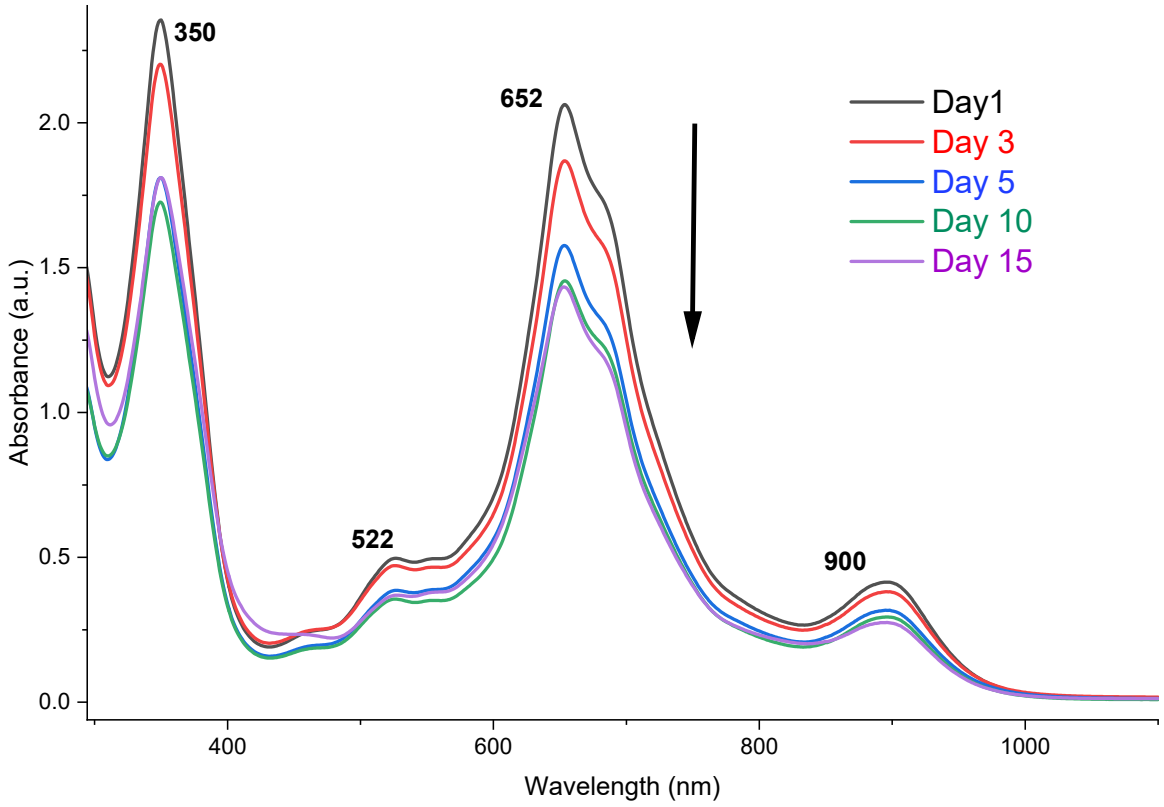

Figure S2. The stacked UV-vis spectra of complex **1** in THF over 15 days. 7 mg of single crystals of complex **1** were stored in open air for one to fifteen days. Then 1.4 mg of sample

was dissolved in 10 mL of dry THF on the 1st, 3rd, 5th, 10th and 15th days to obtain dark blue solutions. The UV-vis spectra were recorded. Day-1 means immediately after exposure to air, the UV-vis spectrum was recorded. This experiment shows that complex **1** takes two weeks for the decomposition of 25%. The intensity of the absorption bands at 652 and 900 nm gradually decreases, and the band at 350 nm slowly increases.

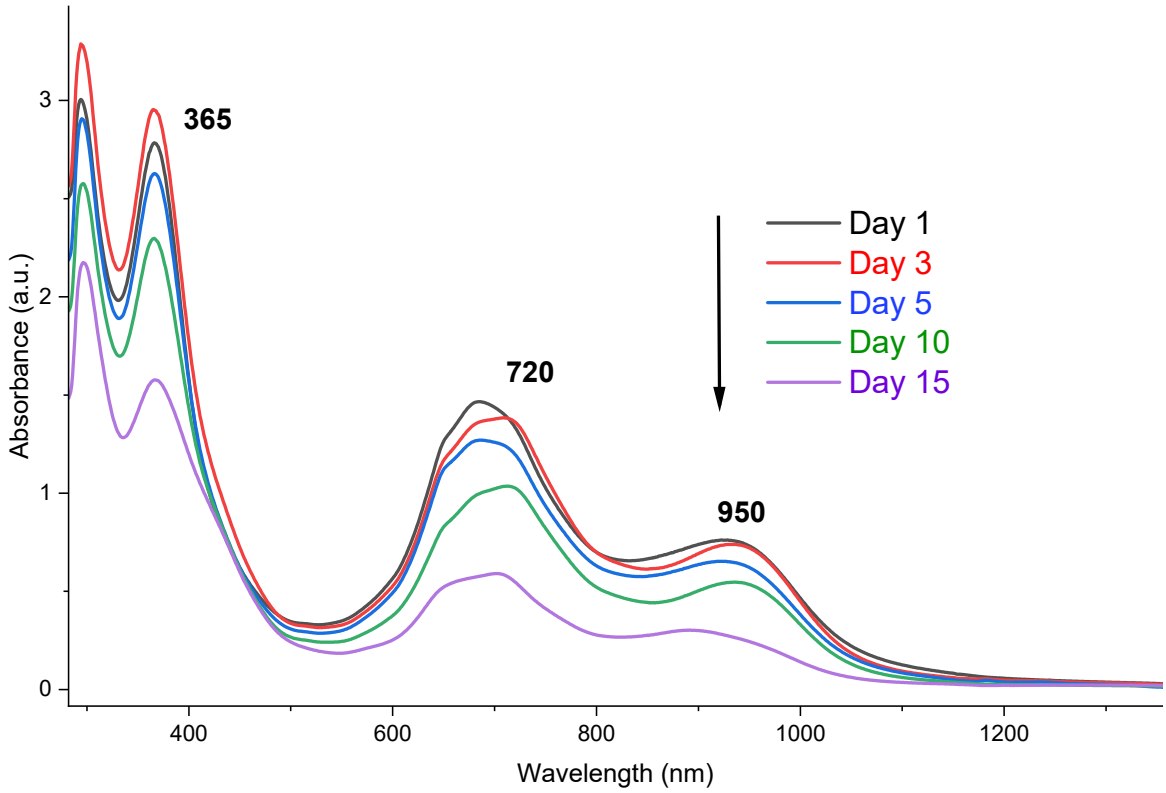

Figure S3. The stacked UV-vis spectra of complex **2** in THF over 15 days. The stacked UV-vis spectra of complex **2** in THF over 15 days. 13.5 mg of single crystals of complex **2** were stored in open air for one to fifteen days. Then 2.7 mg of sample was dissolved in 10 mL of dry THF on the 1st, 3rd, 5th, 10th and 15th day to obtain dark green solutions. The UV-vis spectra were recorded. Day 1 means immediately after exposure to air, the UV-vis spectrum was recorded. This experiment shows that complex **2** takes two weeks for the decomposition of 50%. The intensity of the absorption bands at 720 and 950 nm gradually decreases.

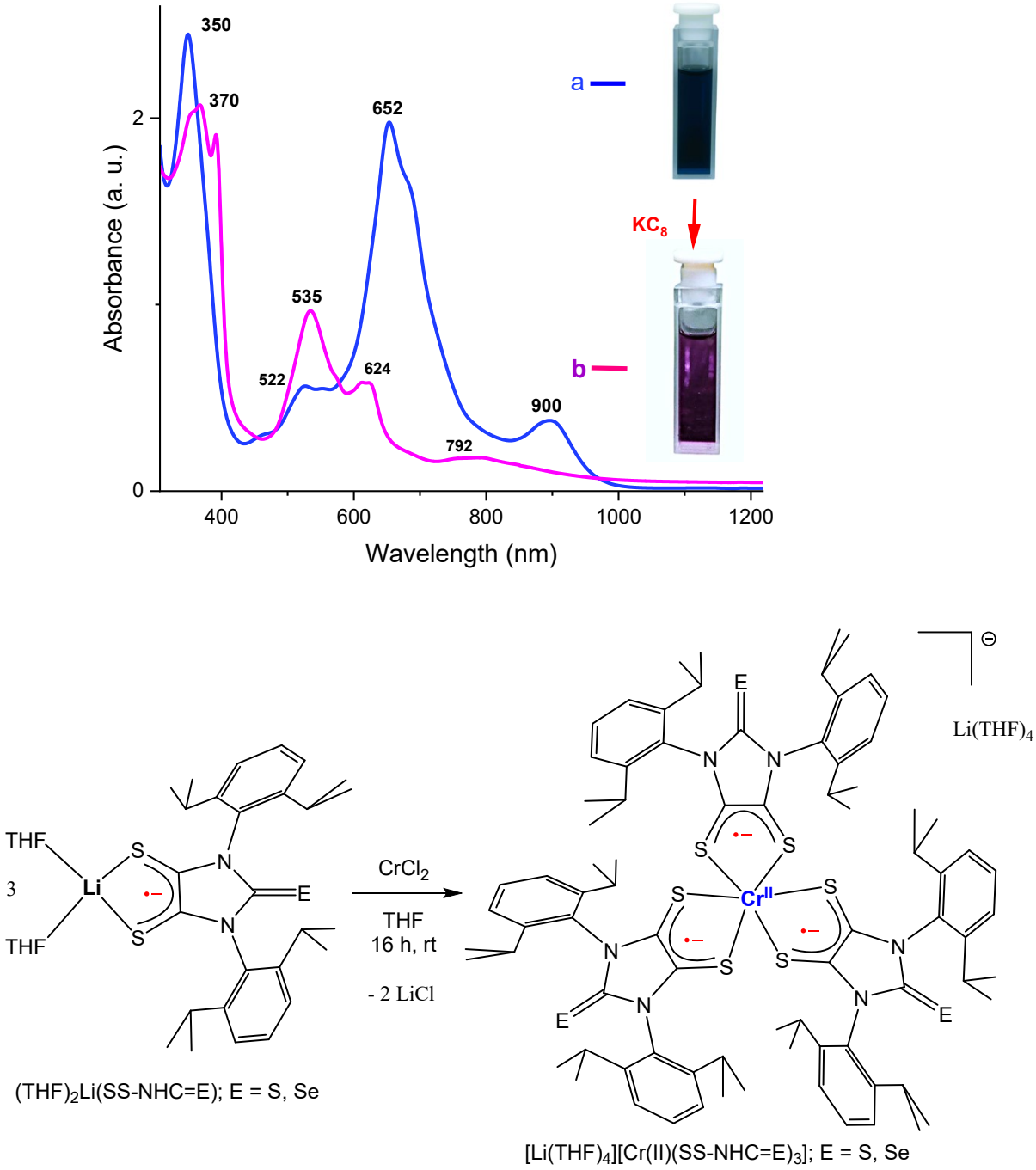

Figure S4. **(**a) UV-Vis spectrum of complex **1** in THF solution [E = S]. (b) UV-Vis spectrum of the one-electron-reduced species generated in situ by reaction with two equiv. KC_8 in THF. 350, 652, 522, and 900 nm.The EPR spectra of both (a) and (b) were recorded and presented in their respective places.

Molar extinction coefficient of complex **1**:

900 nm: 1.06 $\times 10^3$ L mol^{-1} cm^{-1}

652 nm: 5.32 $\times 10^3$ L mol^{-1} cm^{-1}

522 nm: 1.52 $\times 10^3$ L mol^{-1} cm^{-1}

350 nm: 6.62 $\times 10^3$ L mol^{-1} cm^{-1}

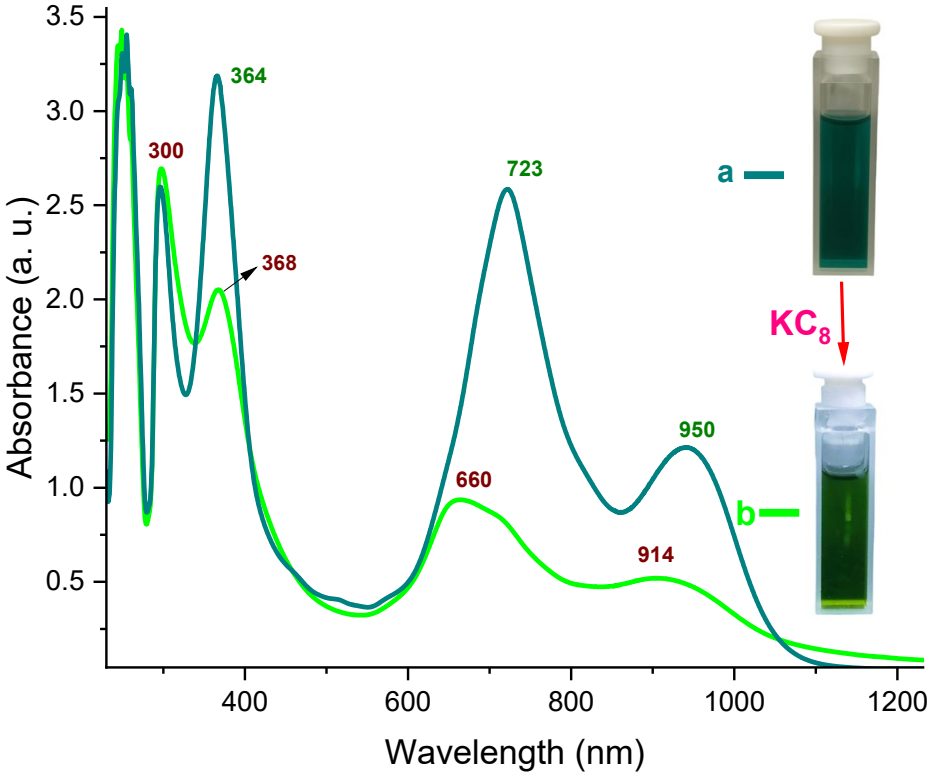

Figure S5. UV-Vis-NIR spectra of complex [Cr(III)(SS-NHC=Se)$_3$] (**2**) before (a) and after (b) addition of two equivalents of KC_8 in THF solution. The colour change was shown in the set. The EPR spectra of both (a) and (b) were recorded and presented in their respective places.

Molar extinction coefficient of [Cr(III)(SS-NHC=Se)$_3$] (**2**) [E = Se]:

950 nm: 1.83 $\times 10^3$ L mol^{-1} cm^{-1}

723 nm: 3.59 $\times 10^3$ L mol^{-1} cm^{-1}

364 nm: 4.37 $\times 10^3$ L mol^{-1} cm^{-1}

4. IR spectra

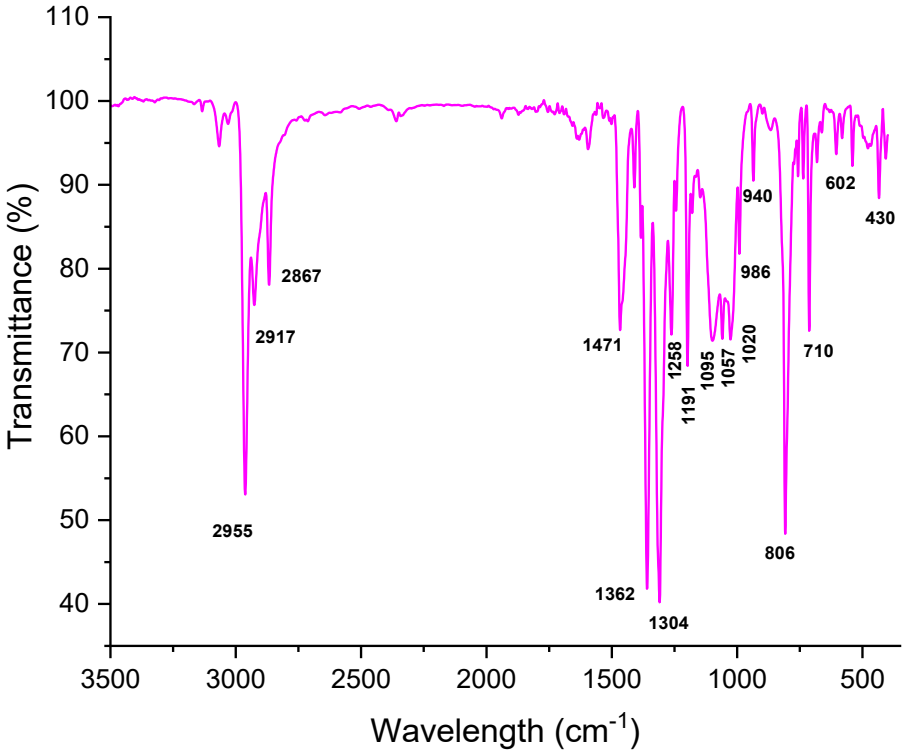

Figure S6. FT-IR spectrum of complex **1** with dry KBr.

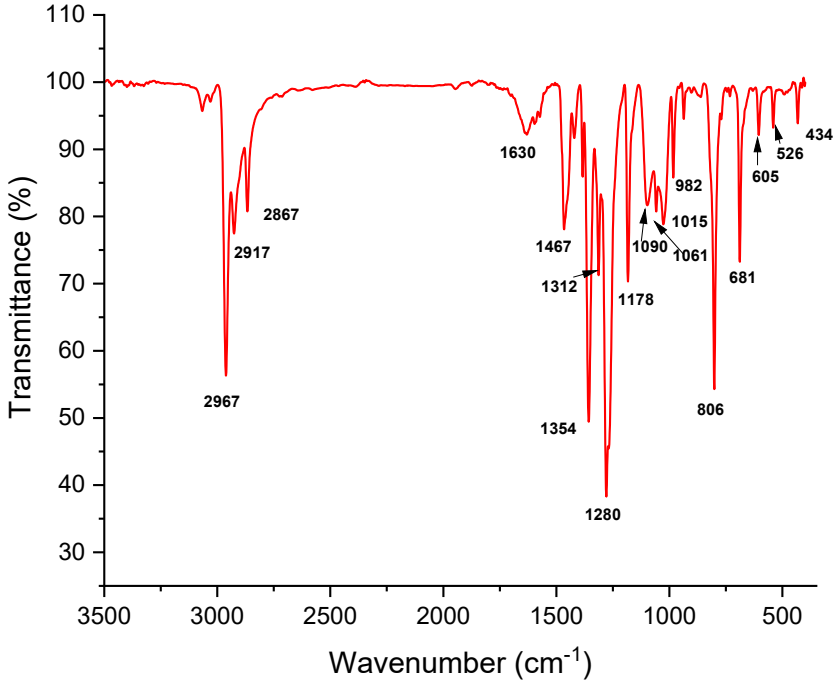

Figure S7. FT-IR spectrum of [Cr(III)(SS-NHC=Se)$_3$] (**2**) with dry KBr.

5. EPR measurements

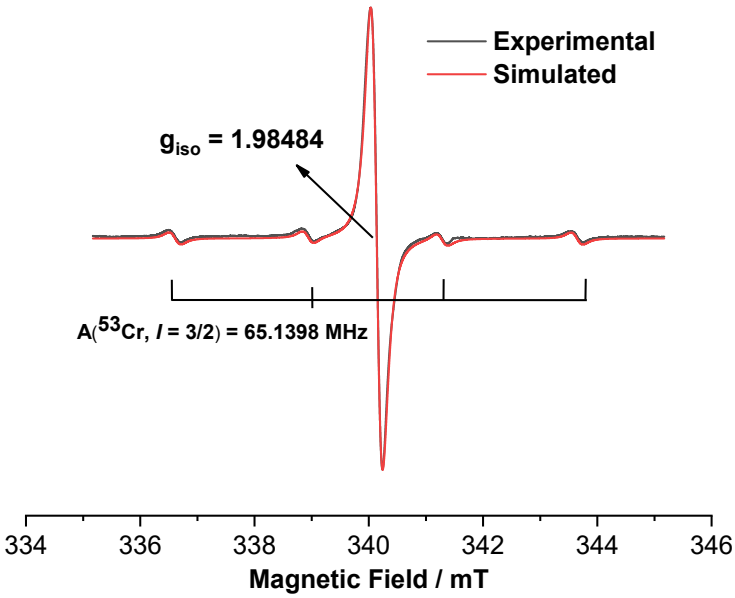

Figure S8. X-band EPR spectrum (black) of the anionic complex [Cr(III)(SS-NHC=S)$_3$] (**1**$^{\bullet-}$) at room temperature in THF solvent. Red and black lines represent the simulated and experimental spectra, respectively, and the simulation is done using the EasySpin program [S3]. [$\mathbf{g_{iso}}$ = 1.98484, LWPP (Gaussian broadening) = 0.105 mT, LWPP (Lorentzian broadening) = 0.155 mT, A(^{53}Cr, natural abundance = 9.5%) = 65.14 MHz, X-band experimental frequency = 9.4492 GHz].

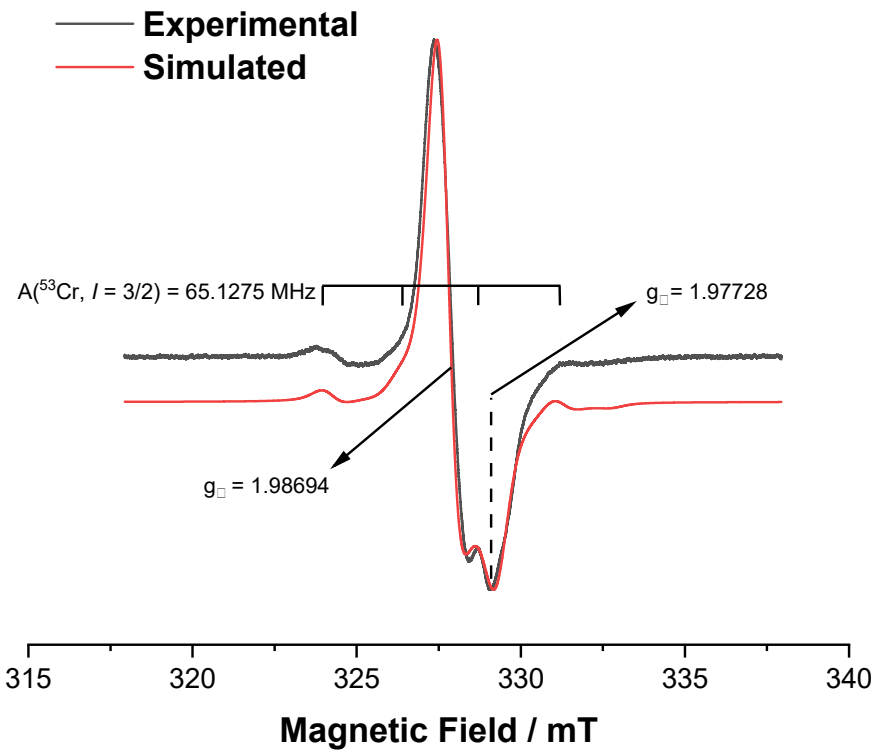

Figure S9. X-band EPR spectrum (black) of anionic complex [Cr(III)(SS-NHC=S)$_3$] (**1**$^{\bullet-}$) at liquid nitrogen temperature in THF. Red and black lines represent the simulated and experimental spectra, respectively, and the simulation is done using the EasySpin program [S3]. [$\mathbf{g_{\parallel}}$ = 1.97728, $\mathbf{g_{\perp}}$ = 1.98694**,** LWPP (Gaussian broadening) = 0.455 mT, LWPP (Lorentzian broadening) = 0.374 mT, A(^{53}Cr) = 65.13 MHz, X-band experimental frequency = 9.1116 GHz].

$$g_{iso} = \sqrt{\frac{2g_{\perp}^{2} + g_{\parallel}^{2}}{3}} = \sqrt{\frac{2 \times 1.98694^{2} + 1.97728^{2}}{3}} = 1.98372$$

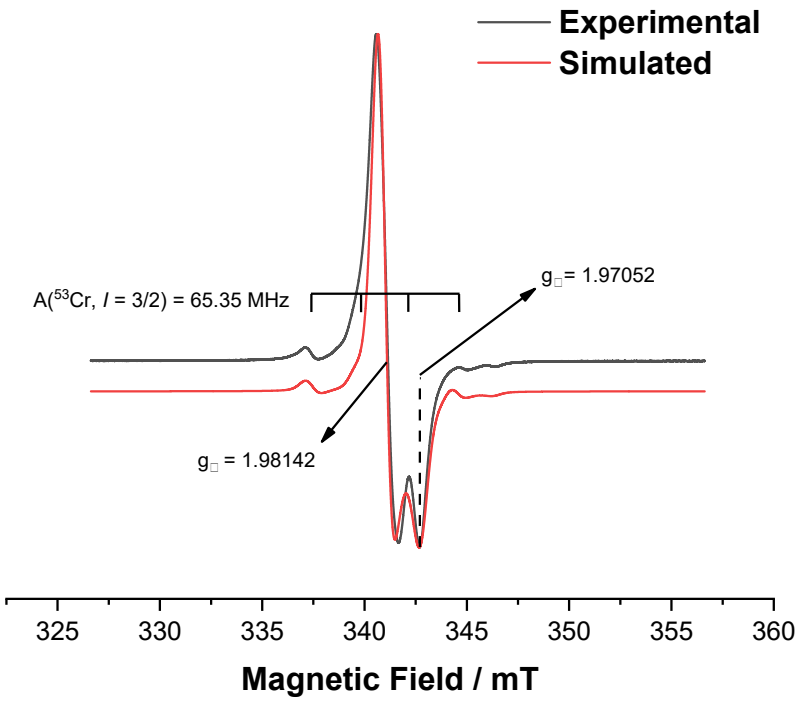

Figure S10: X-band EPR spectrum (black) of anionic complex [Cr(III)(SS-NHC=S)$_3$] (**1**$^{\bullet-}$) at room temperature in solid state. Red and black lines represent the simulated and the experimental spectra, respectively, and the simulation is done using the EasySpin program [S3]. [$\mathbf{g}_{\parallel}$ = 1.97052, $\mathbf{g}_{\perp}$ = 1.98142, LWPP (Gaussian broadening) = 0.549661 mT, LWPP (Lorentzian broadening) = 0.249846 mT, A(^{53}Cr) = 65.355 MHz, X-band experimental frequency = 9.4526 GHz].

$$g_{iso} = \sqrt{\frac{2g_{\perp}^{2} + g_{\parallel}^{2}}{3}} = \sqrt{\frac{2 \times 1.98142^{2} + 1.97052^{2}}{3}} = 1.97779$$

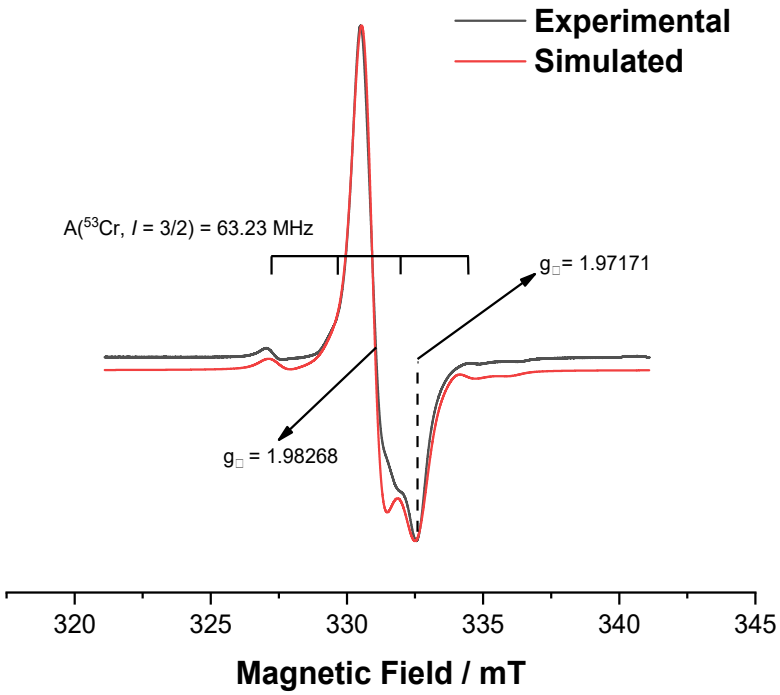

Figure S11. X-band EPR spectrum (black) of the anionic complex [Cr(III)(SS-NHC=S)$_3$] (**1**$^{\bullet-}$) at liquid nitrogen temperature in the solid state. Red and black lines represent the simulated and the experimental spectra, respectively, and the simulation is done using the EasySpin program [S3]. [$\mathbf{g}_{\parallel}$ = 1.97171, $\mathbf{g}_{\perp}$ = 1.98268, LWPP (Gaussian broadening) = 0.536716 mT, LWPP (Lorentzian broadening) = 0.364 mT, A(^{53}Cr) = 63.24 MHz, X-band experimental frequency = 9.1783 GHz].

$$g_{iso} = \sqrt{\frac{2g_{\perp}^{2} + g_{\parallel}^{2}}{3}} = \sqrt{\frac{2 \times 1.98268^{2} + 1.97171^{2}}{3}} = 1.97903$$

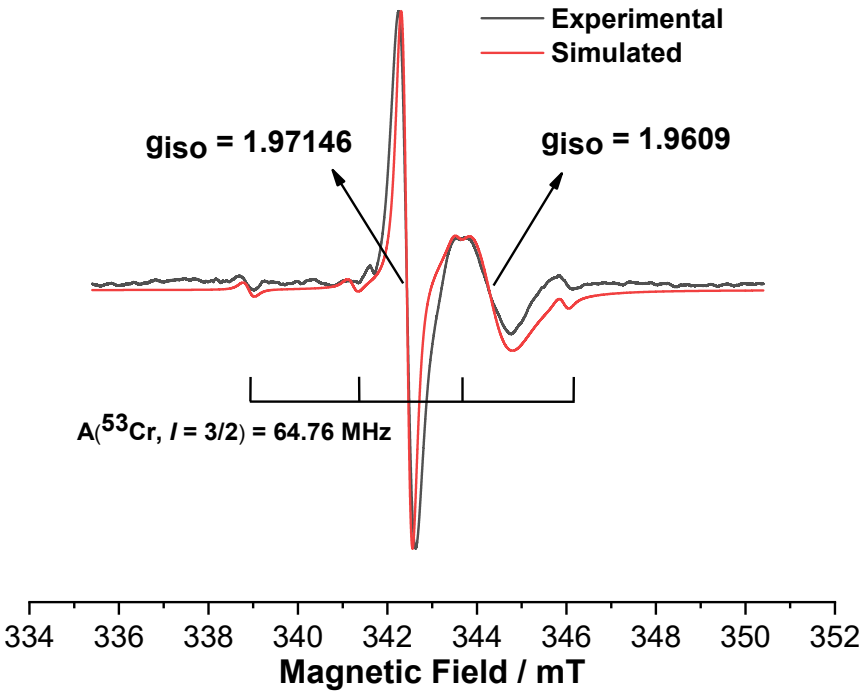

Figure S12. X-band EPR spectrum (black) of anionic complex [Cr(III)(SS-NHC=Se)$_3$] (**2**$^{\bullet-}$) at room temperature in THF. Red and black lines represent the simulated and the experimental spectra, respectively, and the simulation is done using the EasySpin program [S3]. [Two signals – #1: **More intense signal** → $\mathbf{g_{iso}}$ = 1.97146, LWPP (Gaussian broadening) = 0.156541 mT, LWPP (Lorentzian broadening) = 0.159626 mT, **A(^{53}Cr)** = 64.7597 MHz; #2: low intense signal → $\mathbf{g_{iso}}$ = 1.9609, LWPP (Gaussian broadening) = 0.49 mT, LWPP (Lorentzian broadening) = 0.80 mT, X-band experimental frequency = 9.4487 GHz].

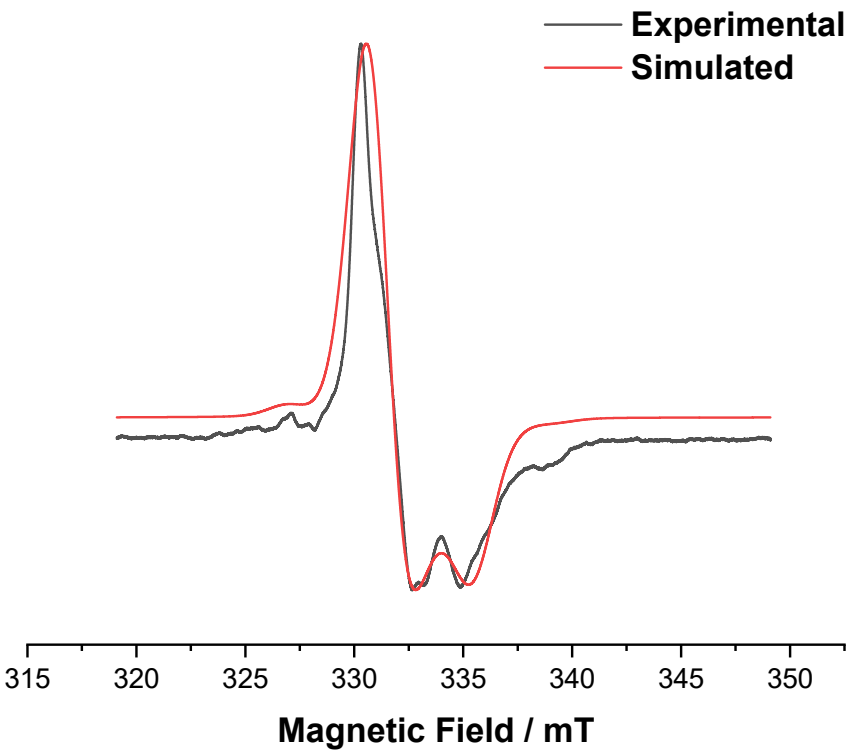

Figure S13. X-band EPR spectrum (black) of the anionic complex [Cr(III)(SS-NHC=Se)$_3$] (**2**$^{\bullet-}$) at liquid nitrogen temperature in THF solvent. Red and black lines represent the simulated and experimental spectra of the complex **2**$^{\bullet-}$ using the EasySpin program. [$\mathbf{g}_{\perp}$ = 1.97942, $\mathbf{g}_{\parallel}$ = 1.95396, LWPP (Gaussian broadening) = 1.59694 mT, LWPP (Lorentzian broadening) = 0.184668 mT, A(^{53}Cr) = 68.99 MHz, X-band experimental frequency = 9.1726 GHz].

$$g_{iso} = \sqrt{\frac{2g_{\perp}^{2} + g_{\parallel}^{2}}{3}} = \sqrt{\frac{2 \times 1.97942^{2} + 1.95396^{2}}{3}} = 1.97097$$

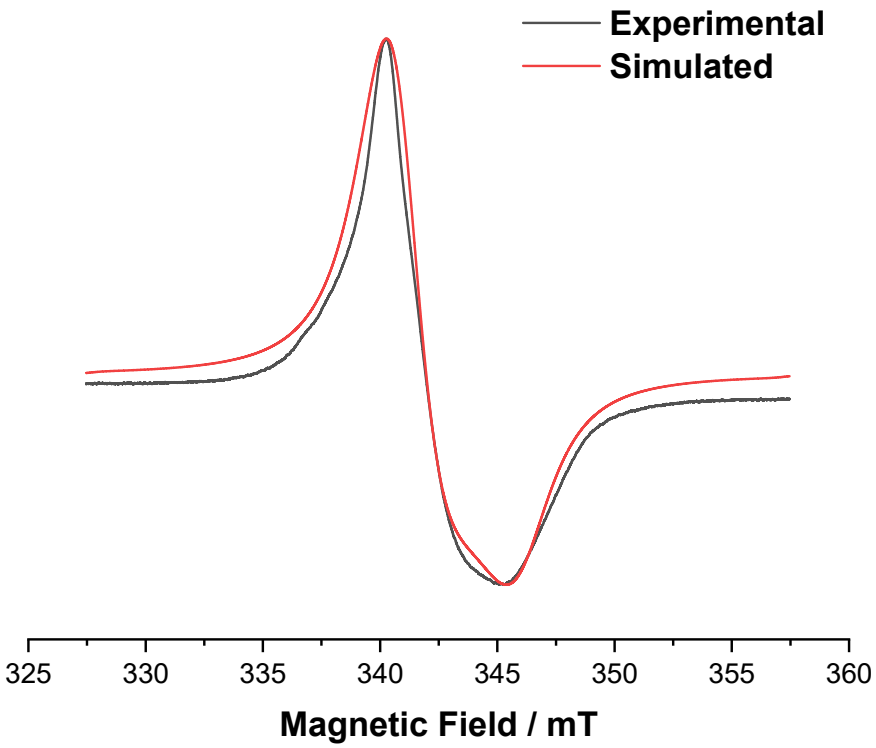

Figure S14. X-band EPR spectrum (black) of anionic complex [Cr(III)(SS-NHC=Se)$_3$] (**2**$^{\bullet-}$) at room temperature in the solid state. Red and black lines represent the simulated and experimental spectra of complex **2**$^{\bullet-}$ using the EasySpin program.[S3] [$g_\perp$ (Radical unpaired e$^-$) = 1.98079, $g_\parallel$ (Radical unpaired e$^-$) = 1.95324, LWPP (Gaussian broadening) = 1.0 mT, LWPP (Lorentzian broadening) = 1.97 mT, X-band experimental frequency = 9.4527 GHz].

$$g_{iso} = \sqrt{\frac{2 \times {g_\perp}^2 + {g_\parallel}^2}{3}} = \sqrt{\frac{2 \times 1.98079^2 + 1.95324^2}{3}} = 1.97165$$

Reactions with KC_8 (Figures 8 and 9):

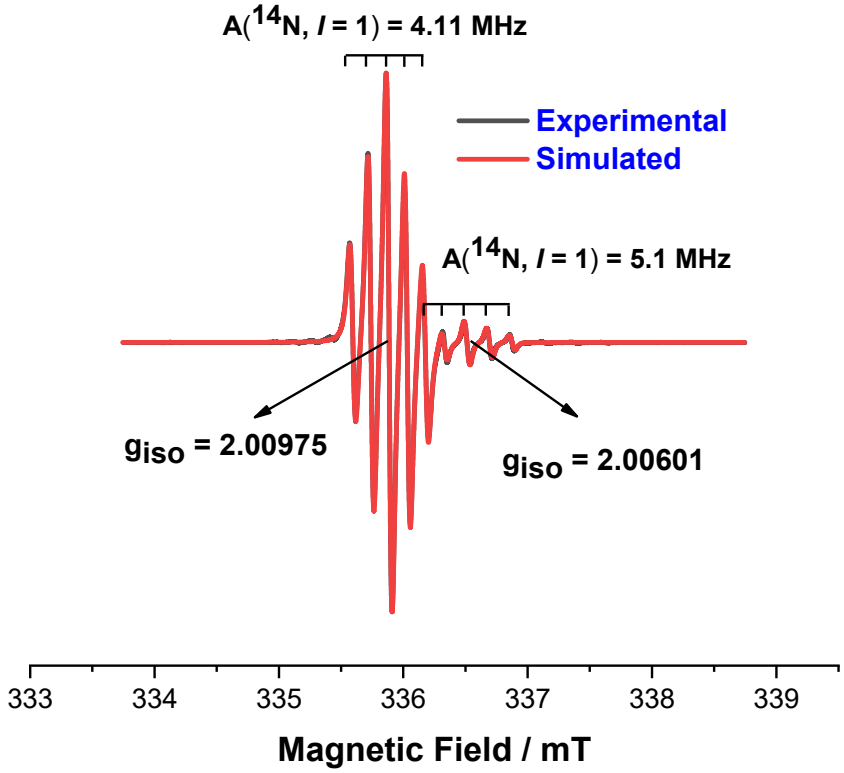

Figure S15. X-band EPR spectrum (black) of complex **1** after the reaction with two equivalents of KC_8 at room temperature in THF (**1** + 2 e^- → $\mathbf{1}^{2-}$). Red and black lines represent the simulated and experimental spectra, respectively, and the simulation is done using the EasySpin program.[S3] [Two signals – **#1: More intense signal** → $\mathbf{g_{iso}}$ = 2.00975, LWPP (Gaussian broadening) = 0.026 mT, LWPP (Lorentzian broadening) = 0.034 mT, **A(^{14}N)** = 4.11 MHz; **#2: Less intense signal** → $\mathbf{g_{iso}}$ = 2.00601, LWPP (Gaussian broadening) = 0.04 mT, LWPP (Lorentzian broadening) = 0.016 mT, **A(^{14}N)** = 5.1 MHz, X-band experimental frequency = 9.4481 GHz].

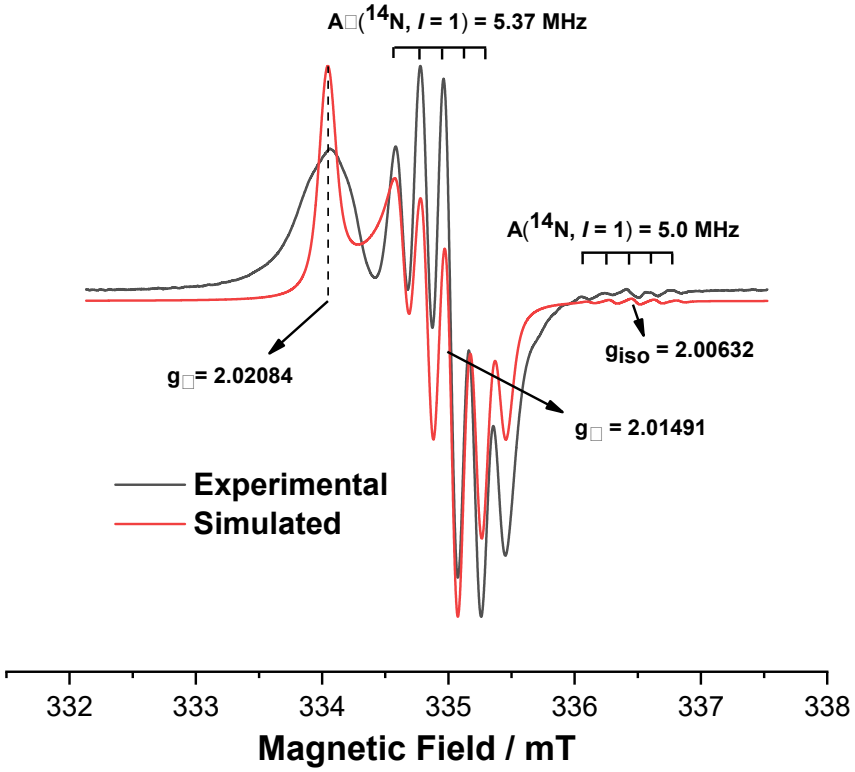

Figure S16. X-band EPR spectrum (black) of complex **2** after the reaction with two equivalents of KC_8 at room temperature in THF (**2** + 2 e^- → $\mathbf{2}^{2-}$). Red and black lines represent the simulated and the experimental spectra respectively, and the simulation is done using the EasySpin program.[S3] [Two signals – **#1: More intense signal** → $\mathbf{g_{\parallel}}$ = 2.02084, $\mathbf{g_{\perp}}$ = 2.01491, LWPP (Gaussian broadening) = 0.074055 mT, LWPP (Lorentzian broadening) = 0.059 mT, $\mathbf{A_{\perp}(^{14}N)}$ = 5.4 MHz; **#2: Less intense signal** → $\mathbf{g_{iso}}$ = 2.00632, LWPP (Gaussian broadening) = 0.042 mT, LWPP (Lorentzian broadening) = 0.047 mT, $\mathbf{A(^{14}N)}$ = 5.0 MHz; X-band experimental frequency = 9.4488 GHz].

$$g_{iso} = \sqrt{\frac{2{g_{\perp}}^2 + {g_{\parallel}}^2}{3}} = \sqrt{\frac{2 \times 2.01491^2 + 2.02084^2}{3}} = 2.01688$$

6. CV measurements

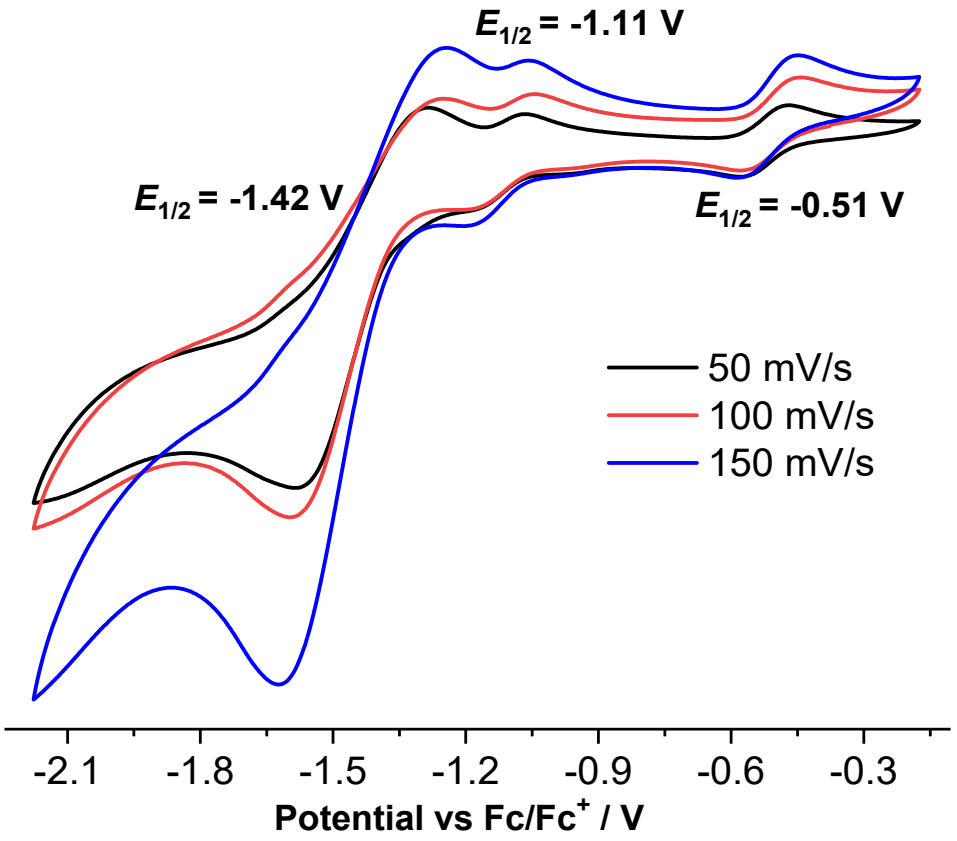

Figure S17. Cyclic voltammogram of complex [Cr(SS-NHC=S)$_3$] (**1**) in THF solution of 0.1 M [n-Bu$_4$N]PF$_6$ with RE: Ag, WE: GC, and CE: Pt.

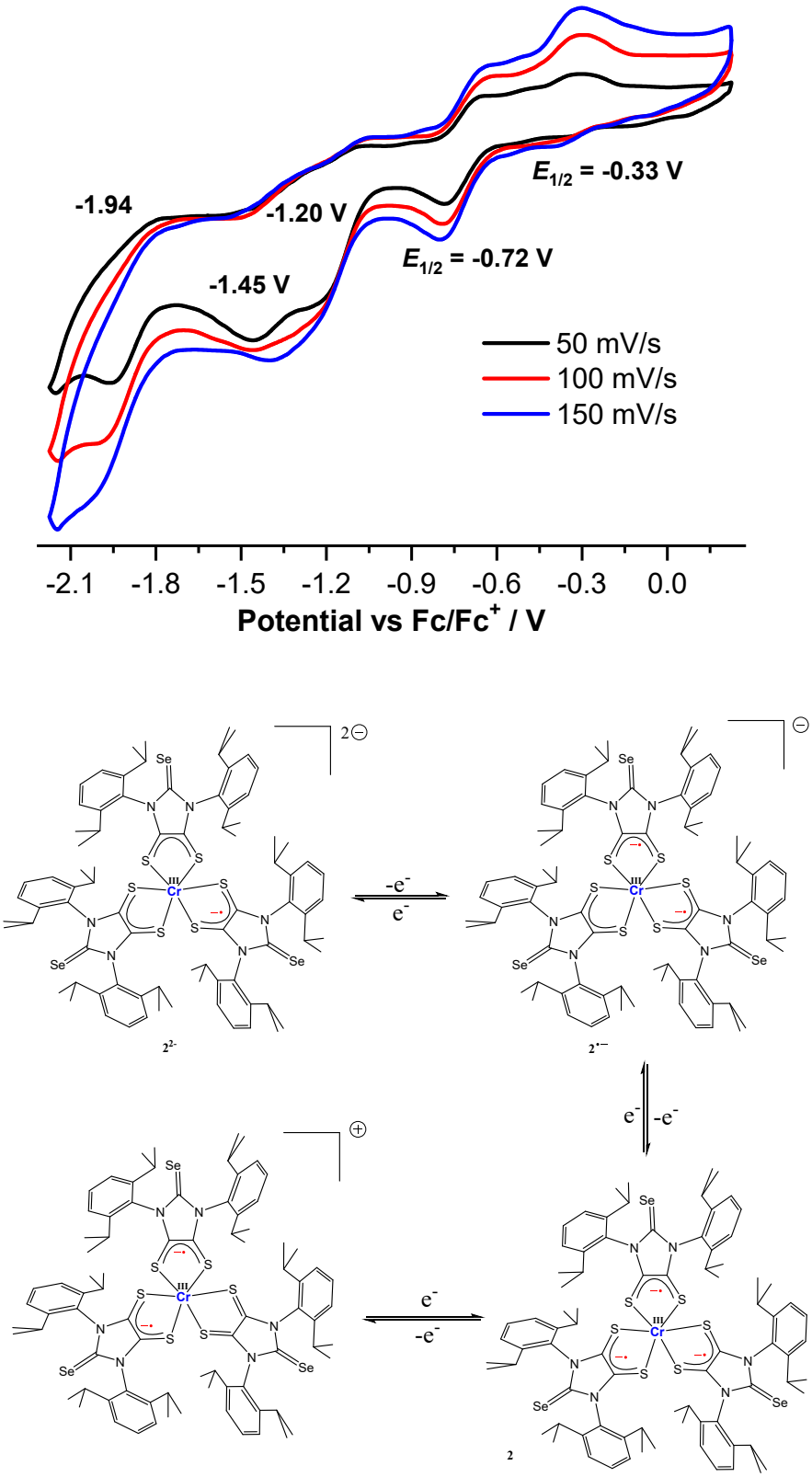

Figure S18. Cyclic voltammogram of complex [Cr(III)(SS-NHC=Se)$_3$] (**2**) in THF solution of 0.1 M [n-Bu$_4$N]PF$_6$ with RE: Ag, WE: GC, and CE: Pt.

7. Magnetic properties calculations

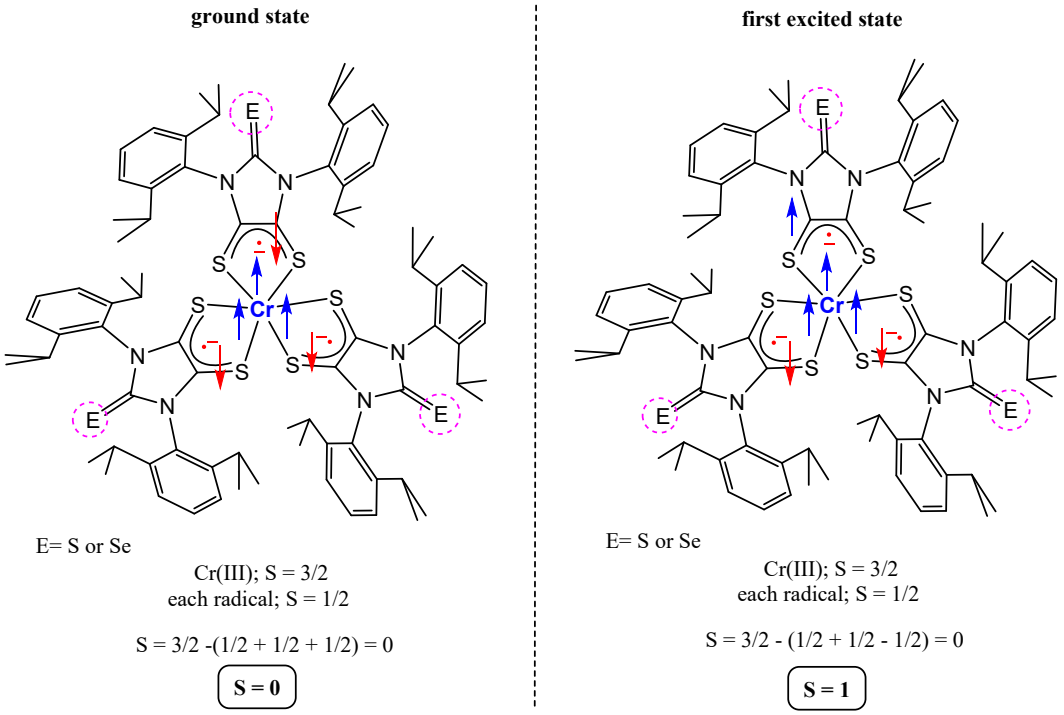

Figure S19. Spin structure of complexes **1** and **2**.

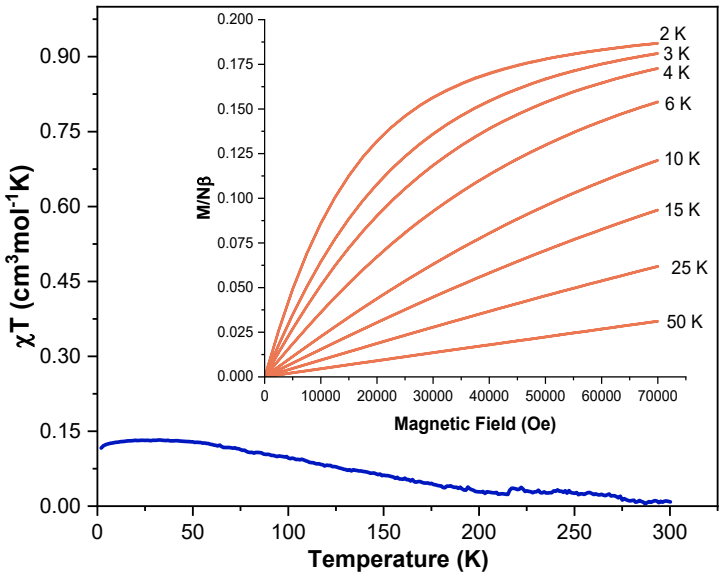

Figure S20. Plots of χT vs T (blue colored lines) and M vs H (red colored lines, in set) for the complex **1**. The diamagnetic corrections were performed.

8. Raman Spectra

Measurements were carried out on a single crust at room temperature at IIT Madras.

9. Single-crystal X-ray diffraction

Crystallographic details of complex **1**.

Single-crystal X-ray diffraction analysis was conducted on complex **1** which crystallises in the orthorhombic system with space group $P2_12_12_1$. The unit cell parameters are $a = 17.5855(9)$ Å, $b = 17.6236(9)$ Å, and $c = 35.3864(19)$ Å, with a unit cell volume of 10,966.9(10) Å^3. The crystal structure was determined at 173 K using Cu Kα radiation ($\lambda = 1.54178$ Å). The crystal's calculated density is 1.163 Mg/m^3, and the absorption coefficient is 2.998 mm^{-1}.

The molecular formula of the complex, $C_{108}H_{138}CrN_8S_{10}$, corresponds to the empirical formula weight of 1920.86 g mol^{-1}. The asymmetric unit consists of one complex molecule. Refinement was performed on F^2 using full-matrix least squares, converging with final R indices of $R_1 = 0.0385$ and $wR_2 = 0.1082$ for observed data ($I > 2\sigma(I)$), indicating a high-quality model.

The chromium centre is coordinated by six sulfur atoms from dithiolene-type ligands, forming a distorted octahedral geometry. The Cr–S bond lengths range from 2.3733(11) to 2.4030(11) Å, consistent with typical Cr(III)–thiolate interactions. The shortest bond lengths are observed for Cr(1)–S(4) and Cr(1)–S(7) at 2.3733(11) Å and 2.3738(10) Å, respectively, while the longest Cr(1)–S(9) bond length is 2.4030(11) Å. Selected S–Cr–S bond angles further illustrate the distortion from ideal octahedral geometry, with values such as 173.31(4)° for S(4)–Cr(1)–S(3), indicating near trans coordination, and smaller angles like 83.68(4)° for S(4)–Cr(1)–S(7), demonstrating deviations from ideal 90°. The observed bond angles confirm structural asymmetry influenced by ligand constraints.

The sulfur atoms are linked to carbon atoms within the ligands, with S–C bond distances ranging from 1.641(4) Å to 1.697(4) Å. Key C–C bond lengths within ligands show typical aromatic character, e.g., C(104)–C(105) at 1.394(6) Å. Overall, the structural data confirm that complex **1** exhibits a well-defined, stable chromium dithiolene framework with subtle distortions reflecting ligand geometry, consistent with its expected coordination environment.

Table S1. Crystallographic details of complex **1**.

CCDC Deposit	**2408554**
Empirical formula	$C_{108}H_{138}CrN_8S_{10}$
Formula weight	1920.86
Temperature (K)	173 (2)
Wavelength (Å)	1.54178
Crystal system	Orthorhombic
Space group	$P2_12_12_1$
Unit cell dimensions	a = 17.5855 (9) Å b = 17.6236 (9) Å c = 35.386 (2) Å α = 90° β = 90° γ = 90°
Volume ($Å^3$)	10966.9 (10)
Z	4
Density (Mg/m^3)	1.163
Absorption coefficient (mm^{-1})	2.998
F (000)	4104
Crystal size (mm^3)	0.568 x 0.162 x 0.119
Theta range for data collection (°)	2.801 to 70.651
Index ranges	-21<=h<=21, -21<=k<=20, -43<=l<=43
R (int)	0.0854
Reflections collected	122131
Independent reflections	20834
Completeness to theta = 67.679°	100.0 %
Max. and min. transmission	
Number of Restraints	84
Number of Parameters	1258
Refinement method	Full-matrix least-squares on F^2
Final R indices [I>2sigma(I)]	R_1 = 0.0385, wR_2 = 0.1082
R indices (all data)	R_1 = 0.0517, wR_2 = 0.1229
GooF	0.853
Largest diff. peak and hole [$e \cdot Å^{-3}$]	0.287 and -0.368

Table S2. Selected bond lengths [Å] for the complex **1**.

Cr(1)-S(4)	2.3733(11)
Cr(1)-S(7)	2.3738(10)
Cr(1)-S(3)	2.3758(11)
Cr(1)-S(1)	2.3760(11)
Cr(1)-S(6)	2.3950(10)
Cr(1)-S(9)	2.4030(11)
S(1)-C(104)	1.697(4)
S(2)-C(1)	1.641(4)
S(3)-C(105)	1.675(4)
S(4)-C(26)	1.682(4)

S(5)-C(27)	1.643(4)
S(6)-C(106)	1.685(4)
S(7)-C(51)	1.678(4)
S(8)-C(52)	1.642(4)
S(9)-C(107)	1.682(4)
S(10)-C(81)	1.659(4)
C(26)-C(106)	1.400(5)
C(51)-C(107)	1.401(6)
C(104)-C(105)	1.394(6)

Table S3. Selected bond angles [°] for the complex **1**.

S(4)-Cr(1)-S(7)	83.68(4)
S(4)-Cr(1)-S(3)	173.31(4)
S(7)-Cr(1)-S(3)	97.94(4)
S(4)-Cr(1)-S(1)	84.28(4)
S(7)-Cr(1)-S(1)	83.24(4)
S(3)-Cr(1)-S(1)	89.45(4)
S(4)-Cr(1)-S(6)	89.21(3)
S(7)-Cr(1)-S(6)	172.51(4)
S(3)-Cr(1)-S(6)	89.39(4)
S(1)-Cr(1)-S(6)	98.44(4)
S(4)-Cr(1)-S(9)	98.47(4)
S(7)-Cr(1)-S(9)	89.41(4)
S(3)-Cr(1)-S(9)	88.05(4)
S(1)-Cr(1)-S(9)	171.84(4)
S(6)-Cr(1)-S(9)	89.31(4)

Table S4. Crystallographic details of Complex [Cr(SS-NHC=Se)$_3$] (**2**).

CCDC Deposit	**2412264**	**2495748**
Empirical formula	$C_{81}H_{102}CrN_6S_6Se_3$ (**2**)	$C_{125}H_{141}CrN_6P_2S_6Se_3$ (**2**$^-$ $(Ph_3P)_2CH^+$)
Formula weight	1640.92	2270.61
Temperature (K)	100 (2)	106(2)
Wavelength (Å)	0.71073	0.71073
Crystal system	Monoclinic	Triclinic
Space group	*C*2/c	*P*-1
Unit cell dimensions	*a* = 16.5297 (5) Å *b* = 26.3317 (9) Å *c* = 44.3217 (14) Å *α* = 90° *β* = 98.3320 (10)° *γ* = 90°	*a* = 15.4937 (14) Å *b* = 19.5413 (17) Å *c* = 21.8622 (18) Å *α* = 80.071 (3)° *β* = 84.739 (3)° *γ* = 76.758 (3)°
Volume (Å^3)	19087.6 (11)	6337.2(10)
Z	8	2
Density (Mg/m^3)	1.142	1.19
Absorption coefficient (mm^{-1})	1.434	1.12
F (000)	6816	2370
Crystal size (mm^3)	0.135 x 0.110 x 0.092	0.319 x 0.233 x 0.231
Theta range for data collection (°)	1.894 to 26.396	2.2198 to 24.9011
Index ranges	-20<=h<=20, -32<=k<=32, -55<=l<=54	-20<=h<=20, -25<=k<=25, -28<=l<=27
R (int)	0.0569	0.084
Reflections collected	251638	244988
Independent reflections	19552	30794
Completeness to theta = 25.242°	99.9 %	99.9 %
Max. and min. transmission	0.7454 and 0.7092	0.7457 and 0.6271
Number of Restraints	120	0
Number of Parameters	983	1313
Refinement method	Full-matrix least-squares on F^2.	Full-matrix least-squares on F^2.
Final *R* indices [*I*>2sigma(*I*)]	R_1 = 0.0407, wR_2 = 0.1115	R_1 = 0.0587, wR_2 = 0.1751
R indices (all data)	R_1 = 0.0586, wR_2 = 0.1216	R_1 = 0.0854, wR_2 = 0.1887
GooF	0.998	1.231
Largest diff. peak and hole [e·Å^{-3}]	0.532 and -0.324	1.796 and -0.946

Table S5. Selected bond lengths [Å] for the complex [Cr(SS-NHC=Se)$_3$] (**2**).

complex	**2**	(**2**-$(Ph_3P)_2CH^+$)
Cr(1)-S(3)	2.3644(7)	2.3769(9)
Cr(1)-S(2)	2.3704(7)	2.3640(9)
Cr(1)-S(6)	2.3735(7)	2.3932(9)
Cr(1)-S(5)	2.3803(7)	2.3770(9)
Cr(1)-S(4)	2.3914(7)	2.3615(9)
Cr(1)-S(1)	2.3950(7)	2.3779(9)
Se(2)-C(28)	1.802(2)	1.817(3)
Se(3)-C(37)	1.798(3)	1.828(3)
Se(1)-C(1)	1.801(2)	1.823(3)
S(3)-C(29)	1.683(2)	1.690(3)
S(5)-C(38)	1.692(3)	1.699(3)
S(4)-C(30)	1.688(2)	1.688(3)
S(2)-C(3)	1.688(2)	1.718(3)
S(1)-C(2)	1.686(2)	1.727(3)
S(6)-C(39)	1.683(2)	1.698(3)
C(2)-C(3)	1.393(3)	1.391(4)
C(38)-C(39)	1.386(3)	1.386(4)
C(30)-C(29)	1.391(3)	1.360(4)

Table S6. Selected bond angles [°] for the complex [Cr(SS-NHC=Se)$_3$] (**2**).

S(3)-Cr(1)-S(2)	83.61(2)	S(6)-Cr(1)-S(4)	86.77(2)
S(3)-Cr(1)-S(6)	172.64(3)	S(5)-Cr(1)-S(4)	100.20(3)
S(2)-Cr(1)-S(6)	100.70(3)	S(3)-Cr(1)-S(1)	99.43(3)
S(3)-Cr(1)-S(5)	85.02(3)	S(2)-Cr(1)-S(1)	89.29(2)
S(2)-Cr(1)-S(5)	84.44(2)	S(6)-Cr(1)-S(1)	86.65(2)
S(6)-Cr(1)-S(5)	89.44(2)	S(5)-Cr(1)-S(1)	171.88(3)
S(3)-Cr(1)-S(4)	89.45(2)	S(4)-Cr(1)-S(1)	86.70(2)
S(2)-Cr(1)-S(4)	171.31(3)		

10. NMR Spectroscopy

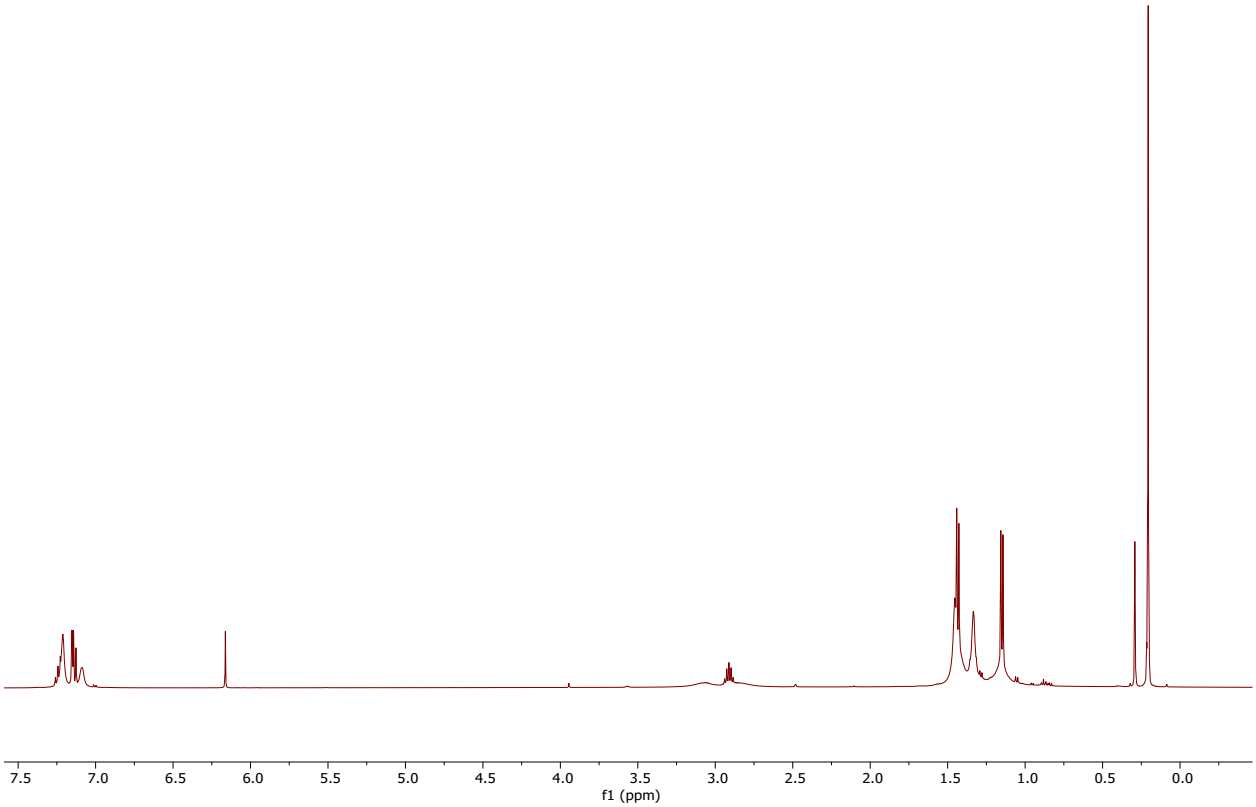

Figure S21. ^{1}H NMR spectrum of complex **1**·NHC=S in C_6D_6 at room temperature (500 MHz). The shaper signals are due to NHC=S of **1**·NHC=S (imidazole ring proton near 6.35 ppm).

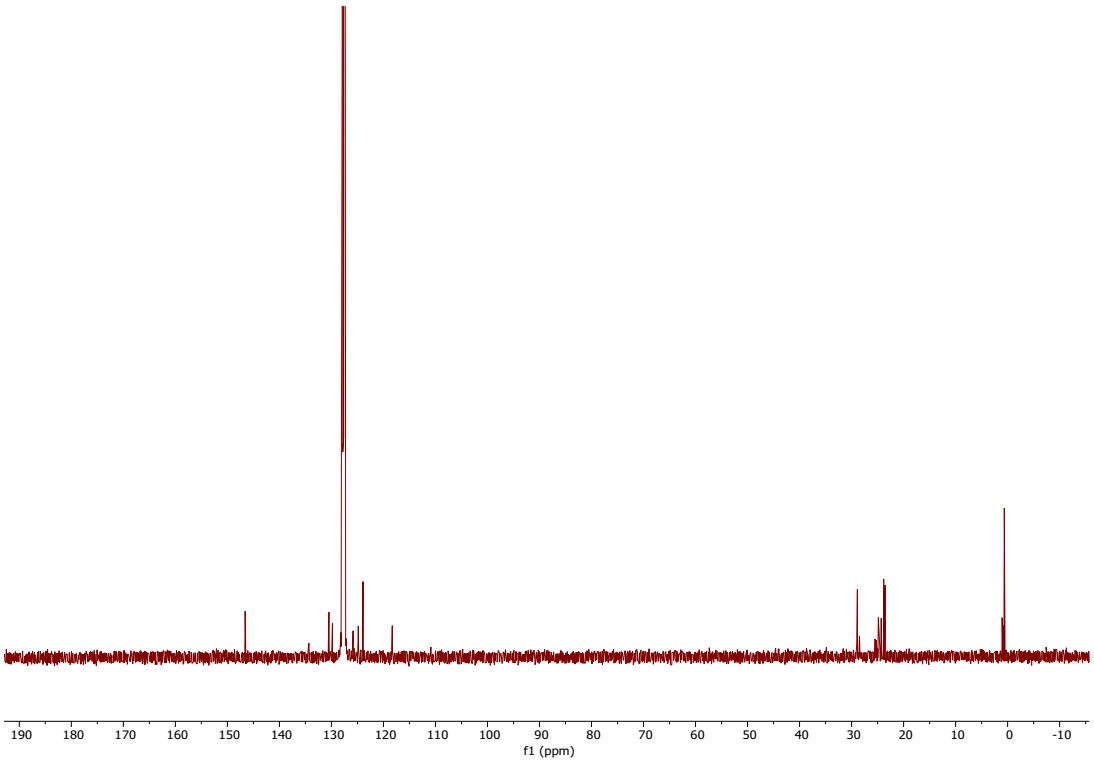

Figure S22. ^{13}C NMR spectrum of complex **1**·NHC=S in C_6D_6 at room temperature (500 MHz).

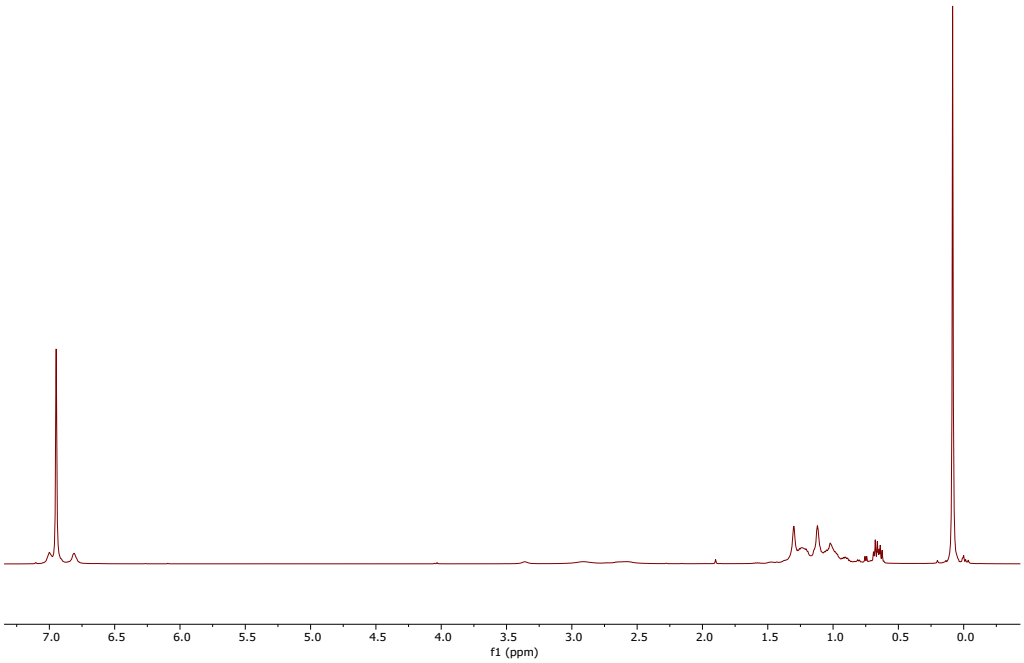

Figure S23. ^{1}H NMR spectrum of complex [Cr(SS-NHC=Se)$_3$] (**2**) in C_6D_6 at room temperature (500 MHz).

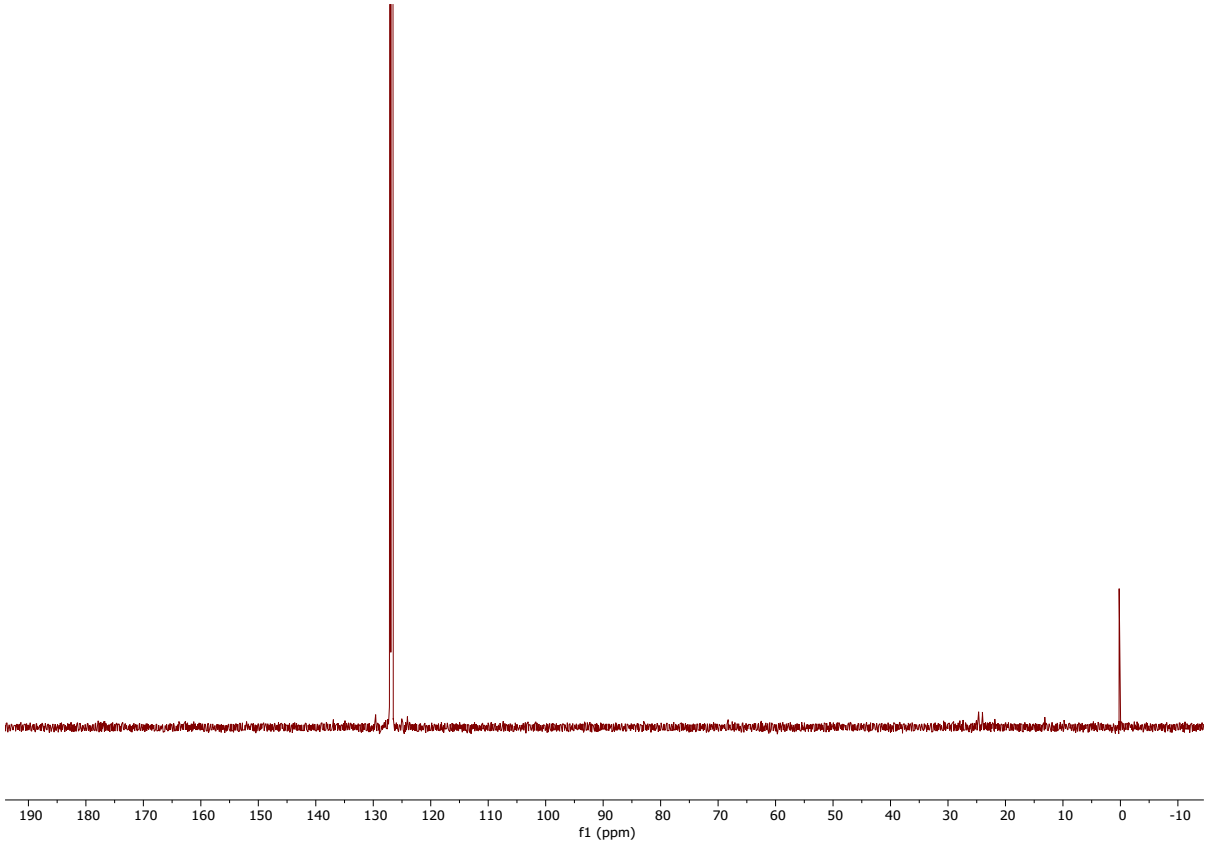

Figure S24. ^{13}C NMR spectrum of complex [Cr(SS-NHC=Se)$_3$] (**2**) in C_6D_6 at room temperature (500 MHz).

11. Thermogravimetric analyses

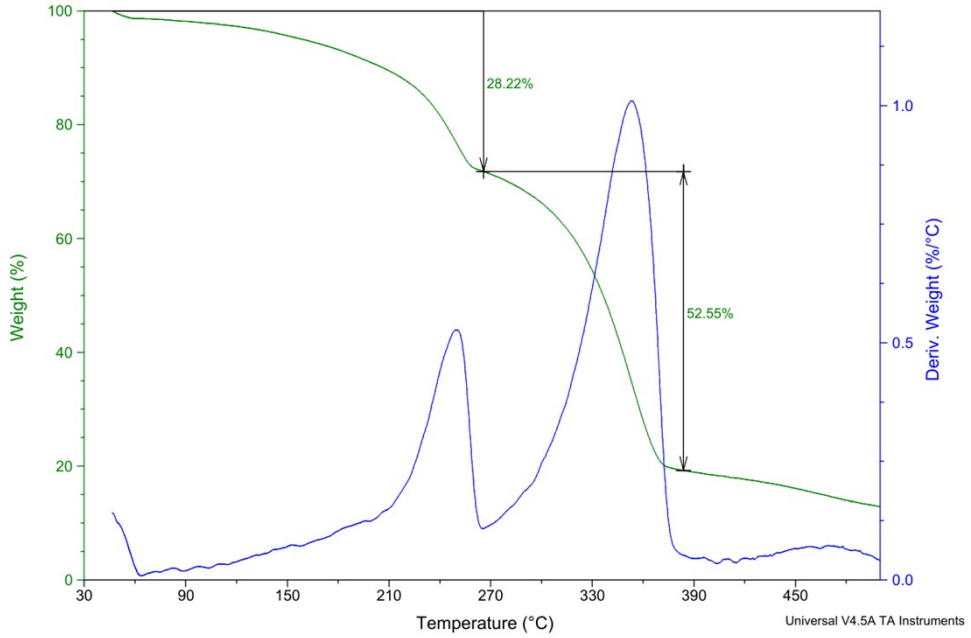

Figure S25. TGA of complex **1** in open air over 90 min, scanning the temperature from 30 °C to 500 °C. The title weight loss in the beginning is due to possible *n*-hexane in the crystals.

12. XPS Measurements:

X-ray photoelectron spectroscopy (XPS) was employed to analyse the surface electronic states and composition of complexes **1** and **2**. For the chromium core level, complex **1** exhibited Cr $2p_{3/2}$ and Cr $2p_{1/2}$ peaks at binding energies of 575.6 eV and 583.7 eV, respectively, while complex **2** showed these peaks at 575.5 eV and 584.5 eV. These values are consistent with Cr centres in an oxidation state close to +3, corroborating prior studies reporting Cr $2p_{3/2}$ binding energies near 575–576 eV for Cr(III) species. The slight shift in the Cr $2p_{1/2}$ peak of complex **2** to higher binding energy suggests subtle differences in the electronic environment, possibly due to selenium effects or coordination geometry.[S2a]

The carbon 1s spectrum for both complexes showed a peak at 283.9 eV, typically attributed to C-C or C-H bonds, indicating similar organic ligand environments in both samples. Nitrogen 1s peaks were observed at 399.7 eV in both complexes, corresponding to nitrogen in an amine or imine environment, confirming the integrity of N-containing ligands.

For sulfur, complex **1** displayed a S 2p peak at 161.8 eV, and complex **2** showed S 2p peaks at 161.5 eV and 165.5 eV, indicative of sulfur in different chemical states or coordination modes (for complex **1**, there is an extra NHC=S moiety, but it's absent in the case of complex **2**). The

minor peak at 152.5 eV detected in both spectra is assigned to silicon contamination from trace amounts of grease and is not related to the complexes themselves. [S2b]

Complex **2** additionally exhibited a Se 3d signal at 53.5 eV, confirming the presence of selenium in the structure, consistent with expected binding energies for metal-coordinated selenium species.[S2]

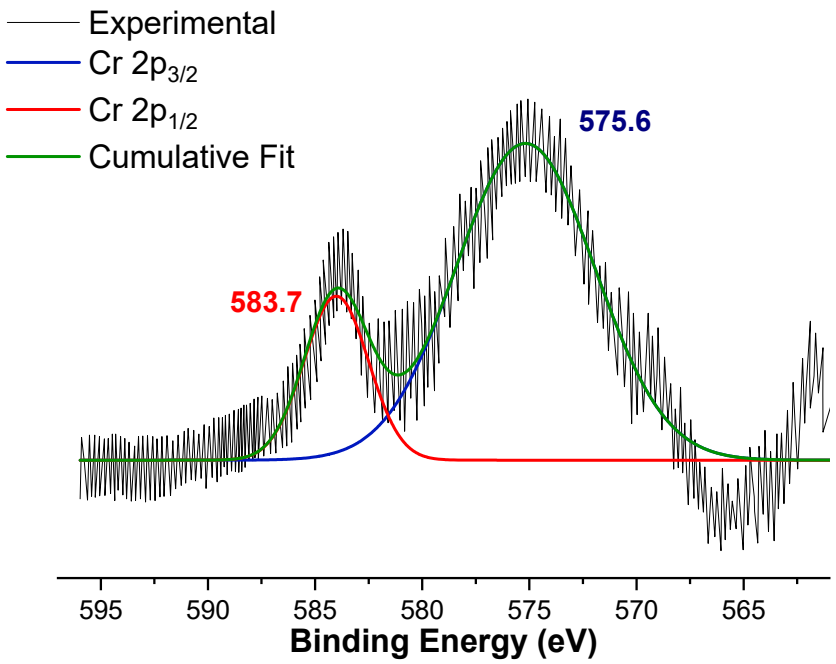

Figure S26. XPS plot of Cr-atom for complex **1**.

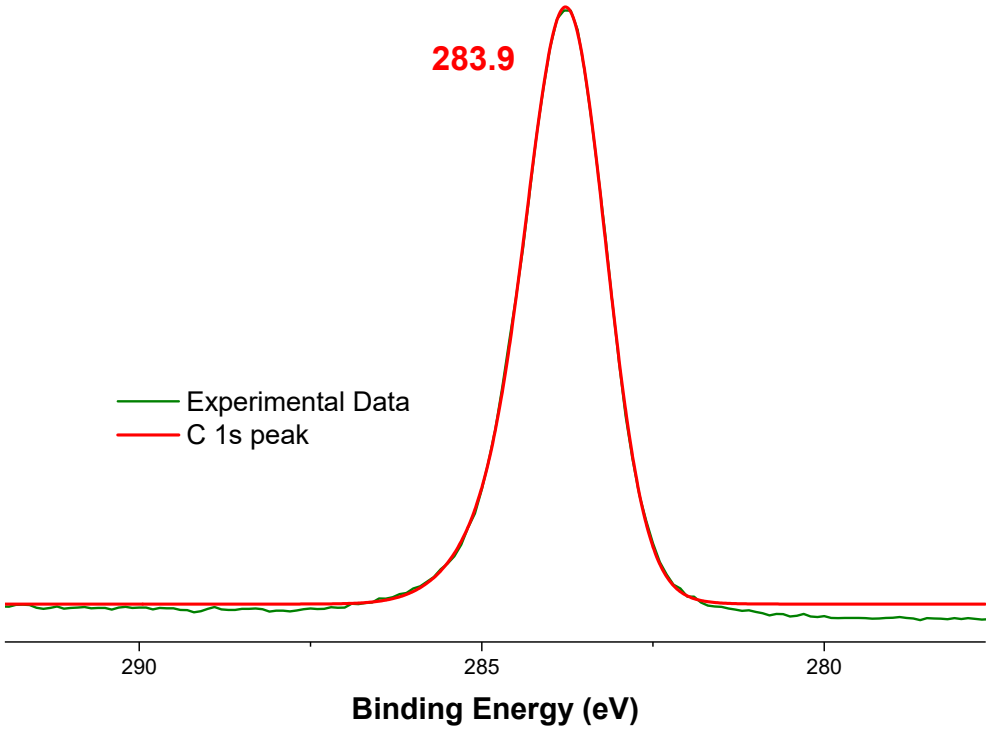

Figure S27. XPS pattern of C for the complex **1**.

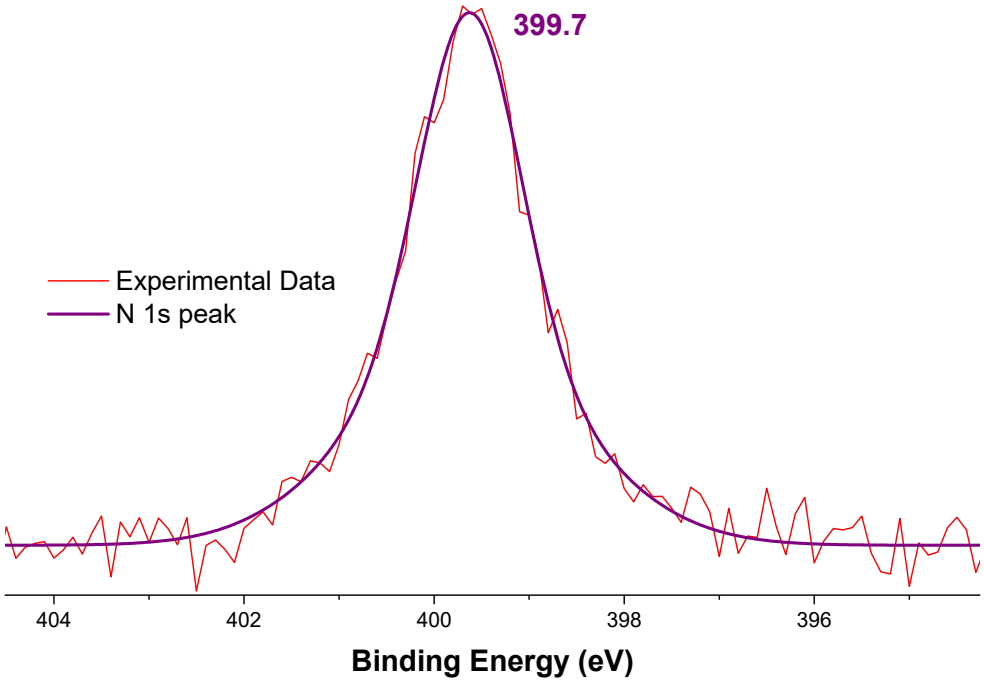

Figure S28. XPS pattern of N for the complex **1**.

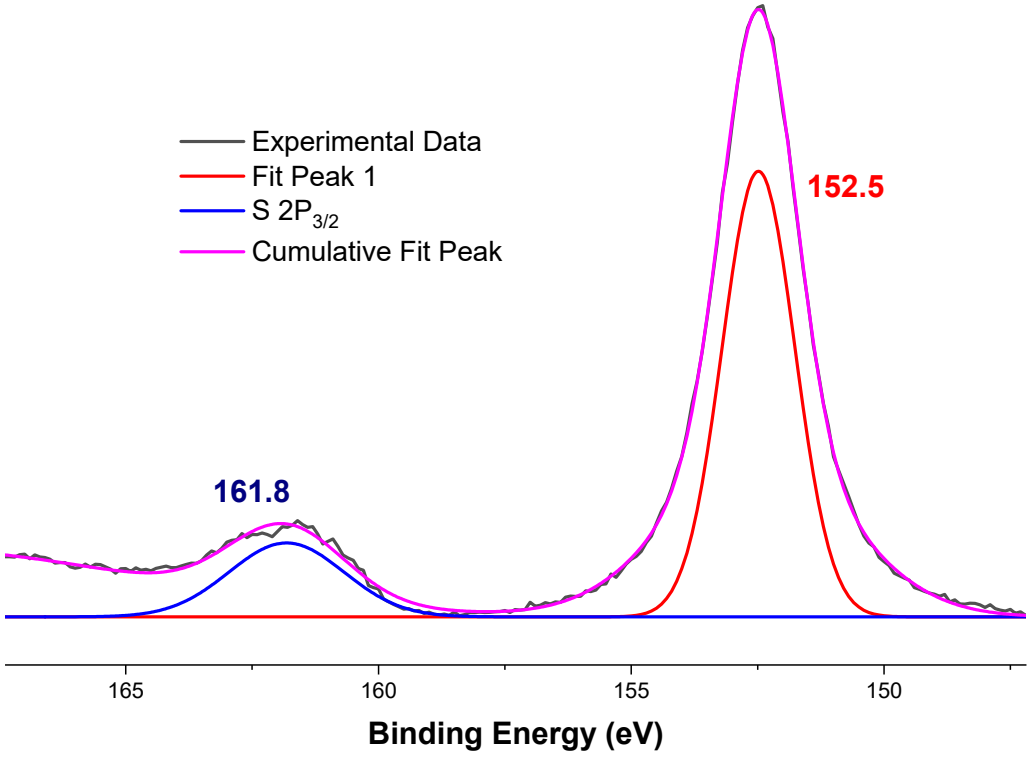

Figure S29. XPS pattern of S for the complex **1**.

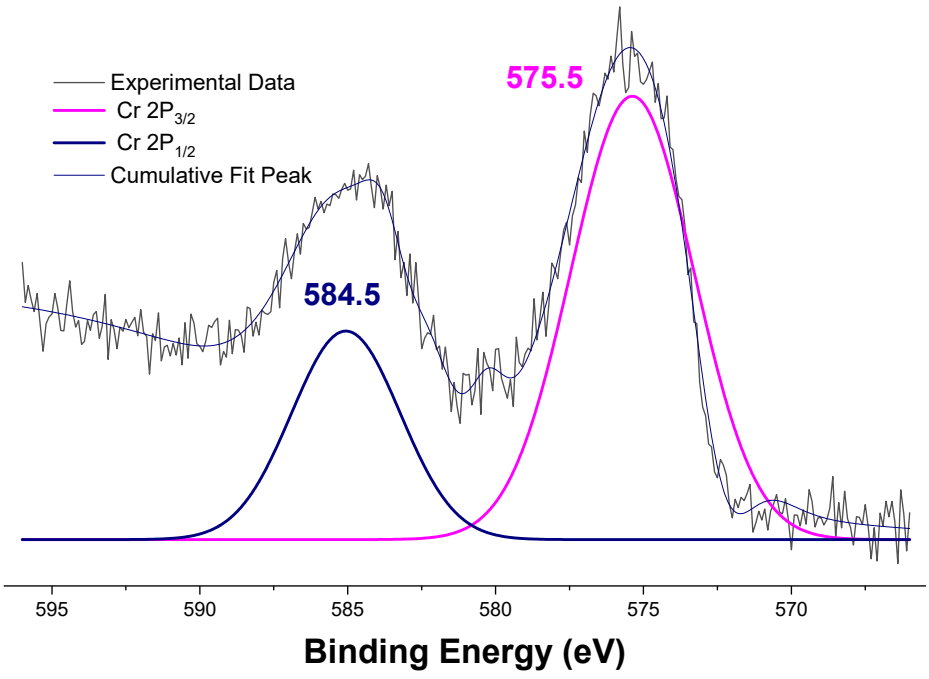

Figure S30. XPS plot of Cr(III) for complex **2**.

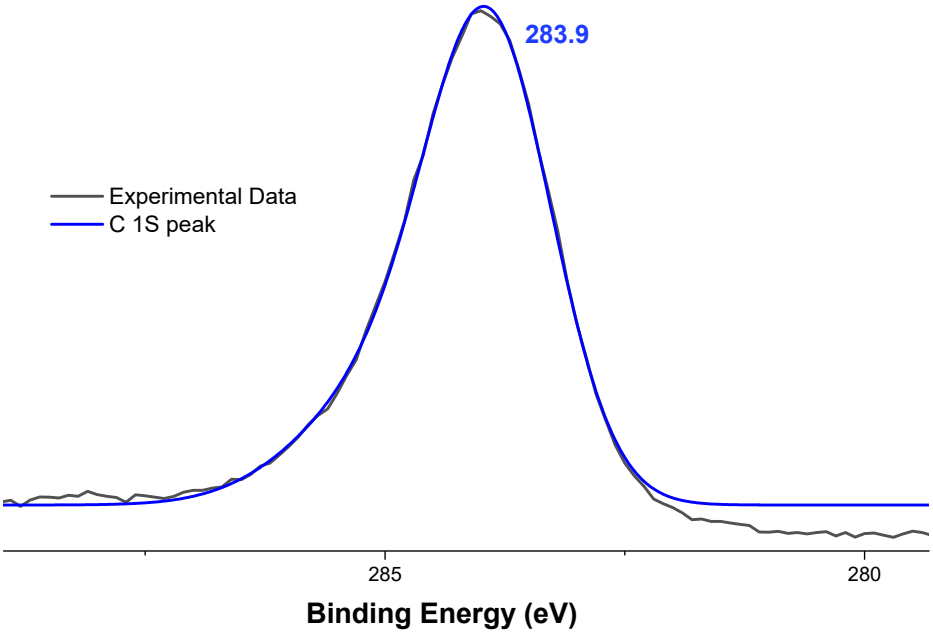

Figure S31. XPS pattern of C for the complex **2**.

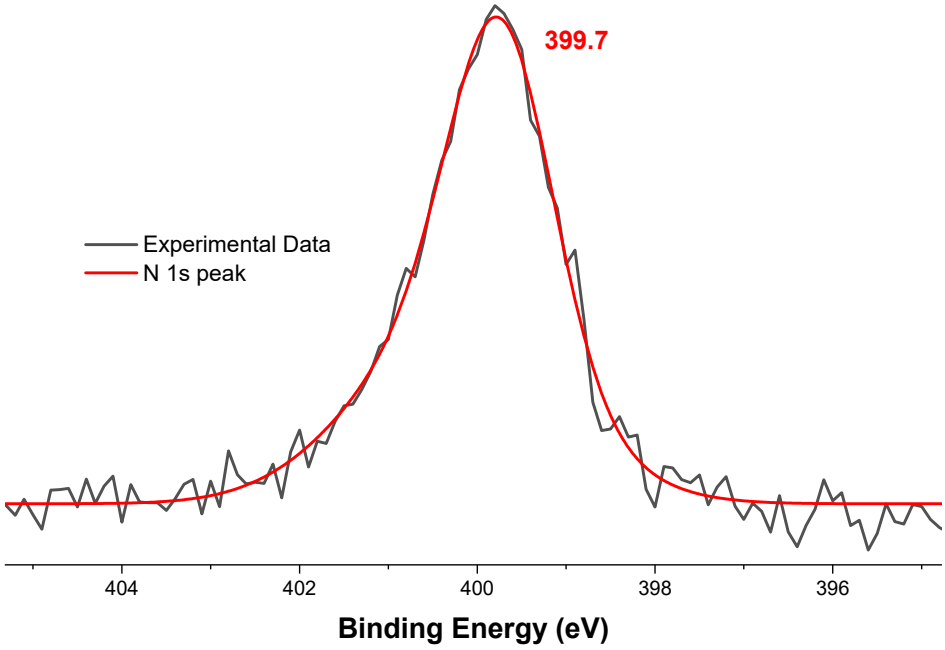

Figure S32. XPS pattern of N for the complex **2**.

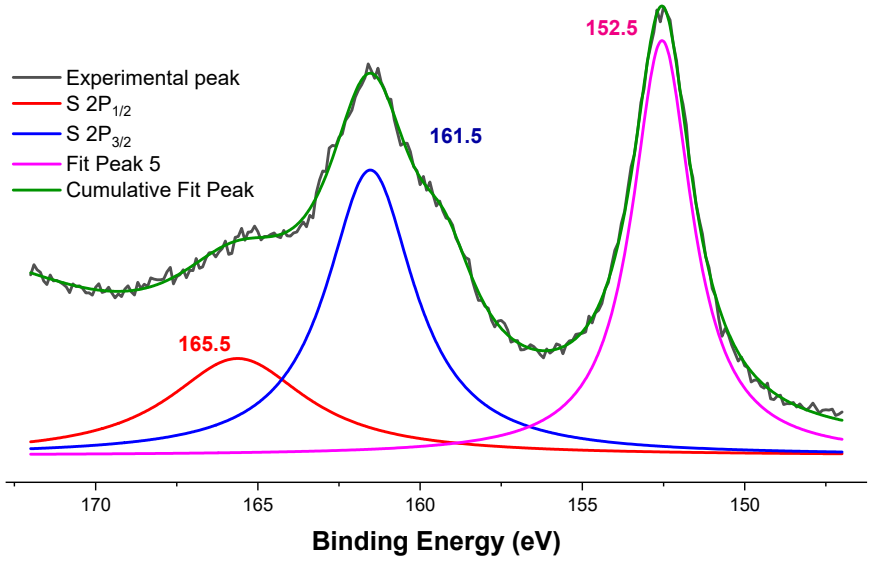

Figure S33. XPS pattern of S for the complex **2**.

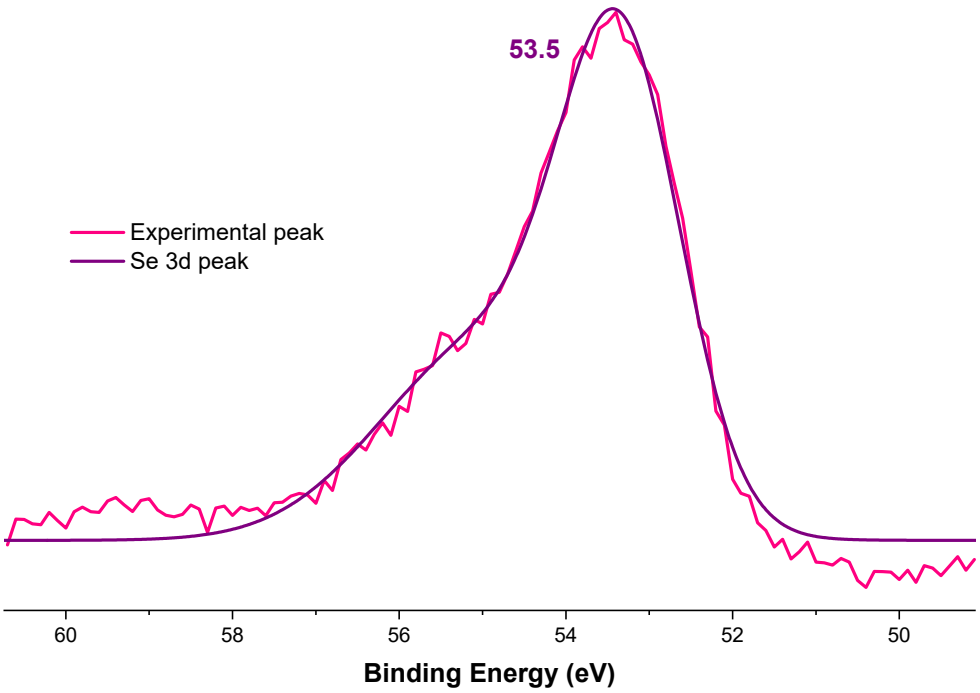

Figure S34. XPS pattern of Se for the complex **2**.

13. Computational analysis

Computational method:

Dipp groups in complexes **1-2** were replaced by Me groups in **1′-2′** for simplicity of density functional theory (DFT) calculation. The geometry optimisation of complexes [complex **1′**; complex **2′**] was done using B3LYP[S4-S6] hybrid functional with dispersion correction term D3(BJ)[S7-S8] along with the basis set Def2-TZVPP[S9] in neutral (q = 0) and charged (q = -1) state with different electronic spin states, using the Gaussian16 [S10] package in the gaseous phase with the help of DFT. The geometry optimisation is favoured by minima on the potential energy surface, followed by no negative frequency. The NBO 6.0 program[S11] is used to perform the NBO [S12] calculations of the complexes at B3LYP-D3(BJ)/Def2-TZVP level of theory using the optimised coordinates, and the Mulliken spin density plots are generated.

The geometry optimisation of complexes was done using B3LYP [S4-S6] hybrid functional with dispersion correction term D3(BJ)[S7-S8], along with the basis set Def2-TZVPP [S9] in neutral (q = 0) and charged (q = -1) state with different electronic spin states, using the Gaussian16 [S10] package in the gaseous phase with the help of DFT. The geometry optimisation is favoured by minima on the potential energy surface, followed by no negative frequency. The NBO 6.0 program[S11] is used to perform the NBO[S12] calculations of the complexes at B3LYP-D3(BJ)/Def2-TZVP level of theory using the optimised coordinates and the Mulliken spin density plots are generated. The previously optimised geometries at the B3LYP-D3(BJ)/Def2-TZVPP level are used to carry out EDA-NOCV [S13-S14] calculations at the B3LYP-D3(BJ)/TZ2P level of theory. ADF (Amsterdam Density Functional) program follows the Morokuma-type energy decomposition method, which involves the breakdown of overall energy into two components, ΔE_{prep} and ΔE_{int}, where E_{prep} gives the energy required to deform the fragments into acquired geometry and valence electronic configuration, while ΔE_{int} is the total interaction energy of those two fragments to form the complex again. ΔE_{int} is further split into four physical components in the ADF output file as,

$$\Delta E_{int} = \Delta E_{elstat} + \Delta E_{Pauli} + \Delta E_{orb} + \Delta E_{disp}$$

The term $\Delta E_{elestat}$ corresponds to the quasiclassical electrostatic interaction between the unperturbed charge distribution of the prepared fragments, and it is attractive. The Pauli repulsion arises due to the superposition of unperturbed electron densities of the isolated fragments to the wavefunction, which obeys the Pauli principle through explicit anti-symmetrisation and renormalisation of the product wave function. It consists of the

destabilising interaction between electrons on either fragment of the same spin. The orbital interaction emerged from the mixing of orbitals, charge transfer (donor-acceptor interaction between the occupied orbital of one fragment with the unoccupied orbital of the other), polarisation (empty/occupied orbital mixing on one fragment due to the presence of another fragment). The ΔE_{orb} can be split into irreducible representations of the point group of an interacting system.

$$\Delta E_{orb} = \sum_{r} \Delta E_{r}$$

Since we have used the metahybrid functional, it provides an additional metahybrid correction term $\Delta E_{\text{hybridS.}}$ This is because of the use of Hartree-Fock exchange in the functional, which can't be broken up and separated Using the NOCV approach along with EDA gives an insight into the pairwise contribution of the orbital interaction. This can be visualised as deformation densities ($\Delta\rho^{\text{orb}}$), which are the difference between the densities of the fragments before and after bond formation. It is given in the form of the total sum of complementary orbital pairs (Ψ_{-k}, Ψ_k) having equal and opposite eigenvalues, where the non-interacting orbitals will have zero eigenvalues,

$$\Delta\rho_{orb}(r) = \sum_{k} \Delta\rho_{k}(r) = \sum_{k=1}^{N/2} \nu_{k}[-\psi_{-k}^{2}(r) + \psi_{k}^{2}(r)]$$

This encompasses charge transfer, electron pair bonding, and polarization. The systematic partitioning of these physical components provides an informative and effective way to elucidate the nature of bonding, particularly in systems with distinct σ/π separation.

$$\Delta E_{Orb} = \sum_{k} \Delta E_{Orb}^{k} = \sum_{k} \nu_{k}\left[- F_{-k,-k}^{TS} + F_{k,k}^{TS}\right]$$

The eigenvalues are obtained through the diagonalisation of the difference density matrix of the system. Similarly, the pairwise orbital interactions associated with the deformation density can represent the total orbital interaction. The $- F_{-k,-k}^{TS}$ and $F_{k,k}^{TS}$, terms are diagonal transition state Kohn-Sham elements corresponding to NOCVs with eigenvalues $-\nu_k$ and ν_k, respectively. This method and analyses have been applied for low-spin Fe(III)-radical complex containing three anionic dithiolene radical ligands.[S1b]

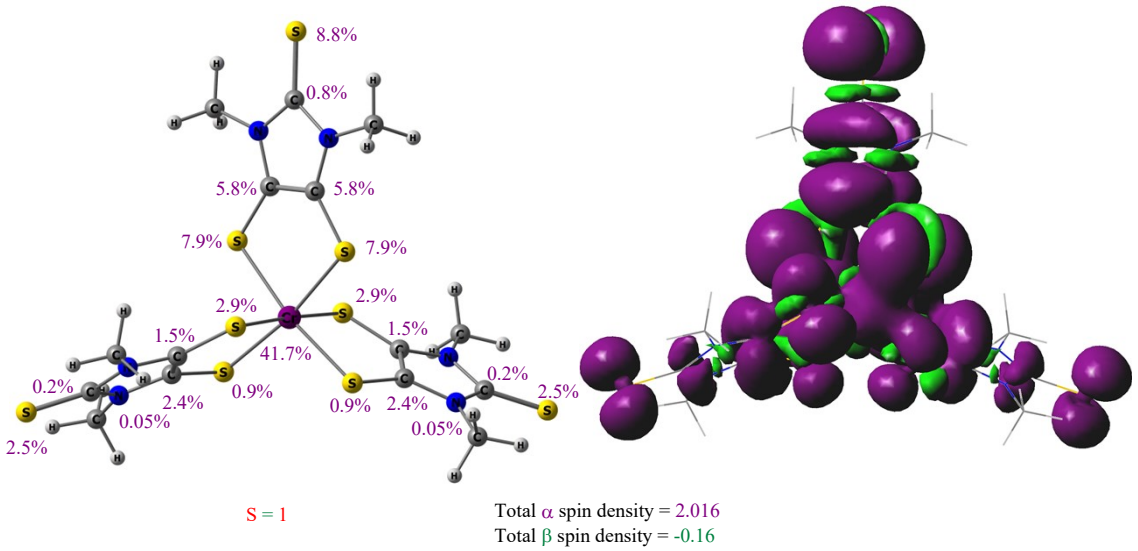

Figure S35. The Mulliken spin densities of complex **1′** (q = 0, S = 1) were calculated at B3LYP-D3(BJ)/def2-TZVPP level of theory. The α spin density percentage is represented on the left side, and the spin density plot is given on the right side. (Purple colour represents α spin density, and green colour denotes the β spin density). E = S.

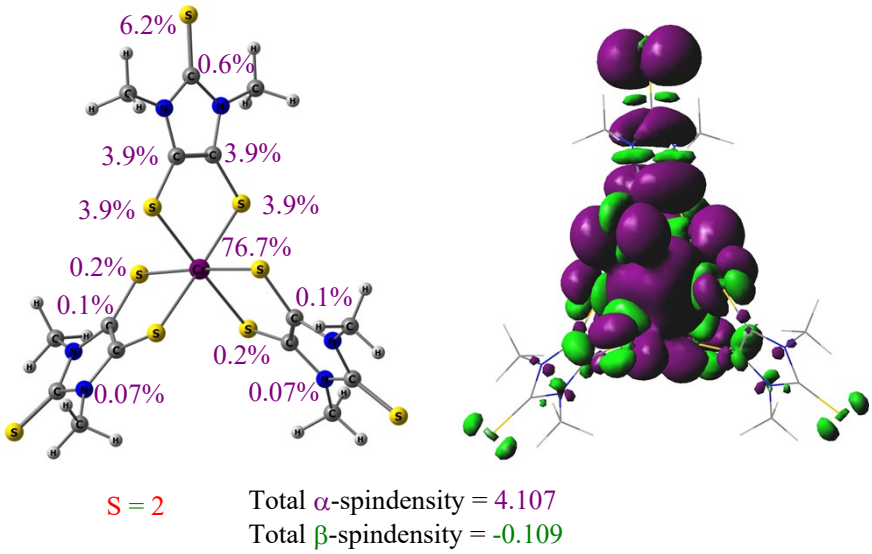

Figure S36. The Mulliken spin densities of complex **1′** (q = 0, S = 2) calculated at B3LYP-D3(BJ)/def2-TZVPP level of theory. The α spin density percentage is represented on the left side, and the spin density plot is given on the right side. (Purple colour indicates α spin density and green colour denotes the beta spin density). E = S.

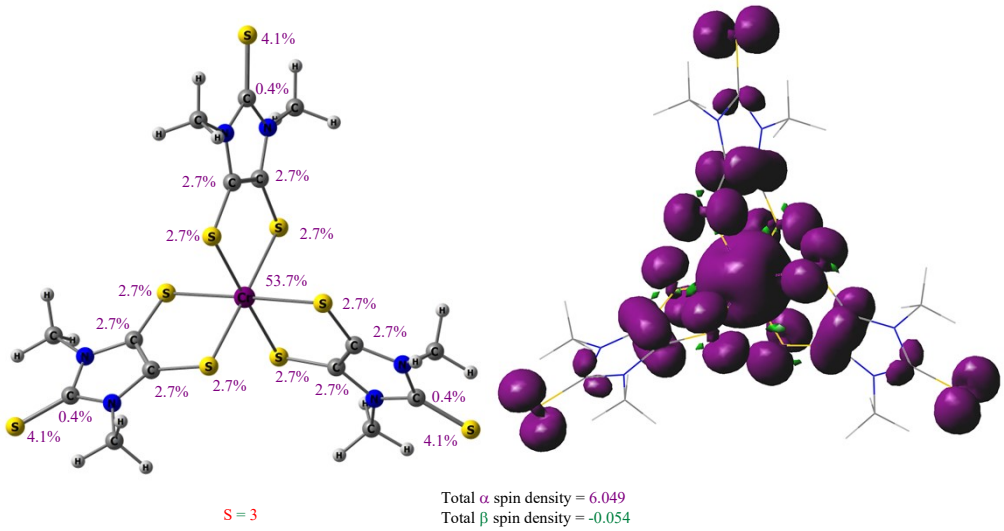

Figure S37. The Mulliken spin densities of complex **1′** (q = 0, S = 3) were calculated at B3LYP-D3(BJ)/def2-TZVPP level of theory. The α spin density percentage is represented on the left side, and the spin density plot is given on the right side. (Purple colour indicates α spin density and green ccolourdenotes the beta spin density). E = S.

Table S7. The energy differences. Dipp groups in complexes **1-2** were replaced by Me groups in **1′-2′** for simplicity of density functional theory (DFT) calculation.

	Singlet	Triplet	Septet	Quintet
Complex **1′**	-5540.1013923	-5540.1053867	-5540.1553244	-5540.1418184
		2.5(Singlet-Triplet) (31.3 with septet)	33.8(Singlet-Triplet) (31.33 kcal/mol with triplet) 8.475 kcal/mol with quintet	25.4 (Singlet-Triplet) (22.9 kcal/mol with triplet)
Complex **2′**	-11550.1972326	-11550.2581672	-11550.2524768	-11550.2552059
		38.2 (Singlet-Triplet) (3.6 kcal/mol with septet)	34.6 (Singlet-Triplet) (1.71 kcal/mol with quintet)	36.4(Singlet-Triplet) (1.85 kcal/mol with triplet)

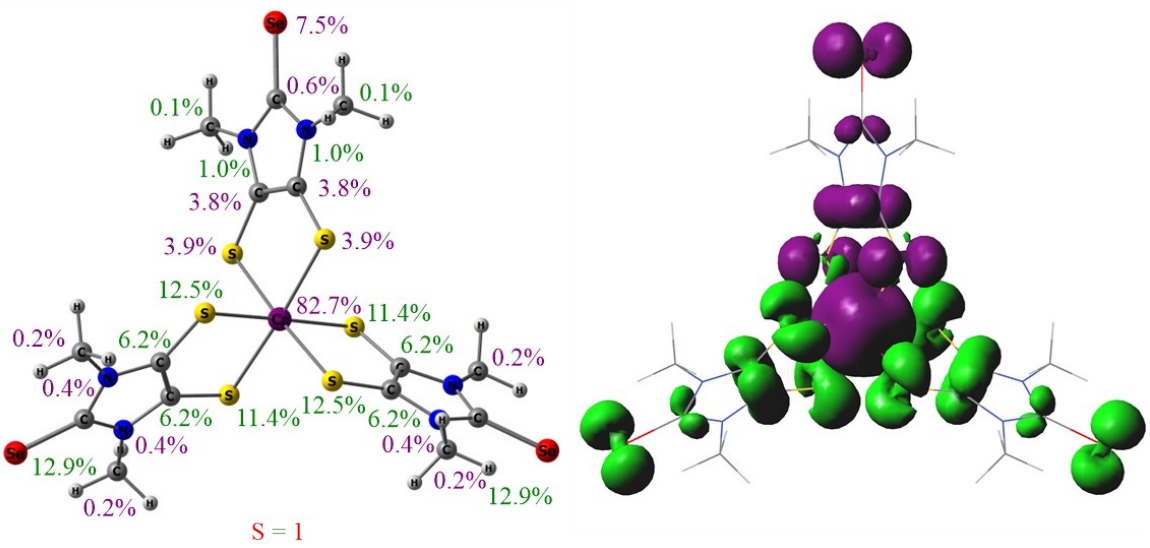

Figure S38. The Mulliken spin densities of complex **2′** (q = 0, S = 1) calculated at B3LYP-D3(BJ)/def2-TZVPP level of theory. The α spin density percentage is represented on the left side, and the spin density plot is given on the right side. (Purple colour indicates α spin density and green colour denotes the beta spin density). E = Se

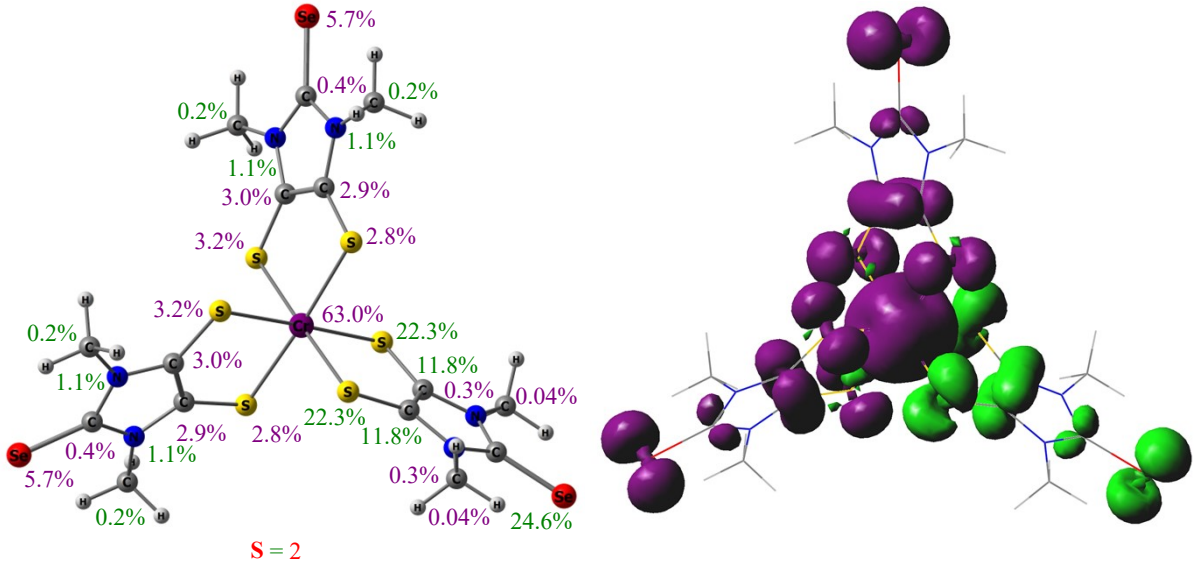

Figure S39. The Mulliken spin densities of complex **2′** (q = 0, S = 2) calculated at B3LYP-D3(BJ)/def2-TZVPP level of theory. The α spin density percentage are represented in the left side and the spin density plot given in the right side. (Purple color indicates α spin density and green color denote the beta spin density). E = Se

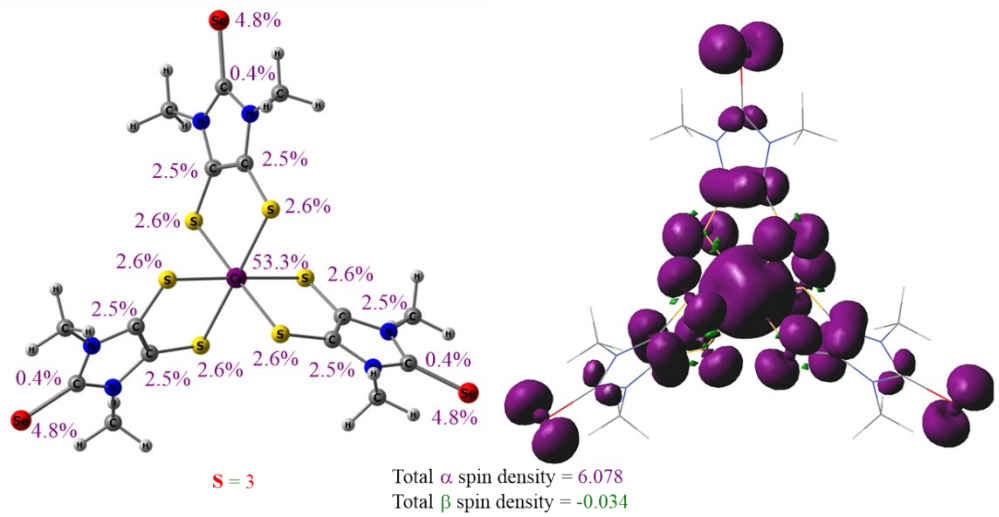

Figure S40. The Mulliken spin densities of complex **2′** (S = 3) were calculated at B3LYP-D3(BJ)/def2-TZVPP level of theory. The α spin density percentage is represented on the left side, and the spin density plot is given on the right side. (Purple colour indicates α spin density and green colour denotes the beta spin density). E = Se

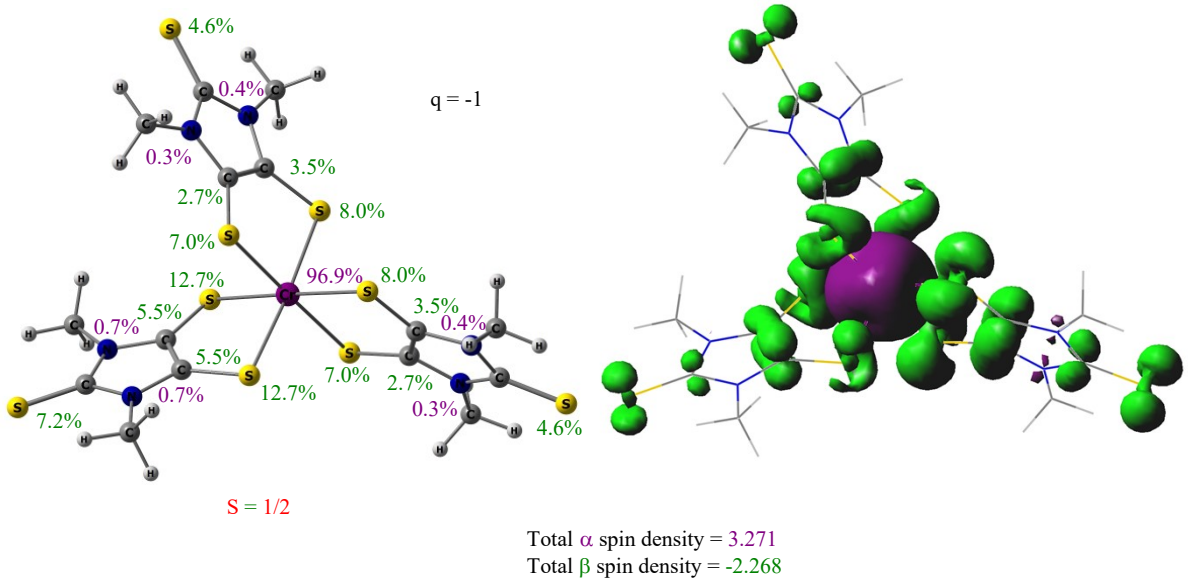

Figure S41. The Mulliken spin densities of anionic complex **(1′)**$^{\bullet-}$ (q = -1, S = 1/2) calculated at B3LYP-D3(BJ)/def2-TZVPP level of theory. The α spin density percentage is represented on the left side, and the spin density plot is given on the right side. (Purple colour indicates α spin density and green colour denotes the beta spin density). E = Se.

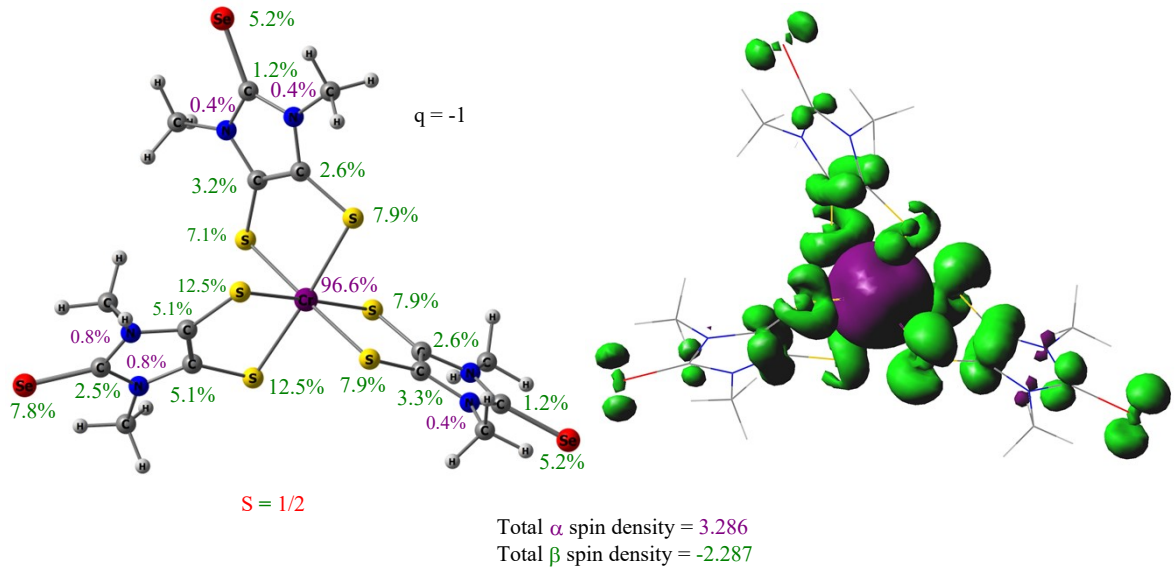

Figure S42. The Mulliken spin densities of anionic complex $(\mathbf{2'})^{\bullet-}$ (q = -1, S = 1/2) were calculated at B3LYP-D3(BJ)/def2-TZVPP level of theory. The α spin density percentage is represented on the left side, and the spin density plot is given on the right side. (Purple colour indicates α spin density and green colour denotes the beta spin density). E = Se.

$\Delta\rho$, CrL_3 (S)	**CrL_2^+ (D)**	**L^- (D)**
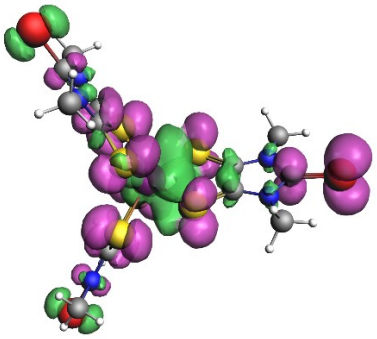 $\Delta\rho_{(1)}$ $\Delta E_{orb(1)}$ = -31.2; $\lvert\nu_1\rvert$ = 0.66/0.74	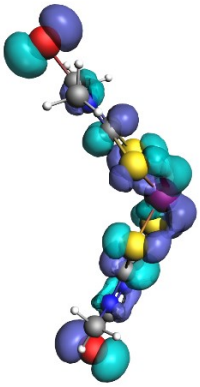 SOMO (ε = -8.22 eV)	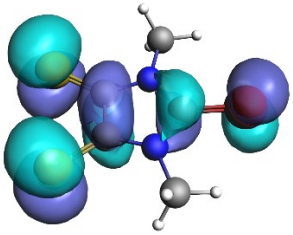 SOMO (ε = -0.02 eV)
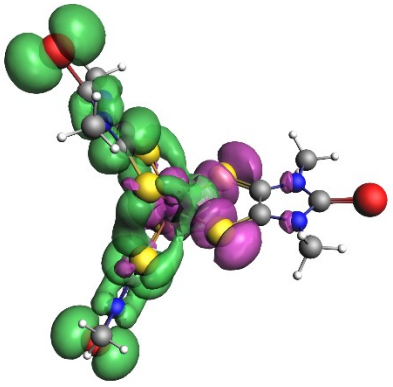	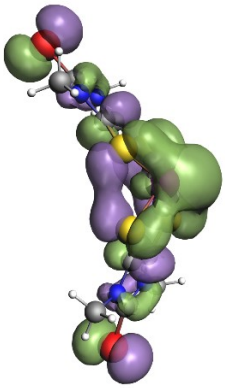	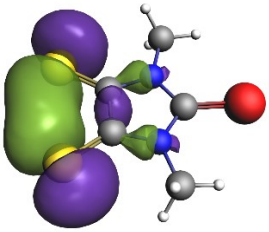 HOMO-2 (ε = -2.45 eV)

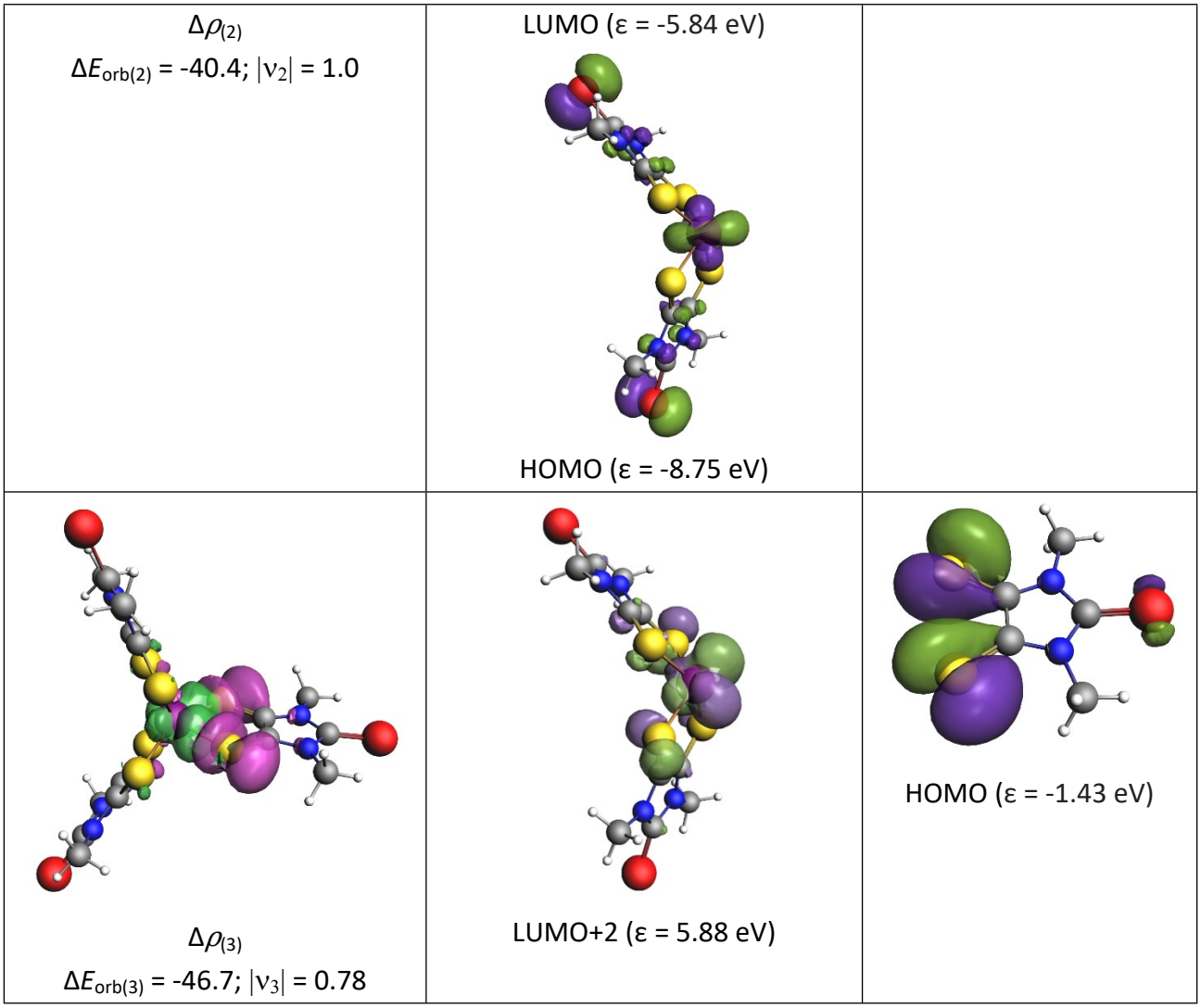

Figure S43. The shape of the deformation densities $\Delta\rho_{(1)-(3)}$ that correspond to $\Delta E_{orb(1)-(3)}$, and the associated fragments orbitals of complex **2′** (S) with charged $(CrL_2)^+$ (D) and L^- (D) in doublet state at the B3LYP-D3(BJ)/TZ2P level. The isosurface value is 0.001 au for $\Delta\rho_{(1-3)}$ and 0.0005 au for $\Delta\rho_{(2)}$. The eigenvalues $|\nu_n|$ give the size of the charge migration in e. The charge flow direction of the deformation densities is from pink → green, the half-filled orbitals (SOMO) are represented in the lavender and cyan colour combination. Dipp groups in complex **2** were replaced by Me groups in **2′** for simplicity of density functional theory (DFT) calculation.

Table S8. The EDA-NOCV result of complex **2′** (S) at the B3LYP-D3(BJ)/TZ2P level. Energies are in kcal/mol.[a]The values in the parentheses show the contribution to the total attractive interaction ΔE_{elstat} + ΔE_{orb} +ΔE_{disp}, and the [b] value in the parentheses shows the contribution to the total orbital interaction. Dipp groups in complex **2** were replaced by Me groups in **2′** for simplicity of density functional theory (DFT) calculation.

Energy	**Interaction**	**CrL_2^+ (D) + L^- (D)**
ΔE_{int}		-179.8

ΔE_{Pauli}		190.0
ΔE_{elstat}		-200.6 (54.3%)
ΔE_{disp}		-16.3 (4.4%)
ΔE_{orb}		-152.8 (41.3%)
$\Delta E_{\text{orb(1)}}$	$CrL_2^+ \leftrightarrow L^-$ π e-share	-31.2 (20.4%)
$\Delta E_{\text{orb(2)}}$	$CrL_2^+ \leftarrow L^-$ σ e- donation	-40.4 (26.4%)
$\Delta E_{\text{orb(3)}}$	$CrL_2^+ \leftarrow L^-$ σ e- donation	-46.7 (30.6%)
$\Delta E_{\text{orb(rest)}}$		-34.5 (22.6%)

Δρ, CrL_3 (D)	**CrL_2 (S)**	**L^- (D)**
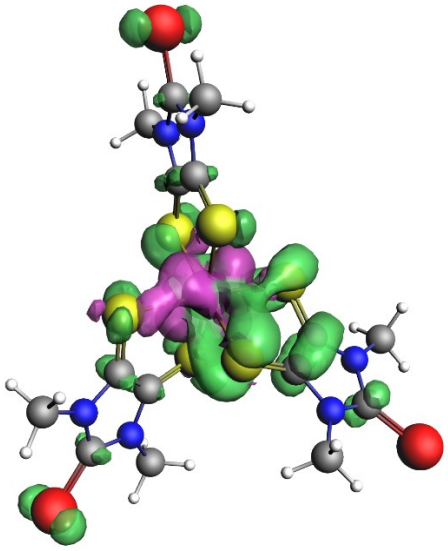 $\Delta\rho_{(1)}$ $\Delta E_{\text{orb(1)}}$ = -32.9; $\lvert\nu_1\rvert$ = 0.82/0.65	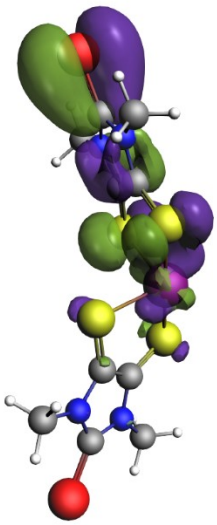 HOMO-6 (ε = -6.85 eV) 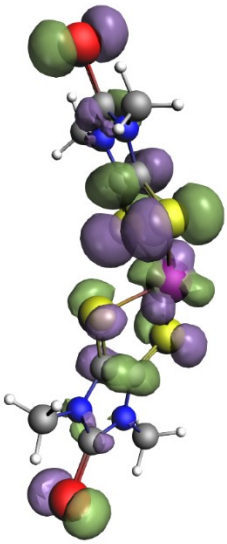	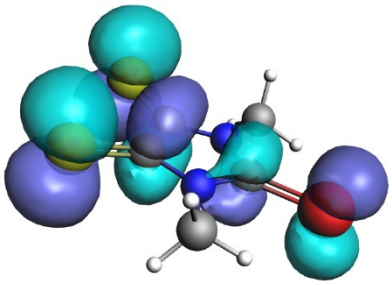 SOMO (ε = -0.23 eV)

<table>
<tr><td></td><td>LUMO (ε = -4.20 eV)</td><td></td></tr>
<tr><td> 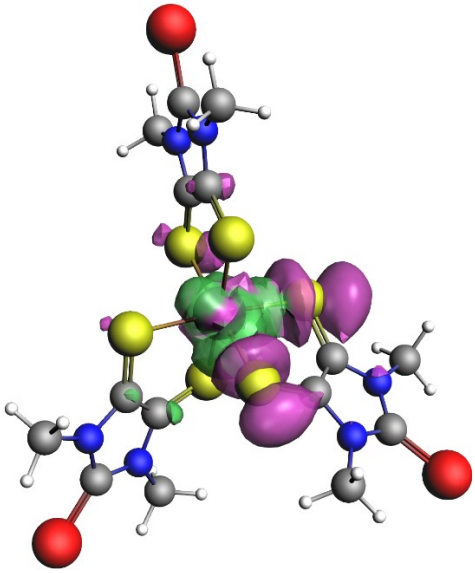
$\Delta\rho_{(2)}$
$\Delta E_{orb(2)}$ = -30.5; $|\nu_2|$ = 0.32/0.52</td><td> 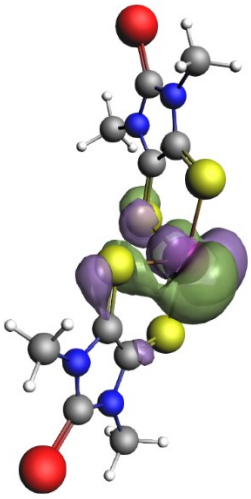
LUMO+2 (ε = -2.67 eV)</td><td> 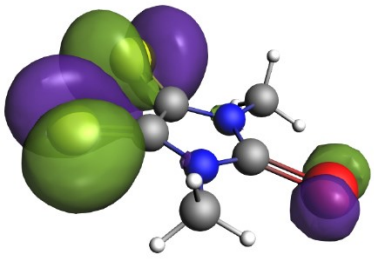
HOMO (ε = -1.76 eV)</td></tr>
<tr><td> 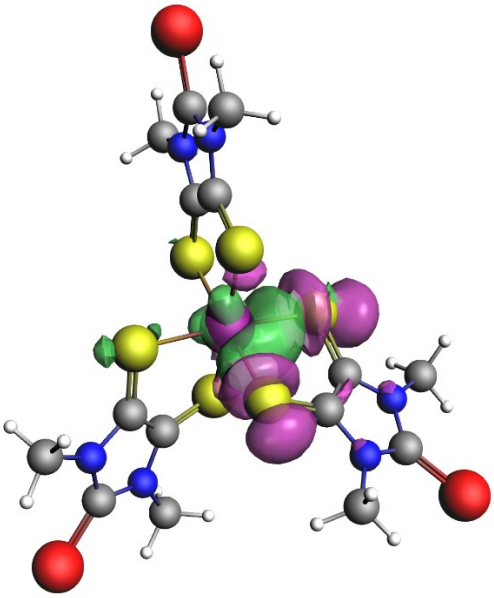
$\Delta\rho_{(3)}$
$\Delta E_{orb(3)}$ = -24.4; $|\nu_3|$ = 0.25/0.26</td><td> 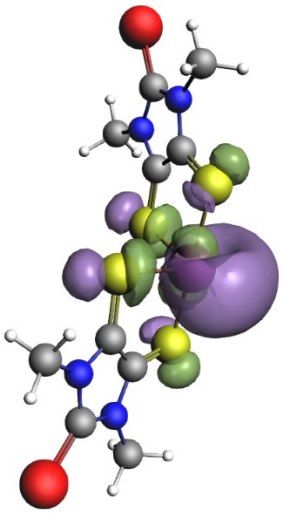
LUMO+3 (ε = -2.26 eV)</td><td> 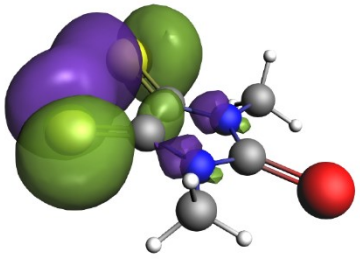
HOMO-1 (ε = -2.39 eV)</td></tr>
</table>

Figure S44. The shape of the deformation densities $\Delta\rho_{(1)-(3)}$ that correspond to $\Delta E_{orb(1)-(3)}$, and the associated fragments orbitals of complex $(\mathbf{2'})^{\bullet-}$ (D) with charged CrL_2 (S) and L^- (D) in singlet and doublet state, respectively at the B3LYP-D3(BJ)/TZ2P level. The isosurface value is 0.001 au for $\Delta\rho_{(1-3)}$. The eigenvalues $|\nu_n|$ give the size of the charge migration in e. The charge flow direction of the deformation densities is from pink → green, the half-filled orbitals (SOMO) are represented in the lavender and cyan colour combination. E = Se.

Table S9. The EDA-NOCV result of complex (**2′**)$^{\bullet-}$ (D) at the B3LYP-D3(BJ)/TZ2P level. Energies are in kcal/mol.[a]The values in the parentheses show the contribution to the total attractive interaction ΔE_{elstat} + ΔE_{orb} +ΔE_{disp}, and the [b] value in the parentheses shows the contribution to the total orbital interaction. Dipp groups in complex **2** were replaced by Me groups in **2′** for simplicity of density functional theory (DFT) calculation.

Energy	Interaction	CrL_2 (S) + L^- (D)
ΔE_{int}		-114.2
ΔE_{Pauli}		169.2
ΔE_{elstat}		-137.9 (48.6%)
ΔE_{disp}		-19.1 (6.7%)
ΔE_{orb}		-126.5 (44.7%)
$\Delta E_{orb(1)}$	$CrL_2 \rightarrow L^-$ π e^- donation (HOMO→SOMO)	-32.9 (26.0%)
$\Delta E_{orb(2)}$	$CrL_2 \leftarrow L^-$ σ e^- donation	-30.5 (24.1%)
$\Delta E_{orb(3)}$	$CrL_2 \leftarrow L^-$ σ e^- donation	-24.4 (19.3%)
$\Delta E_{orb(rest)}$		-38.7 (30.6%)

14. Hirshfeld Plots:

The parameter d_i (internal distance) represents the distance from a given point on the Hirshfeld surface to the nearest nucleus within the same molecule. Meanwhile, d_e (external distance) measures the distance from that point to the nearest nucleus in a neighboring molecule. These distances are critical for analysing the nature and strength of intermolecular interactions. In the Hirshfeld surface maps of d_i and d_e, the red regions correspond to close contacts (short distances), green indicates intermediate separations, and blue denotes longer distances. An additional key metric is the normalised contact distance (d_{norm}), which integrates d_i, d_e, and the van der Waals radii of the interacting atoms. The color scale of the d_{norm} surface ranges from red (short contacts), through white (contacts close to van der Waals separations), to blue (long contacts), visually highlighting regions of significant intermolecular interactions. The term, d_{norm} is defined by the following equation:

$$d_{norm} = \frac{d_i - r_i^{vdW}}{r_i^{vdW}} + \frac{d_e - r_e^{vdW}}{r_e^{vdW}}$$

Curvedness quantifies the degree of local surface curvature on the Hirshfeld surface. Low curvedness values, typically depicted in green or red, correspond to relatively flat regions and

may indicate areas of π–π stacking or planar molecular packing. High values, shown in blue, highlight sharp edges or significant surface features. The ***shape index*** offers a qualitative representation of surface topology, distinguishing between concave (red) and convex (blue) regions. This descriptor is particularly useful for identifying complementary interaction sites, such as alternating concave and convex patterns characteristic of π–π interactions. The ***fragment patch*** feature assigns unique colors to areas of the Hirshfeld surface in contact with individual neighboring molecules, thereby facilitating the visual identification of distinct intermolecular interactions within the crystal structure.

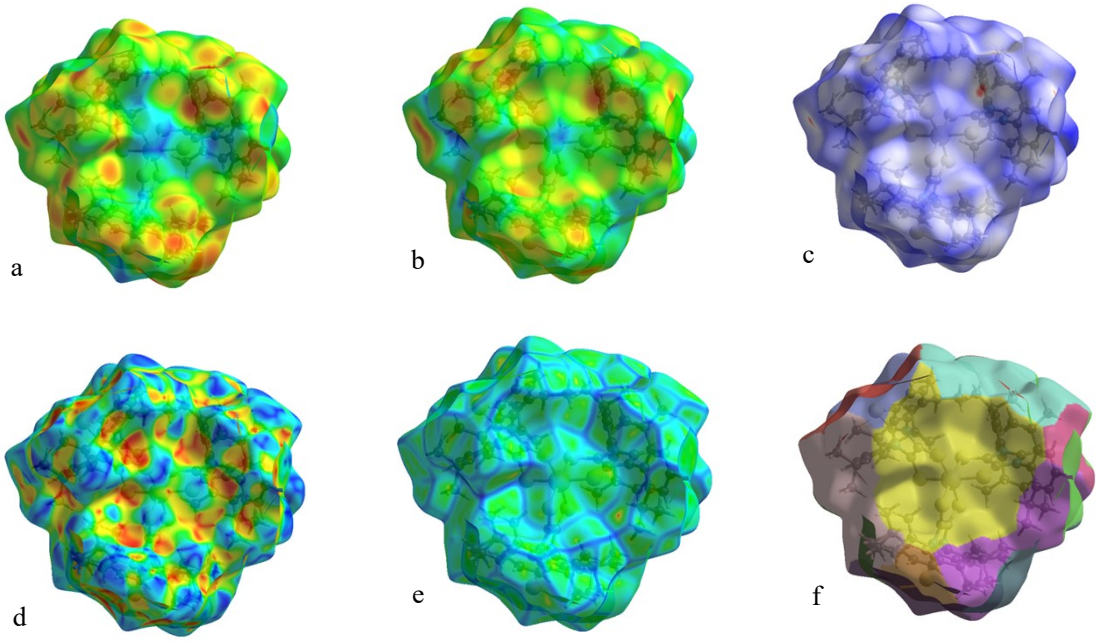

Figure S45. A compilation of (a) d_i – internal distance, (b) d_e – external distance, (c) d_{norm} – normalized contact distance, (d) Shape index, (e) Curvedness and (f) Fragment patch – all mapped on the Hirshfeld surface of **1**.

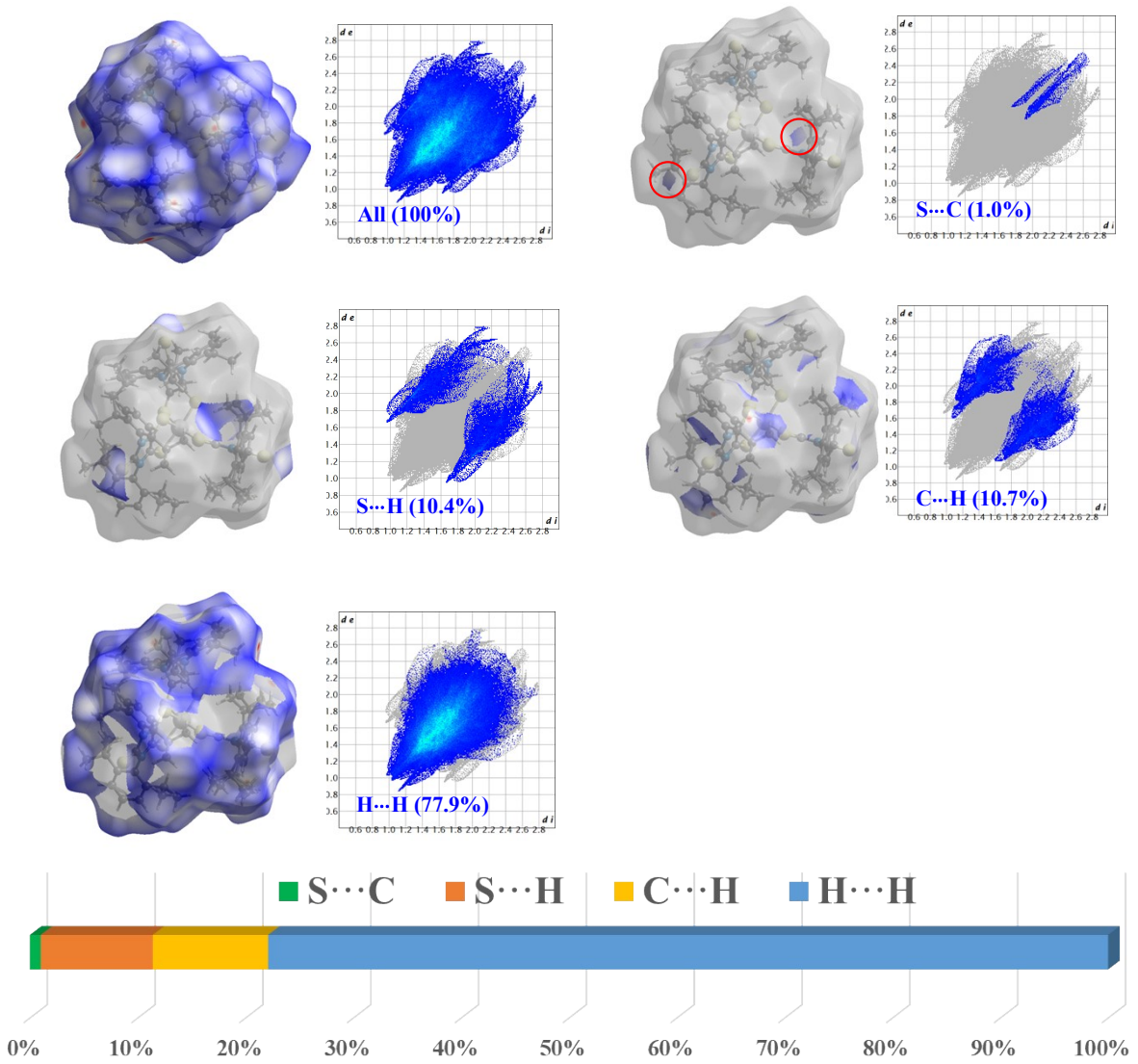

Figure S46. 2-D fingerprint plots of complex **1** generated using CrystalExplorer, highlighting the relative contributions of specific intermolecular interactions. The full fingerprint is outlined in gray, while individual interaction types are color-coded, with their percentage contributions to the Hirshfeld surface area annotated in blue. The distance range considered spans 0.8–2.8 Å.

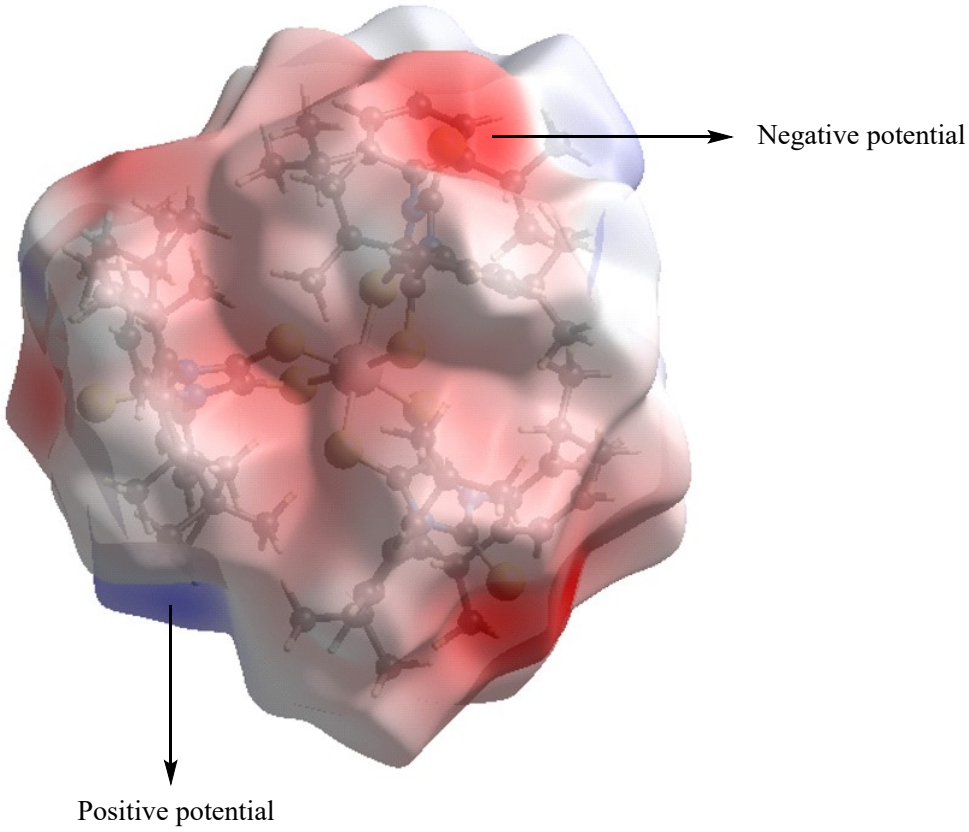

Figure S47. Hirshfeld surface mapped with electrostatic potential (HF/ST0-3G): -0.0971 to +0.2843 au.

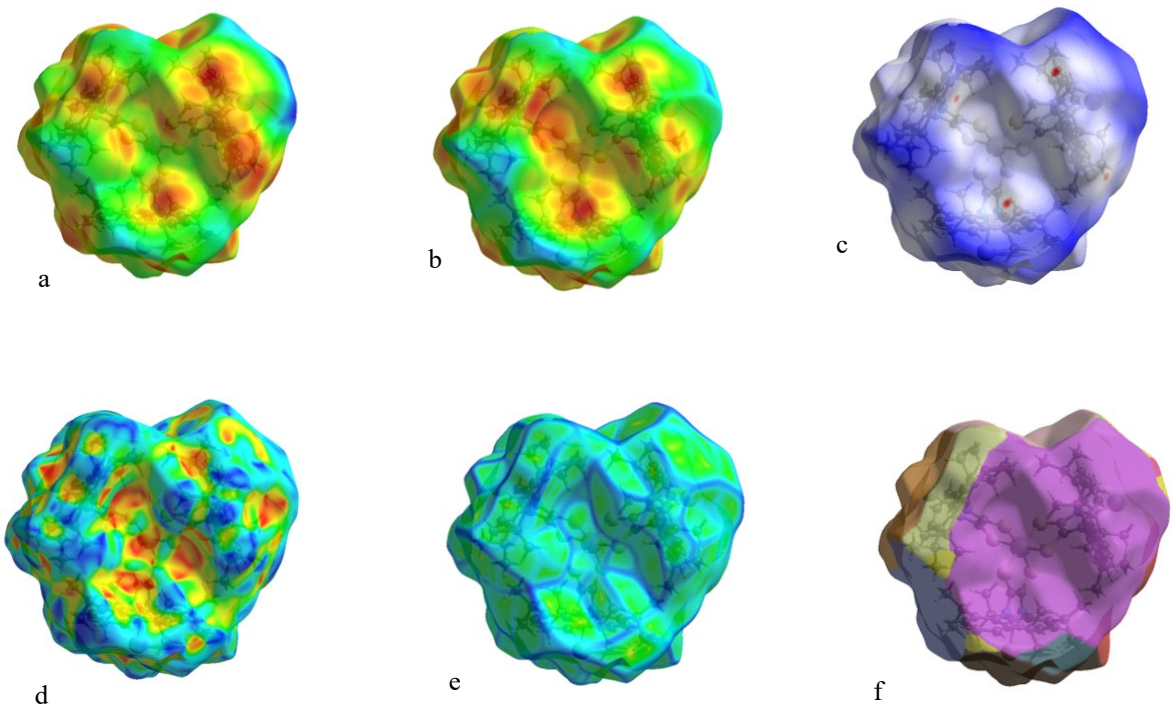

Figure S48. A compilation of (a) d_i – internal distance, (b) d_e – external distance, (c) d_{norm} – normalized distance, (d) Shape index, (e) Curvedness, (f) Fragment patch mapped on the Hirshfeld surface of complex **2**.

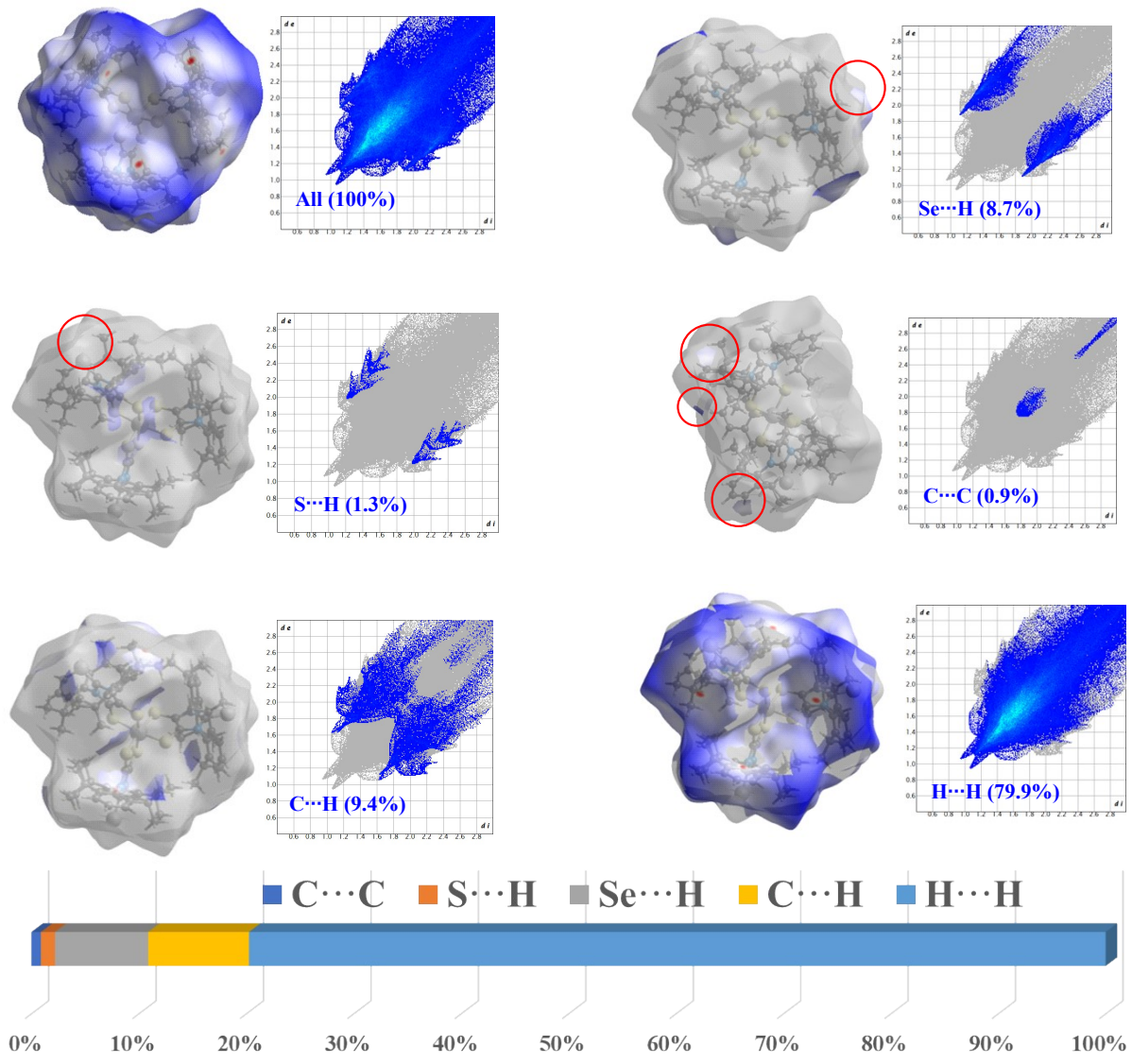

Figure S49. 2D Fingerprint plots of complex **2** generated using Crystal Explorer, highlighting the relative contributions of specific intermolecular interactions. The full fingerprint is outlined in grey, while individual interaction types are color-coded, with their percentage contributions to the total Hirshfeld surface area annotated in blue. The distance range considered spans 0.9 to 2.9 Å.

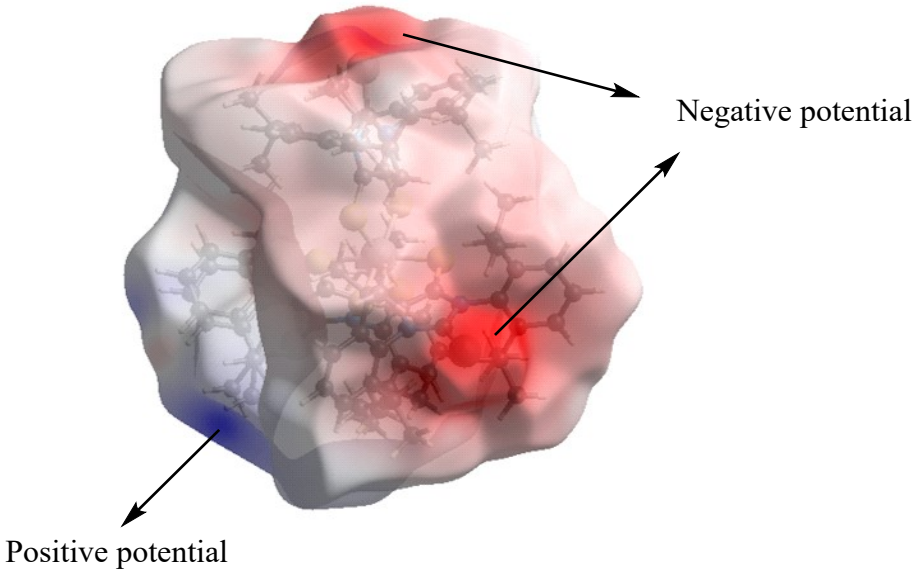

Figure S50. Hirshfeld surface mapped with electrostatic potential (HF/STO-3G); −0.1106 to 0.2146 au.

Results and Discussion

The Hirshfeld surfaces and corresponding fingerprint plots were generated using ***CrystalExplorer 21*** based on the crystallographic information files (CIFs) of each complex. **Figure S45** and **Figure S46** present the mapped Hirshfeld surfaces of complex **1** and complex **2**, respectively, displaying (a) d_i (internal distance), (b) d_e (external distance), (c) d_{norm} (normalised contact distance), (d) shape index, (e) curvedness, and (f) fragment patches. These analyses reveal numerous regions of intermolecular interactions contributing to crystal stabilization, such as van der Waals interactions. In particular, the d_{norm} surfaces (**Figure 1c** and **Figure S48c**) visually highlight close contacts, while **Figure S46** and **Figure S49** provide a detailed breakdown of interaction types and their relative contributions for complexes **1** and **2**, respectively.

For complex **1**, the Hirshfeld surface contact contributions are as follows: S···C (1.0%), S···H (10.4%), C···H (10.7%), and H···H (77.9%). In complex **2**, the contributions are: C···C (0.9%), S···H (1.3%), Se···H (8.7%), C···H (9.4%), and H···H (79.9%). The electrostatic potential mapped onto the Hirshfeld surfaces – calculated at the HF/STO-3G level – are presented in **Figure S47** (complex 1, −0.0971 to +0.2843 au) and **Figure S50** (complex **2**, −0.1106 to +0.2146 au). In both complexes, regions of negative electrostatic potential (shown in red) are

observed around the C=S (complex **1**) and C=Se (complex **2**) bonds, indicating electron-rich centers due to lone pairs and electronegativity. These atoms are likely to act as hydrogen bond acceptors in noncovalent interactions with electropositive hydrogen atoms, particularly those from the DIPP (2,6-diisopropylphenyl) groups of adjacent molecules, which exhibit positive potential regions (blue). Such complementary interactions, including C–H···S and C–H···Se contacts, can play a significant role in guiding the packing arrangement and enhancing the overall stability of the crystal structure. Notably, the S···H interaction accounts for 10.4% in complex **1**, and the Se···H interaction contributes 8.7% in complex **2**, reinforcing their involvement in stabilising intermolecular interactions.

15. Supercapacitive studies

Electrolyte variation

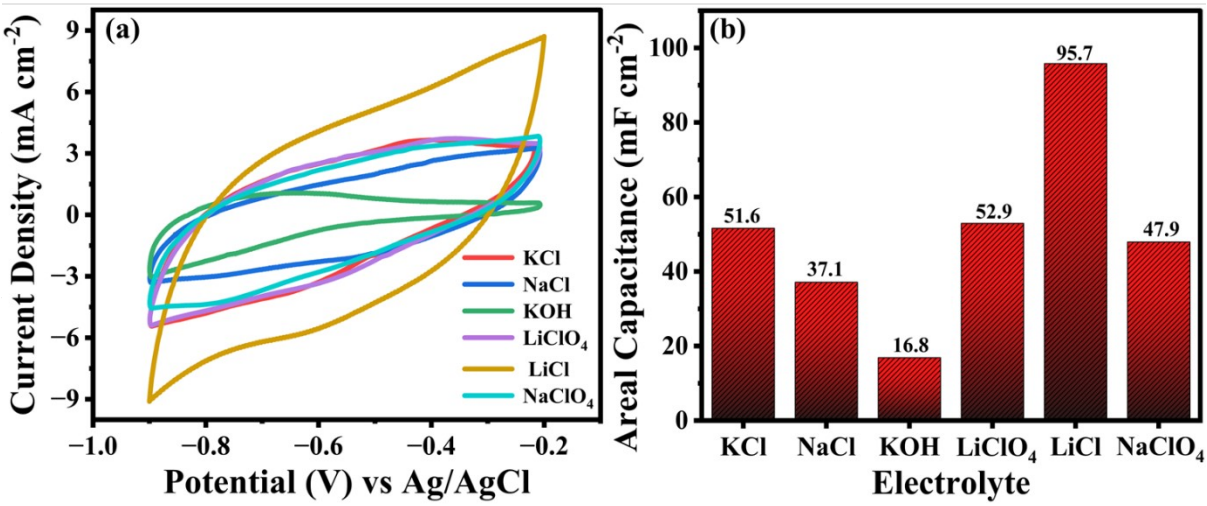

Figure S51. (a) Cyclic voltammetry responses of Complex **2** in various electrolytes at a scan rate of 100 mV s^{-1}; (b) corresponding areal capacitance for different electrolytes.

Based on this comparative analysis, 1 M LiCl was therefore chosen as the optimal electrolyte for subsequent electrochemical investigations.

16. SEM data

The SEM analysis highlights a well-preserved crystalline framework, dominated by angular and elongated crystallites. The absence of significant amorphous content or spherical particles substantiates the phase purity and successful isolation of the target complex. These morphological traits are consistent with efficient packing and potential for accessible surface area, which may be exploited in subsequent applications such as supercapacitor studies. The consistency in image contrast and sharpness further indicates the high conductivity and stability of the complex under electron beam irradiation, underscoring its robust physicochemical nature, which is suitable for advanced investigations in main-group and transition metal chemistry.[S15]

The SEM analysis of the synthesised complex shows well-defined, plate-like crystalline particles forming porous aggregates. This morphology provides a high surface area and interconnected pathways, which enhance ion diffusion and charge storage-key properties for efficient supercapacitor electrodes. Such microstructural features align with established literature, supporting the material's suitability for advanced energy storage applications and high-performance supercapacitors.[S15]

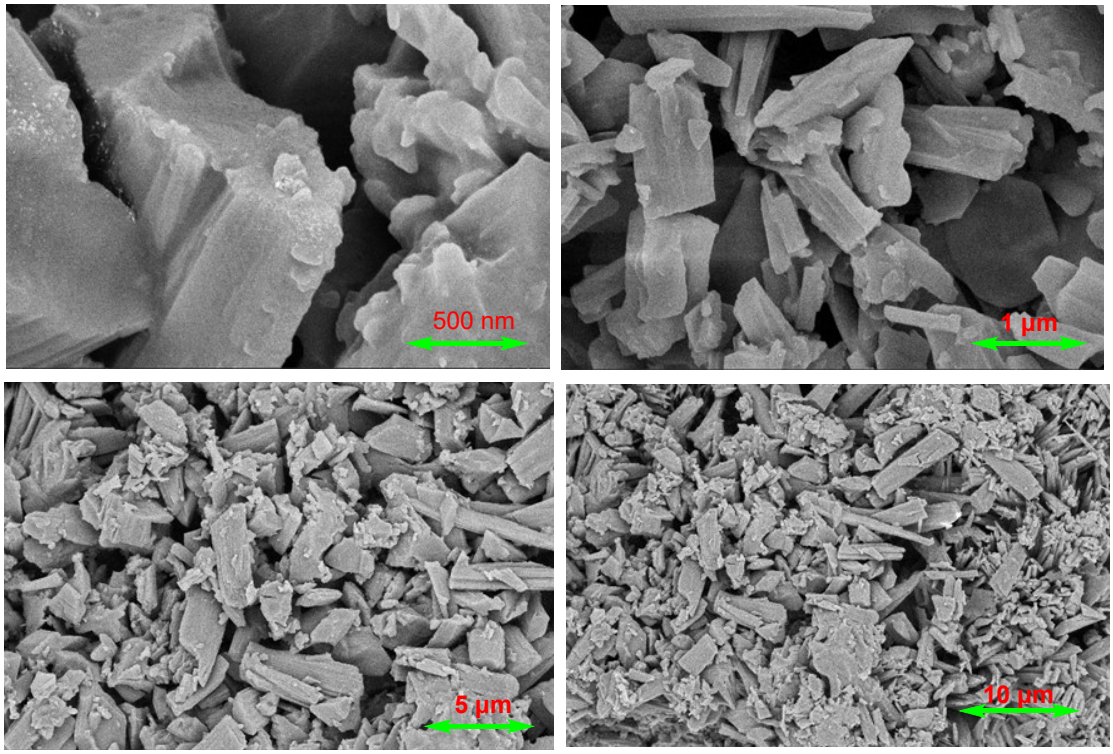

Figure S52. SEM data of complex **1**, analysed for morphological features of complexes.

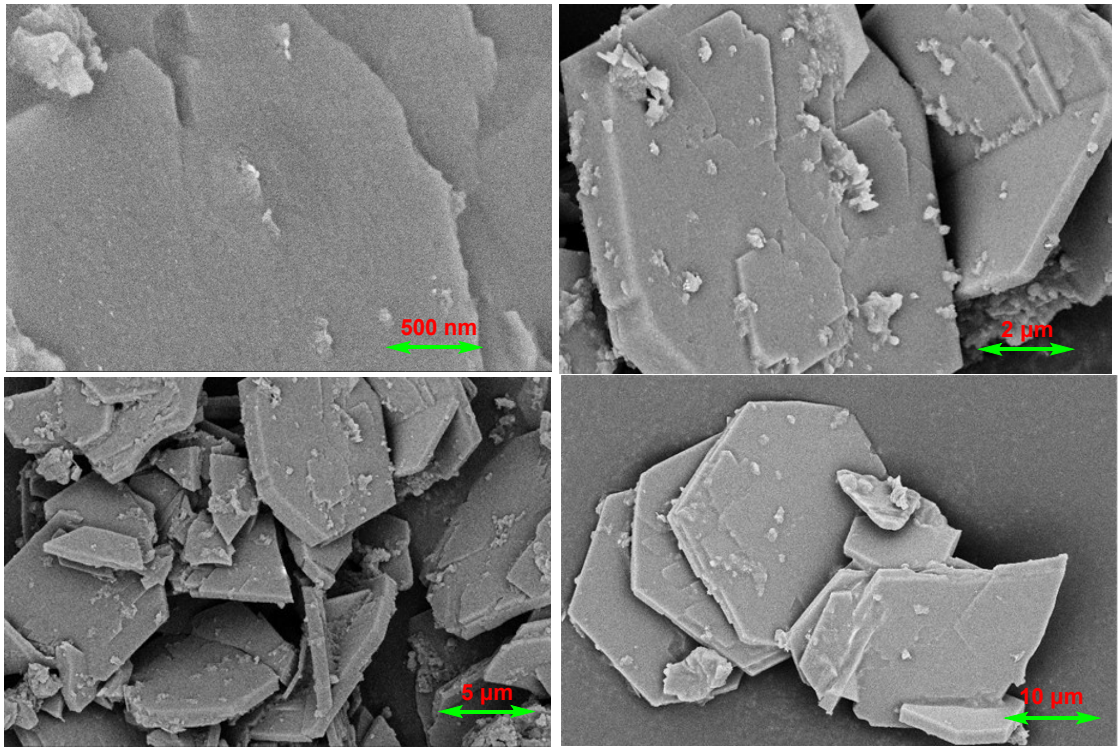

Figure S53. SEM data of complex **2**, analysed for morphological features of **2**. SEM images of the electrodes for complex **1** and complex **2**, captured both before and after the cycling stability tests.

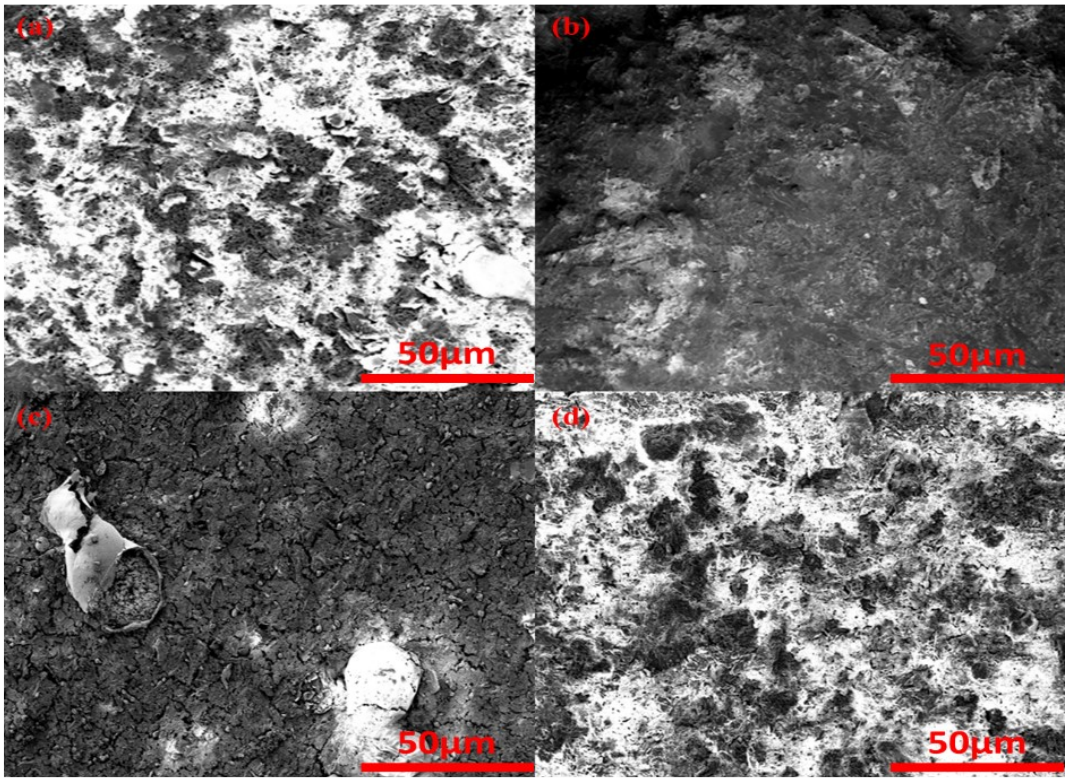

Figure S54. SEM images (50 µm) of complex **1** and complex **2** electrodes before and after cycling stability: (a) Complex **1** before, (b) complex **1** after, (c) complex **2** before, and (d) complex **2** after.

Furthermore, SEM analyses of complexes **1** and **2** were performed before and after the cycling stability test at a 50 µm scale to examine the possible morphological factors influencing performance degradation as shown in **Figure S54**. The pristine electrode of complex **1** (Figure 1 (a)) shows a porous and loosely connected surface that may initially favor electrolyte diffusion and ion transport. After 3000 cycles in 1 M LiCl electrolyte (**Figure S54** (b)), this porous framework becomes more compact and less defined, indicating structural densification and partial morphological collapse. Such changes could hinder ion access to electrochemically active sites, thereby contributing to the observed capacitance loss and a retention of 81.2 %. In contrast, complex **2** exhibits a distinct morphological evolution. The fresh electrode (**Figure S54** (c)) presents a comparatively dense microstructure, which gradually evolves into a more uniform and porous surface after prolonged cycling (**Figure S54** (d)). This structural evolution can promote more effective electrolyte infiltration and stable interfacial contact, thereby accounting for the improved structural integrity and the higher capacitance retention of 87.3 % after 3000 cycles in a 1 M LiCl electrolyte.

17. BET Isotherm Data of the complex 2:

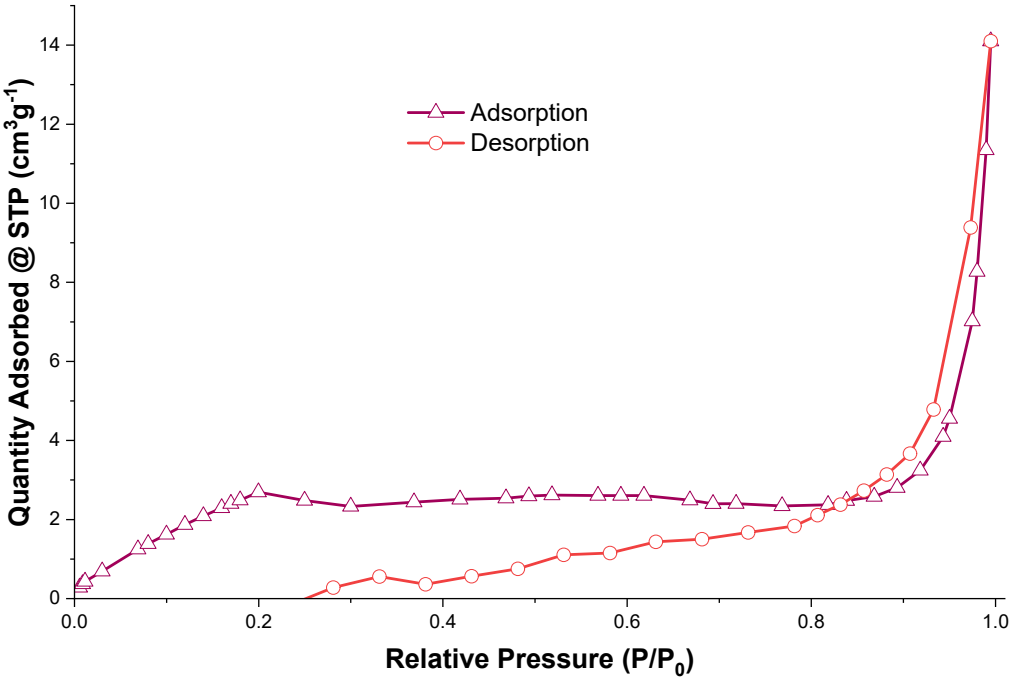

Figure S55. BET analysis of the nitrogen adsorption-desorption isotherm of complex **2**.

In electrochemical studies, the active surface area of the electrode plays a pivotal role in determining its performance. Accordingly, Brunauer-Emmett-Teller (BET) surface area analysis was conducted to evaluate this parameter, yielding a specific surface area of 14 cm^2 g^{-1} for the electrode material of complex **2**.

The N_2 adsorption-desorption isotherm of complex **2** **(Figure S55)** exhibits a type-IV profile, characteristic of a mesoporous material. Gradual nitrogen uptake at low relative pressures ($P/P_0 < 0.1$) corresponds to surface monolayer-multilayer adsorption, while the limited increase in the intermediate region ($P/P_0 \approx 0.1$-0.3) indicates minimal microporosity. A pronounced hysteresis loop at higher relative pressures ($P/P_0 \approx 0.4$-0.9) arises from capillary condensation within mesopores, and the sharp uptake near $P/P_0 = 1.0$ suggests the presence of larger mesopores or interparticle voids. Overall, the isotherm confirms that complex **2** possesses an accessible mesoporous architecture favourable for efficient mass transport and surface interactions.

18. Optimised Coordinates

Energies are in Hartree

Complex **1**, Singlet (S = 0)

E_{hf} = -5540.1013923

24	0.000404000	0.001366000	0.000017000
16	-0.177166000	-1.723258000	1.585970000
16	-0.190494000	-1.721753000	-1.586076000
16	-1.404250000	1.017082000	1.586113000
16	-1.396584000	1.027912000	-1.585863000
16	1.582798000	0.709485000	1.585961000
16	1.588039000	0.697362000	-1.586112000
6	-0.332598000	-3.134879000	0.697724000
6	-0.338560000	-3.134203000	-0.697895000
6	-2.550275000	1.855984000	0.698011000
6	-2.546830000	1.860851000	-0.697605000
6	2.883413000	1.279759000	0.697687000
6	2.885771000	1.274308000	-0.697931000

7	-0.470940000	-4.442020000	1.101908000
7	-0.480657000	-4.440920000	-1.102146000
7	-3.613995000	2.628093000	1.102310000
7	-3.608363000	2.636045000	-1.101751000
7	4.084978000	1.812679000	1.101862000
7	4.088822000	1.803794000	-1.102192000
6	-0.565687000	-5.277210000	-0.000138000
6	-4.290839000	3.126649000	0.000327000
6	4.855708000	2.148063000	-0.000193000
16	-0.742331000	-6.920253000	-0.000175000
16	-5.627058000	4.098921000	0.000423000
16	6.367238000	2.815955000	-0.000247000
6	4.489871000	1.974831000	-2.483212000
6	4.481431000	1.994344000	2.482852000
6	-0.533273000	-4.873767000	-2.483159000
6	-0.511701000	-4.876218000	2.482898000
6	-3.970012000	2.879728000	2.483345000
6	-3.957612000	2.897243000	-2.482739000
1	-4.189373000	1.938677000	2.986463000
1	-3.143531000	3.371714000	2.994889000
1	-4.846777000	3.519537000	2.489876000
1	-4.832908000	3.539062000	-2.489131000
1	-3.127674000	3.390566000	-2.987333000
1	-4.176862000	1.959963000	-2.992912000
1	4.492940000	1.032484000	2.994216000
1	5.474543000	2.432297000	2.489260000
1	3.777213000	2.655794000	2.986223000
1	3.788712000	2.634238000	-2.993502000
1	5.483954000	2.410576000	-2.489677000
1	4.500774000	1.009309000	-2.987626000

1	-0.622665000	-5.955921000	2.489287000
1	0.410752000	-4.591403000	2.987608000
1	-1.354088000	-4.410285000	2.992937000
1	-1.379729000	-4.406950000	-2.985594000
1	0.385006000	-4.588891000	-2.995391000
1	-0.644795000	-5.953413000	-2.489645000

Complex **1**; Triplet (S = 1)

E_{hf} = -5540.1053867

24	0.000027000	-0.351737000	-0.000034000
16	1.738066000	-0.410977000	-1.582285000
16	1.261101000	-1.806780000	1.317827000
16	-0.994708000	1.368681000	-1.327250000
16	0.994669000	1.368745000	1.327170000
16	-1.260987000	-1.806883000	-1.317814000
16	-1.738016000	-0.410987000	1.582245000
6	2.947635000	-1.208630000	-0.727017000
6	2.753427000	-1.777502000	0.539273000
6	-0.410714000	2.760155000	-0.568229000
6	0.410541000	2.760182000	0.568183000
6	-2.753310000	-1.777659000	-0.539255000
6	-2.947543000	-1.208746000	0.727014000
7	4.258268000	-1.435788000	-1.070234000
7	3.954400000	-2.325251000	0.920718000
7	-0.642918000	4.073457000	-0.891689000
7	0.642623000	4.073498000	0.891669000
7	-3.954257000	-2.325489000	-0.920672000
7	-4.258159000	-1.435964000	1.070248000
6	4.909034000	-2.131102000	-0.063674000
6	-0.000197000	4.915935000	0.000006000
6	-4.908890000	-2.131367000	0.063723000

16	6.486737000	-2.622657000	-0.041836000
16	-0.000273000	6.569130000	0.000022000
16	-6.486566000	-2.623009000	0.041915000
6	-4.868197000	-1.004860000	2.311293000
6	-4.177723000	-3.027380000	-2.167952000
6	4.177896000	-3.027077000	2.168029000
6	4.868285000	-1.004709000	-2.311298000
6	-1.458256000	4.510227000	-2.007298000
6	1.457929000	4.510321000	2.007280000
1	-1.072802000	4.082037000	-2.931171000
1	-2.486911000	4.180703000	-1.866229000
1	-1.416345000	5.593862000	-2.047424000
1	1.415987000	5.593956000	2.047375000
1	1.072471000	4.082149000	2.931160000
1	2.486594000	4.180819000	1.866238000
1	-3.626795000	-3.967647000	-2.174080000
1	-5.241545000	-3.223658000	-2.255117000
1	-3.835489000	-2.409835000	-2.996586000
1	-4.735859000	0.069770000	2.428616000
1	-5.923938000	-1.252552000	2.267710000
1	-4.400833000	-1.513785000	3.153545000
1	5.924046000	-1.252313000	-2.267688000
1	4.400974000	-1.513721000	-3.153526000
1	4.735862000	0.069904000	-2.428685000
1	3.835768000	-2.409456000	2.996651000
1	3.626892000	-3.967299000	2.174252000
1	5.241709000	-3.223431000	2.255134000

Complex **1**; Quintet (S = 2)

E_{hf} = -5540.1418184

24	-0.200994000	0.000616000	-0.000059000

16	-0.130762000	2.085975000	1.220865000
16	1.473615000	0.825893000	-1.517552000
16	1.472693000	-0.827314000	1.517016000
16	-0.134523000	-2.084915000	-1.220884000
16	-1.929307000	-0.769925000	1.545941000
16	-1.928609000	0.773654000	-1.545567000
6	1.222976000	2.754519000	0.453291000
6	1.885207000	2.235287000	-0.675280000
6	1.881432000	-2.237686000	0.674991000
6	1.218029000	-2.755900000	-0.453355000
6	-3.280557000	-0.311689000	0.632444000
6	-3.280274000	0.316529000	-0.632112000
7	1.882852000	3.905601000	0.801429000
7	2.917488000	3.095674000	-0.957699000
7	2.912127000	-3.099967000	0.957423000
7	1.875652000	-3.908319000	-0.801344000
7	-4.594766000	-0.488177000	0.981579000
7	-4.594318000	0.494069000	-0.981312000
6	2.940778000	4.146379000	-0.059011000
6	2.933222000	-4.150955000	0.059012000
6	-5.437312000	0.003309000	0.000127000
16	4.000367000	5.414850000	-0.019346000
16	3.990402000	-5.421438000	0.019446000
16	-7.089942000	0.003956000	0.000074000
6	-5.032349000	1.110616000	-2.218284000
6	-5.033354000	-1.104448000	2.218492000
6	3.846684000	2.923571000	-2.056423000
6	1.513132000	4.753162000	1.917604000
6	3.841847000	-2.929369000	2.055937000
6	1.504156000	-4.755412000	-1.917283000

1	4.319820000	-1.954022000	1.980375000
1	3.311006000	-2.990754000	3.005095000
1	4.582711000	-3.719609000	1.991886000
1	2.243924000	-5.545167000	-1.997437000
1	0.517377000	-5.183722000	-1.746381000
1	1.479394000	-4.162953000	-2.830307000
1	-4.649148000	-0.539184000	3.066108000
1	-6.118330000	-1.103163000	2.225635000
1	-4.656666000	-2.124535000	2.274059000
1	-4.648748000	0.544867000	-3.065854000
1	-6.117324000	1.110405000	-2.225373000
1	-4.654645000	2.130319000	-2.273989000
1	2.254352000	5.541556000	1.997749000
1	0.527096000	5.183295000	1.746992000
1	1.487486000	4.160580000	2.830524000
1	4.322848000	1.947317000	-1.981153000
1	3.315790000	2.986146000	-3.005473000
1	4.589035000	3.712411000	-1.992339000

Complex **1**; Septet (S = 3)

E_{hf} = -5540.1553244

24	0.000499000	-0.001149000	-0.001064000
16	0.650054000	1.848842000	-1.444170000
16	-1.240219000	1.516321000	1.442678000
16	-1.925538000	-0.363102000	-1.445023000
16	-0.693894000	-1.834610000	1.442009000
16	1.278486000	-1.487576000	-1.444601000
16	1.934657000	0.314553000	1.443124000
6	-0.140607000	3.079372000	-0.586412000
6	-0.915443000	2.943066000	0.585906000
6	-2.597431000	-1.661997000	-0.586763000

6	-2.092669000	-2.265144000	0.585724000
6	2.739373000	-1.418041000	-0.586643000
6	3.008241000	-0.679613000	0.586274000
7	-0.151113000	4.412075000	-0.909624000
7	-1.359011000	4.199585000	0.910049000
7	-3.747354000	-2.335885000	-0.909552000
7	-2.960586000	-3.276052000	0.910488000
7	3.899114000	-2.074543000	-0.910157000
7	4.318126000	-0.923768000	0.910709000
6	-0.900601000	5.135983000	0.000542000
6	-4.000977000	-3.346076000	0.001138000
6	4.900426000	-1.787915000	0.000572000
16	-1.186125000	6.763920000	0.001151000
16	-5.269883000	-4.405112000	0.002524000
16	6.453186000	-2.354159000	0.001112000
6	4.993323000	-0.351634000	2.059158000
6	4.048432000	-2.946860000	-2.058613000
6	-2.192658000	4.498382000	2.058070000
6	0.530738000	4.977471000	-2.057494000
6	-4.577926000	-2.026855000	-2.057086000
6	-2.803983000	-4.146854000	2.059120000
1	-4.943046000	-1.003875000	-1.981347000
1	-3.993509000	-2.126944000	-2.970313000
1	-5.409745000	-2.723461000	-2.063961000
1	-3.636724000	-4.842358000	2.066191000
1	-1.861596000	-4.687096000	1.984620000
1	-2.799844000	-3.552972000	2.971734000
1	3.839973000	-2.390508000	-2.971060000
1	5.068894000	-3.315402000	-2.066911000
1	3.348045000	-3.777086000	-1.982918000

1	4.474246000	-0.641349000	2.971375000
1	6.011037000	-0.727656000	2.069087000
1	4.993188000	0.734468000	1.982027000
1	0.345218000	6.046484000	-2.062336000
1	1.598963000	4.780048000	-1.983902000
1	0.149436000	4.523688000	-2.970884000
1	-3.129907000	3.949222000	1.984039000
1	-1.679754000	4.200847000	2.971300000
1	-2.382086000	5.566707000	2.063592000

Complex **2**; singlet (S = 0)

E_{hf} = -11550.1972326

24	-0.000102000	-0.002661000	-0.000769000
16	-1.542078000	-0.813120000	-1.572502000
16	0.069160000	1.740973000	-1.572735000
16	-1.703423000	-0.379075000	1.570173000
16	1.476356000	-0.931724000	-1.573067000
16	1.177016000	-1.289000000	1.573095000
16	0.525893000	1.659954000	1.573925000
6	-2.921677000	-1.178639000	-0.691259000
6	0.438290000	3.117119000	-0.688626000
6	-2.998327000	-0.979886000	0.688815000
6	2.484975000	-1.938267000	-0.689081000
6	2.348702000	-2.100904000	0.690009000
6	0.646039000	3.080205000	0.690667000
7	-4.132779000	-1.690993000	-1.093769000
7	0.598021000	4.425061000	-1.084076000
7	-4.263065000	-1.363065000	1.076788000
7	3.539399000	-2.728497000	-1.084453000
7	3.315432000	-2.995606000	1.086614000
7	0.939934000	4.364254000	1.087206000

6	-4.978137000	-1.813321000	-0.010494000
6	-4.462943000	-2.032963000	-2.462962000
6	0.913109000	5.215316000	0.001793000
6	0.469966000	4.884104000	-2.453365000
6	-4.769768000	-1.336375000	2.435930000
6	4.067231000	-3.395789000	0.001404000
6	3.512531000	-3.428781000	2.456094000
6	1.217186000	4.751019000	2.456696000
34	-6.680549000	-2.437815000	0.006085000
34	1.227469000	7.003246000	0.002161000
34	5.461240000	-4.558600000	0.002059000
6	4.001917000	-2.845608000	-2.453540000
1	3.235730000	-3.320105000	-3.065759000
1	4.211909000	-1.853817000	-2.850594000
1	4.902837000	-3.450918000	-2.453093000
1	4.275563000	-4.200704000	2.457441000
1	3.833453000	-2.587566000	3.069566000
1	2.576311000	-3.820637000	2.850322000
1	-4.792528000	-2.342510000	2.852489000
1	-4.113149000	-0.706981000	3.029906000
1	-5.780552000	-0.937621000	2.433031000
1	-5.455699000	-2.472187000	-2.468160000
1	-4.448107000	-1.137350000	-3.083021000
1	-3.733288000	-2.744264000	-2.846973000
1	0.539529000	5.967257000	-2.452486000
1	1.267164000	4.461304000	-3.063914000
1	-0.491709000	4.566262000	-2.852787000
1	2.026803000	4.138058000	2.849539000
1	1.501533000	5.798502000	2.458754000
1	0.329250000	4.605324000	3.070943000

Complex **2**; Triplet (S = 1)

E_{hf} = -11550.2581672

24	-0.000282000	0.128095000	0.000144000
16	-1.901406000	0.146216000	-1.493124000
16	1.096541000	1.765056000	-1.407351000
16	-1.099784000	1.763180000	1.407655000
16	0.967178000	-1.595452000	-1.432895000
16	-0.964797000	-1.597302000	1.432924000
16	1.900817000	0.149259000	1.493348000
6	-2.894345000	1.211648000	-0.629370000
6	2.561479000	1.879990000	-0.566738000
6	-2.564808000	1.875970000	0.566897000
6	0.396979000	-2.947981000	-0.583797000
6	-0.392094000	-2.948735000	0.583767000
6	2.892108000	1.216154000	0.629498000
7	-4.170902000	1.598913000	-0.953567000
7	3.652724000	2.640217000	-0.907375000
7	-3.657181000	2.634610000	0.907425000
7	0.619117000	-4.263820000	-0.905318000
7	-0.611775000	-4.265003000	0.905242000
7	4.168118000	1.605289000	0.953585000
6	-4.665510000	2.481055000	-0.018374000
6	-4.882353000	1.131474000	-2.128550000
6	4.661360000	2.488132000	0.018325000
6	3.712835000	3.482996000	-2.086922000
6	-3.718569000	3.477367000	2.086922000
6	0.004435000	-5.099759000	-0.000064000
6	-1.388193000	-4.695712000	2.053114000
6	4.880378000	1.138871000	2.128482000
34	-6.299695000	3.272851000	-0.007887000

34	6.294398000	3.282286000	0.007668000
34	0.006118000	-6.915739000	-0.000113000
6	1.396292000	-4.693024000	-2.053241000
1	0.954093000	-4.289844000	-2.962637000
1	2.416701000	-4.324597000	-1.962030000
1	1.388782000	-5.777645000	-2.078074000
1	-1.378076000	-5.780305000	2.078296000
1	-0.947169000	-4.291156000	2.962467000
1	-2.409477000	-4.329797000	1.961559000
1	-3.545007000	2.872011000	2.974933000
1	-2.951292000	4.247671000	2.027235000
1	-4.703422000	3.931060000	2.125163000
1	-5.866149000	1.589036000	-2.129980000
1	-4.333051000	1.414551000	-3.024970000
1	-4.969561000	0.046807000	-2.093876000
1	4.697515000	3.936988000	-2.126023000
1	3.538663000	2.877547000	-2.974745000
1	2.945416000	4.253114000	-2.026611000
1	4.969894000	0.054401000	2.093414000
1	5.863217000	1.598486000	2.130229000
1	4.330333000	1.420446000	3.024915000

Complex **2**; Quintet (S = 2)

E_{hf} = -11550.2552059

24	-0.067644000	0.000795000	0.000281000
16	-1.777553000	-0.911577000	-1.443667000
16	0.015228000	1.976380000	-1.428067000
16	-1.771096000	0.926045000	1.443653000
16	1.618420000	-0.976743000	-1.463603000
16	-0.000435000	-1.975375000	1.428632000
16	1.625347000	0.965393000	1.464751000

6	-3.136840000	-0.366611000	-0.593360000
6	1.214907000	2.817665000	-0.574845000
6	-3.134177000	0.390901000	0.593180000
6	1.853997000	-2.418224000	-0.601038000
6	1.192105000	-2.826408000	0.575085000
6	1.873070000	2.404497000	0.601633000
7	-4.453482000	-0.573207000	-0.922948000
7	1.733458000	4.046147000	-0.900583000
7	-4.449331000	0.607059000	0.922570000
7	2.731709000	-3.423062000	-0.922917000
7	1.700069000	-4.059461000	0.900227000
7	2.759054000	3.402125000	0.923298000
6	-5.286510000	0.019930000	-0.000231000
6	-4.885906000	-1.317497000	-2.090969000
6	2.691908000	4.430634000	0.010144000
6	1.315732000	4.816105000	-2.057601000
6	-4.876514000	1.354508000	2.090501000
6	2.655668000	-4.451438000	-0.010297000
6	1.275899000	-4.826236000	2.057024000
6	3.636301000	3.359196000	2.078633000
34	-7.102523000	0.026460000	-0.000311000
34	3.661908000	5.965707000	0.006829000
34	3.612915000	-5.994501000	-0.007365000
6	3.609528000	-3.386987000	-2.078055000
1	3.014041000	-3.301533000	-2.985399000
1	4.271051000	-2.525403000	-2.006134000
1	4.186857000	-4.305454000	-2.090847000
1	1.847903000	-5.747882000	2.077956000
1	1.455237000	-4.248297000	2.962002000
1	0.211890000	-5.043633000	1.980621000

1	-4.481501000	0.883245000	2.988920000
1	-4.499495000	2.374134000	2.029793000
1	-5.961321000	1.355200000	2.110715000
1	-5.970648000	-1.308414000	-2.112569000
1	-4.485432000	-0.850336000	-2.989103000
1	-4.518258000	-2.340485000	-2.029223000
1	1.903293000	5.727737000	-2.085130000
1	1.479811000	4.231613000	-2.961215000
1	0.256100000	5.052432000	-1.976132000
1	4.290520000	2.492009000	2.007260000
1	4.221370000	4.272756000	2.091086000
1	3.039938000	3.279227000	2.985901000

Complex **2**; Septet (S = 3)

E_{hf} = -11550.2524768

24	0.002527000	0.000141000	0.000014000
16	-1.666313000	-1.026978000	1.444868000
16	1.727430000	-0.928436000	1.445698000
16	0.011525000	-1.961065000	-1.442822000
16	-0.054949000	1.960318000	1.442963000
16	-1.699236000	0.970729000	-1.445663000
16	1.695209000	0.986229000	-1.445697000
6	-1.826950000	-2.481154000	0.586416000
6	3.066385000	-0.339896000	0.586511000
6	-1.140288000	-2.863463000	-0.584709000
6	-1.236538000	2.823292000	0.584743000
6	-1.909447000	2.418285000	-0.586741000
6	3.053226000	0.443235000	-0.586424000
7	-2.658483000	-3.524706000	0.908445000
7	4.386114000	-0.535371000	0.909402000
7	-1.589700000	-4.119725000	-0.907064000

7	-1.728406000	4.063527000	0.907292000
7	-2.775840000	3.433097000	-0.908719000
7	4.365630000	0.683043000	-0.909254000
6	-2.530588000	-4.551934000	0.000566000
6	-3.542655000	-3.524745000	2.059275000
6	5.211035000	0.087893000	0.000086000
6	4.829282000	-1.297539000	2.062146000
6	-1.124478000	-4.871075000	-2.058224000
6	-2.683099000	4.463817000	-0.000547000
6	-3.659051000	3.403617000	-2.059903000
6	4.782940000	1.459641000	-2.062013000
34	-3.414410000	-6.138212000	0.000254000
34	7.026680000	0.118487000	0.000133000
34	-3.620078000	6.019290000	-0.000100000
6	-1.289326000	4.830002000	2.058753000
1	-1.478617000	4.261883000	2.967921000
1	-0.221537000	5.026854000	1.979971000
1	-1.844295000	5.762109000	2.073816000
1	-4.222784000	4.330447000	-2.075294000
1	-3.068668000	3.304380000	-2.969172000
1	-4.333022000	2.552376000	-1.980549000
1	-1.332818000	-4.310028000	-2.967627000
1	-0.050605000	-5.031310000	-1.979162000
1	-1.647374000	-5.821554000	-2.073101000
1	-4.074523000	-4.470215000	2.074923000
1	-2.956341000	-3.405016000	2.968706000
1	-4.245168000	-2.696970000	1.979231000
1	5.913852000	-1.278212000	2.081351000
1	4.426250000	-0.851619000	2.969798000
1	4.470901000	-2.322369000	1.981642000

1	4.391299000	2.472191000	-1.981038000
1	5.867552000	1.475818000	-2.081848000
1	4.394157000	1.000997000	-2.969538000

Complex **1**; q = -1, Doublet (S = ½)

E_{hf} = -5540.2631751

24	-0.364601000	0.000192000	0.000146000
16	1.344454000	-0.536891000	1.599936000
16	-0.284247000	-2.243594000	-0.911317000
16	-2.130137000	-0.496011000	1.638946000
16	-2.129959000	0.496845000	-1.638666000
16	-0.283341000	2.243963000	0.911713000
16	1.344238000	0.536959000	-1.600078000
6	1.904950000	-1.923291000	0.767520000
6	1.255774000	-2.603158000	-0.253192000
6	-3.481388000	-0.193879000	0.676594000
6	-3.481310000	0.194743000	-0.676442000
6	1.256659000	2.603027000	0.253342000
6	1.905377000	1.923014000	-0.767611000
7	3.090472000	-2.602924000	1.005924000
7	2.072892000	-3.667873000	-0.601949000
7	-4.807390000	-0.297265000	1.052647000
7	-4.807272000	0.298258000	-1.052615000
7	2.074222000	3.667411000	0.602006000
7	3.091119000	2.602196000	-1.006134000
6	3.210043000	-3.685438000	0.169344000
6	-5.644143000	0.000412000	-0.000068000
6	3.211234000	3.684631000	-0.169514000
16	4.471287000	-4.785561000	0.097181000
16	-7.310286000	0.000347000	-0.000193000
16	4.472885000	4.784270000	-0.097471000

6	4.071276000	2.202611000	-1.989812000
6	1.764172000	4.625622000	1.637662000
6	1.762154000	-4.626208000	-1.637279000
6	4.071058000	-2.203501000	1.989237000
6	-5.242717000	-0.682414000	2.376555000
6	-5.242412000	0.682970000	-2.376709000
1	-4.875094000	-1.681183000	2.610362000
1	-4.844182000	0.015290000	3.112159000
1	-6.328005000	-0.667048000	2.388338000
1	-6.327730000	0.669372000	-2.388122000
1	-4.873143000	1.680905000	-2.611444000
1	-4.845299000	-0.015992000	-3.111905000
1	1.432271000	4.093985000	2.527852000
1	2.662948000	5.199730000	1.842281000
1	0.966636000	5.295255000	1.313144000
1	3.679987000	2.349489000	-2.996974000
1	4.957039000	2.813876000	-1.845389000
1	4.306016000	1.147317000	-1.858439000
1	4.956586000	-2.815073000	1.844637000
1	4.306083000	-1.148298000	1.857642000
1	3.680039000	-2.350106000	2.996543000
1	0.964453000	-5.295446000	-1.312361000
1	1.430202000	-4.094661000	-2.527508000
1	2.660654000	-5.200691000	-1.842044000

Complex **2**; q = -1, Doublet (S = ½)

E_{hf} = -11550.3651817

24	0.444510000	0.000002000	0.000233000
16	2.204710000	-0.512014000	1.635358000
16	0.363824000	2.230977000	0.941682000
16	2.204493000	0.512292000	-1.635115000

16	-1.263705000	-0.559027000	1.595964000
16	0.364115000	-2.230838000	-0.941515000
16	-1.264100000	0.558539000	-1.595257000
6	3.555833000	-0.199039000	0.674567000
6	-1.169895000	2.606578000	0.279091000
6	3.555745000	0.199317000	-0.674513000
6	-1.817604000	-1.941521000	0.753222000
6	-1.169599000	-2.606620000	-0.278938000
6	-1.818026000	1.941176000	-0.752820000
7	4.883103000	-0.303664000	1.048663000
7	-1.984713000	3.670950000	0.634171000
7	4.882966000	0.303929000	-1.048782000
7	-2.997156000	-2.631775000	0.988564000
7	-1.984568000	-3.670792000	-0.634342000
7	-2.997559000	2.631434000	-0.988281000
6	5.712780000	0.000088000	-0.000127000
6	5.311303000	-0.699514000	2.373409000
6	-3.110902000	3.700485000	-0.142546000
6	-1.665463000	4.616906000	1.680661000
6	5.310984000	0.699737000	-2.373598000
6	-3.110682000	-3.700507000	0.142437000
6	-1.665545000	-4.616578000	-1.681056000
6	-3.970532000	2.243513000	-1.986209000
34	7.542796000	0.000044000	-0.000262000
34	-4.486460000	4.918828000	-0.060104000
34	-4.486229000	-4.918838000	0.059654000
6	-3.970057000	-2.244093000	1.986648000
1	-3.561422000	-2.390643000	2.986513000
1	-4.214115000	-1.190507000	1.860248000
1	-4.852792000	-2.861958000	1.853115000

1	-2.566898000	-5.172808000	-1.920142000
1	-1.302183000	-4.071064000	-2.549838000
1	-0.888044000	-5.304871000	-1.347979000
1	4.895033000	0.014317000	-3.110669000
1	4.951737000	1.705111000	-2.590681000
1	6.395751000	0.672691000	-2.398256000
1	6.396051000	-0.671755000	2.398136000
1	4.894821000	-0.014550000	3.110598000
1	4.952742000	-1.705190000	2.590247000
1	-2.565702000	5.176287000	1.916563000
1	-1.306274000	4.071419000	2.551217000
1	-0.884741000	5.302125000	1.348818000
1	-4.213549000	1.189632000	-1.860324000
1	-4.853766000	2.860511000	-1.851967000
1	-3.562492000	2.391048000	-2.986179000

19. References:

[S1] (a) Y. Wang, H. P. Hickox, Y. Xie, P. Wei, S. A. Blair, M. K. Johnson, III, H. F. Schaefer and G. H. Robinson, *J. Am. Chem. Soc.,* 2017, **139**, 6859. (b) S. Das, A. Jain, S. Ahamed, B. Sahu, S. Suthar, B. Schwarz, C. L. Mascarenhas, S. Mondal, S. Banerjee, S. K. Kushvaha, H. W. Roesky and K. C. Mondal, *Angew. Chem. Int. Ed*., 2025, e202507231. doi.org/10.1002/anie.202507231.

[S2] (a) A. M. Salvi, J. E. Castle, J. F. Watts and E. Desimoni, *Appl. Surf. Sci.*, 1995, **90**, 333-341. (b) E. Korin, N. Froumin, and S. Cohen, *ACS Biomater. Sci. Eng.,* 2017, **3**, 882-889.

[S3] (a) S. Stoll and A. Schweiger, *J. Magn. Reson.,* 2006, **178**, 42–55. (b) S. Ye, *Magn. Reson. Lett.*, 2023, **3**, 43-60.

[S4] A. D. Becke, *J. Chem. Phys.,* 1993, **98**, 1372-1377.

[S5] P. J. Stephens, F. J.; Devlin, C. F. Chabalowski, M. J. Frisch M. J. *J. Phys. Chem.,* 1994, **98**, 11623-11627.

[S6] C. Lee, W. Yang and R. G. Parr, *Phys. Rev. B,* 1988, **37**, 785-789.

[S7] S. Grimme, J. Antony, S. Ehrlich and H. Krieg, *J. Chem. Phys.,* 2010, **132**, 154104-154124.

[S8] S. Grimme, S. Ehrlich and L. Goerigk, *J. Comput. Chem.,* 2011, **32**, 1456-1465.

[S9] S. Weigend, R. Ahlrichs, *Phys. Chem. Chem. Phys.,* 2005, **7**, 3297-3305.

[S10] Gaussian 16, Revision A.03, Frisch, M. J.; Trucks, G. W.; Schlegel, H. B.; Scuseria, G. E.; Robb, M. A.; Cheeseman, J. R.; Scalmani, G.; Barone, V.; Petersson, G. A.; Nakatsuji, H.; Li, X.; Caricato, M.; Marenich, A. V.; Bloino, J.; Janesko, B. G.; Gomperts, R.; Mennucci, B.; Hratchian, H. P.; Ortiz, J. V.; Izmaylov, A. F.; Sonnenberg, J. L.; Williams-Young, D.; Ding, F.; Lipparini, F.; Egidi, F.; Goings, J.; Peng, B.; Petrone, A.; Henderson, T.; Ranasinghe, D.; Zakrzewski, V. G.; Gao, J.; Rega, N.; Zheng, G.; Liang, W.; Hada, M.; Ehara, M.; Toyota, K.; Fukuda, R.; Hasegawa, J.; Ishida, M.; Nakajima, T.; Honda, Y.; Kitao, O.; Nakai, H.; Vreven, T.; Throssell, K.; Montgomery, J. A., Jr.; Peralta, J. E.; Ogliaro, F.; Bearpark, M. J.; Heyd, J. J.; Brothers, E. N.; Kudin, K. N.; Staroverov, V. N.; Keith, T. A.; Kobayashi, R.; Normand, J.; Raghavachari, K.; Rendell, A. P.; Burant, J. C.; Iyengar, S. S.; Tomasi, J.; Cossi, M.; Millam, J. M.; Klene, M.; Adamo, C.; Cammi, R.; Ochterski, J. W.; Martin, R. L.; Morokuma, K.; Farkas, O.; Foresman, J. B.; Fox, D. J. Gaussian, Inc., Wallingford CT, 2016.

[S11] E. D. Glendening, C. R. Landis and F. Weinhold, *J. Comput. Chem.,* 2013, **34**, 1429-1437.

[S12] A. E. Reed, L. A. Curtiss and F. Weinhold, *Chem. Rev.,* 1988, **88**, 899-926.

[S13] M. P. Mitoraj, A. Michalak and T. Ziegler, *J. Chem. Theory Comput*., 2009, **5**, 962-975.

[S14] G. Deng, S. Lei, S. Pan, J. Jin, G. Wang, L. Zhao, M. Zhou and G. Frenking, *Chem. Eur. J*., 2020, **26**, 10487-10500.

[S15] M. Islam, M. S. Hossain, B. Adak, M. M. Rahman, K. Moni, A. S. Nur, H. Hong, H. Younes, and S. Mukhopadhyay, *J. Energy Storage*, 2025, **107**, 114838.